

A NUMERICAL INVESTIGATION OF THE FORMATION OF SECONDARY VORTICES
IN LABORATORY-SIMULATED TORNADOES

by

Robert Lambert Walko

A Dissertation Submitted to the Faculty of the

DEPARTMENT OF ATMOSPHERIC SCIENCES

In Partial Fulfillment of the Requirements
For the Degree of

DOCTOR OF PHILOSOPHY
WITH A MAJOR IN ATMOSPHERIC SCIENCES

In the Graduate College

THE UNIVERSITY OF ARIZONA

1 9 8 3

INFORMATION TO USERS

This reproduction was made from a copy of a document sent to us for microfilming. While the most advanced technology has been used to photograph and reproduce this document, the quality of the reproduction is heavily dependent upon the quality of the material submitted.

The following explanation of techniques is provided to help clarify markings or notations which may appear on this reproduction.

1. The sign or "target" for pages apparently lacking from the document photographed is "Missing Page(s)". If it was possible to obtain the missing page(s) or section, they are spliced into the film along with adjacent pages. This may have necessitated cutting through an image and duplicating adjacent pages to assure complete continuity.
2. When an image on the film is obliterated with a round black mark, it is an indication of either blurred copy because of movement during exposure, duplicate copy, or copyrighted materials that should not have been filmed. For blurred pages, a good image of the page can be found in the adjacent frame. If copyrighted materials were deleted, a target note will appear listing the pages in the adjacent frame.
3. When a map, drawing or chart, etc., is part of the material being photographed, a definite method of "sectioning" the material has been followed. It is customary to begin filming at the upper left hand corner of a large sheet and to continue from left to right in equal sections with small overlaps. If necessary, sectioning is continued again—beginning below the first row and continuing on until complete.
4. For illustrations that cannot be satisfactorily reproduced by xerographic means, photographic prints can be purchased at additional cost and inserted into your xerographic copy. These prints are available upon request from the Dissertations Customer Services Department.
5. Some pages in any document may have indistinct print. In all cases the best available copy has been filmed.

**University
Microfilms
International**

300 N. Zeeb Road
Ann Arbor, MI 48106

8324466

Walko, Robert Lambert

A NUMERICAL INVESTIGATION OF THE FORMATION OF SECONDARY
VORTICES IN LABORATORY-SIMULATED TORNADOES

The University of Arizona

PH.D. 1983

University
Microfilms
International 300 N. Zeeb Road, Ann Arbor, MI 48106

A NUMERICAL INVESTIGATION OF THE FORMATION OF SECONDARY VORTICES
IN LABORATORY-SIMULATED TORNADOES

by

Robert Lambert Walko

A Dissertation Submitted to the Faculty of the

DEPARTMENT OF ATMOSPHERIC SCIENCES

In Partial Fulfillment of the Requirements
For the Degree of

DOCTOR OF PHILOSOPHY
WITH A MAJOR IN ATMOSPHERIC SCIENCES

In the Graduate College

THE UNIVERSITY OF ARIZONA

1 9 8 3

THE UNIVERSITY OF ARIZONA
GRADUATE COLLEGE

As members of the Final Examination Committee, we certify that we have read
the dissertation prepared by Robert Lambert Walko

entitled A Numerical Investigation of the Formation of
Secondary Vortices in Laboratory-Simulated Tornadoes

and recommend that it be accepted as fulfilling the dissertation requirement
for the Degree of Doctor of Philosophy.

Robert J. Bell

Date

7/6/83

D. O. Staley

Date

7/6/83

S. D. Womery

Date

7/6/83

Thomas F. Bels

Date

7/6/83

Edward J. Kuhn

Date

7/6/83

Final approval and acceptance of this dissertation is contingent upon the
candidate's submission of the final copy of the dissertation to the Graduate
College.

I hereby certify that I have read this dissertation prepared under my
direction and recommend that it be accepted as fulfilling the dissertation
requirement.

Robert J. Bell
Dissertation Director

Date

8/2/83

STATEMENT BY AUTHOR

This dissertation has been submitted in partial fulfillment of requirements for an advanced degree at The University of Arizona and is deposited in the University Library to be made available to borrowers under rules of the Library.

Brief quotations from this dissertation are allowable without special permission, provided that accurate acknowledgment of source is made. Requests for permission for extended quotation from or reproduction of this manuscript in whole or in part may be granted by the head of the major department or the Dean of the Graduate College when in his judgment the proposed use of the material is in the interests of scholarship. In all other instances, however, permission must be obtained from the author.

SIGNED: Robert L. Walke

ACKNOWLEDGEMENTS

I wish to gratefully acknowledge the support of my committee chairman, Dr. Robert Gall, who suggested this research project to me and provided the contract funds. His continual suggestions and comments concerning not only this work but also the philosophy of research in general were extremely valuable.

My sincere appreciation goes to my wife Carla who typed most of the penultimate draft of this dissertation and who, along with my daughter Anika, provided a wonderfully supportive home environment. I also wish to express my gratitude to my parents for the encouragement they have given me throughout my life.

I wish to thank the faculty, staff and students of the Department of Atmospheric Sciences for their friendship and help during my graduate studies. I was fortunate to have been supported by a Research Associateship during this time.

This research was supported by NSF contract ATM-815554. The numerical computations were performed on the CRAY-1 computer at the National Center for Atmospheric Research and a portion of the project was carried out while the author was a visitor at that institution. I am particularly grateful to Mr. Ken Hansen of the NCAR Scientific Computing Division for his continued help with the system software.

TABLE OF CONTENTS

	Page
LIST OF ILLUSTRATIONS	vi
LIST OF TABLES.	x
NOMENCLATURE.	xi
ABSTRACT.	xiv
1. INTRODUCTION.	1
1.1 General Statement of the Problem	1
1.2 Focus of the Investigation	3
1.3 Survey of Vortex Instability Studies	12
1.4 Summary of this Investigation.	18
2. DESCRIPTION OF THE AXISYMMETRIC MODEL	20
2.1 Coordinate System and Model Variables.	20
2.2 System of Hydrodynamic Equations	22
2.3 Finite Difference Grid and Equations	26
2.4 Method of Solution	30
2.5 Spatial and Temporal Boundary Conditions	35
A. Inner Boundary	37
B. Lower Boundary	38
C. Outer Boundary	38
D. Upper Boundary	39
E. Initial Temporal Boundary.	41
2.6 General Development of the Solution.	41
2.7 Model Testing and Verification	41
3. DESCRIPTION OF THE LINEAR MODEL	44
3.1 Linearization of the Hydrodynamic Equations.	44
3.2 Fourier Decomposition of the Perturbation Variables.	48
3.3 Finite Difference Grid and Equations	51
3.4 Method of Solution	55
3.5 Spatial Boundary Conditions.	57
A. Inner Boundary	57
B. Lower Boundary	58
C. Outer Boundary	58
D. Upper Boundary	58

TABLE OF CONTENTS--continued

	Page
3.6 Initialization and Development of Solution	59
3.7 Derivation of Energy Equations	61
3.8 Linear Model Testing and Verification.	64
4. EXPERIMENTS AND RESULTS	67
4.1 Specifications of Numerical Experiments.	67
A. Linear Dimensions.	67
B. Eddy Viscosity Coefficient	68
C. Density.	69
D. Swirl Ratio.	69
E. Linear Wavenumber.	70
F. List of Axisymmetric and Linear Experiments.	70
4.2 Axisymmetric Model Solutions	72
4.3 Growth Rates of Linear Perturbations	85
4.4 Linear Perturbation Structures	91
4.5 Energy Budgets of Linear Perturbations	118
4.6 Phase Speeds of Linear Perturbations	122
5. DISCUSSION AND CONCLUSIONS.	125
5.1 Discussion of Linear Results	125
5.2 Conclusions.	138
REFERENCES.	144

LIST OF ILLUSTRATIONS

Figure		Page
1.1	Cross section of the Purdue vortex simulator. The diagram is shown approximately to scale and all dimensions are given in meters. (After Church et al., 1979)	7
2.1	Coordinate system and variables used in numerical models	21
2.2	The finite difference grid on which the difference equations are based. The diagram indicates the relative placement of the dependent variables and the scheme for numbering indices	27
4.1	Radial height cross sections of numerically-generated stream function fields. The swirl ratio is denoted by S while the contour interval is indicated by Δ . Negative-valued contours are represented by a broken pattern while the zero and positive contours are solid lines	73
4.2	Same as in Figure 4.1 but for higher swirl cases . . .	74
4.3	Same as in Figure 4.1 but for radial velocity.	76
4.4	Same as in Figure 4.1 but for radial velocity and higher swirl cases	77
4.5	Same as in Figure 4.1 but for azimuthal velocity . . .	78
4.6	Same as in Figure 4.1 but for azimuthal velocity and higher swirl cases	79
4.7	Same as in Figure 4.1 but for vertical velocity. . . .	81
4.8	Same as in Figure 4.1 but for vertical velocity and higher swirl cases	82
4.9	Same as in Figure 4.1 but for vertical vorticity . . .	83
4.10	Same as in Figure 4.1 but for vertical vorticity and higher swirl cases	84

LIST OF ILLUSTRATIONS--continued

Figure		Page
4.11	Same as in Figure 4.1 but for azimuthal vorticity. . .	86
4.12	Same as in Figure 4.1 but for azimuthal vorticity and higher swirl cases	87
4.13	Radial-height cross sections of various numerically generated fields for the case $S=1.0$ and $\nu=0.000186$. Contour scheme is as in Figure 4.1	88
4.14	Growth rates of linear perturbations in s^{-1} as a function of swirl ratio and wavenumber. The contours represent cases with $\nu=0.001$ and the numbers to the right of the plot are growth rates for the case $\nu=0.000186$ and $S=1.0$	90
4.15	Horizontal cross sections through the linear per- turbation fields of u' and v' for $S=0.3$ and $m=1$. In any column, the plots represent three different, equally spaced levels for the same field, and all have the same contour interval as given by Δ . The circle added to each plot denotes the location of the maximum value of ζ for that level. See text for a more complete description.	93
4.16	Same as in Figure 4.15 but for the fields w' and p' with $m=1$ and $S=0.3$	94
4.17	Same as in Figure 4.15 but for the fields ζ' with $m=1$ and $S=0.3$, and ζ' with $m=1$ and $S=0.5$	95
4.18	Same as in Figure 4.15 but for the fields u' and v' with $m=1$ and $S=0.5$	96
4.19	Same as in Figure 4.15 but for the fields w' and p' with $m=1$ and $S=0.5$	97
4.20	Same as in Figure 4.15 but for the fields u' and v' with $m=2$ and $S=0.5$	98
4.21	Same as in Figure 4.15 but for the fields w' and p' with $m=2$ and $S=0.5$	99
4.22	Same as in Figure 4.15 but for the fields ζ' with $m=2$ and $S=0.5$, and ζ' with $m=2$ and $S=1.0$	100

LIST OF ILLUSTRATIONS--continued

Figure		Page
4.23	Same as in Figure 4.15 but for the fields u' and v' with $m=2$ and $S=1.0$	101
4.24	Same as in Figure 4.15 but for the fields w' and p' with $m=2$ and $S=1.0$	102
4.25	Same as in Figure 4.15 but for the fields u' and v' with $m=2$ and $S=3.0$	103
4.26	Same as in Figure 4.15 but for the fields w' and p' with $m=2$ and $S=3.0$	104
4.27	Same as in Figure 4.15 but for the fields ζ' with $m=4$ and $S=2.0$, and ζ' with $m=2$ and $S=3.0$	105
4.28	Same as in Figure 4.15 but for the fields u' and v' with $m=4$ and $S=2.0$	106
4.29	Same as in Figure 4.15 but for the fields w' and p' with $m=4$ and $S=2.0$	107
4.30	Same as in Figure 4.15 but for the fields u' and v' with $m=5$ and $S=1.0$	108
4.31	Same as in Figure 4.15 but for the fields w' and p' with $m=5$ and $S=1.0$	109
4.32	Same as in Figure 4.15 but for the fields ζ' with $m=5$ and $S=1.0$, and ζ' with $m=5$ and $S=3.0$	110
4.33	Same as in Figure 4.15 but for the fields u' and v' with $m=5$ and $S=3.0$	111
4.34	Same as in Figure 4.15 but for the fields w' and p' with $m=5$ and $S=3.0$	112

LIST OF ILLUSTRATIONS--continued

Figure		Page
4.35	<p>Histograms showing the contributions of eight individual sources (or sinks) of energy for the perturbations as a function of swirl ratio and wavenumber. The small square within each histogram serves to locate the proper positions on the coordinate axes. The height of an individual bar denotes the rate of energy input divided by twice the total energy in the perturbation, and thus is equivalent to a growth rate. The small increments along the vertical axis denote growth rate units of 0.1 s^{-1}</p>	121

LIST OF TABLES

Table		Page
4.1	List of numerical experiments	71
4.2	A comparison of the maximum amplitudes (over all levels and radii) of different perturbation fields within the same experiment as a function of swirl ratio and wavenumber.	117
4.3	Angular velocity ω in degrees per second of linear perturbations as a function of swirl ratio and wavenumber.	123

NOMENCLATURE

r	radial coordinate in cylindrical system
θ	azimuthal coordinate in cylindrical system
z	vertical coordinate in cylindrical system
t	time coordinate
u	radial velocity component
v	azimuthal velocity component
w	vertical velocity component
p	pressure
ζ	vertical vorticity component
η	azimuthal vorticity component
ψ	stream function
$\bar{u}, \bar{v}, \bar{w}, \bar{p},$ $\bar{\zeta}, \bar{\eta}, \bar{\psi}$	axisymmetric velocity components, pressure, vorticity components and stream function
$u', v', w',$ p', ζ', η'	perturbation velocity components, pressure, and vorticity components
U, V, W, P	complex amplitude of perturbation velocity components and pressure
ρ	density
ν	eddy viscosity coefficient
\vec{V}	velocity vector
\vec{F}	frictional force vector
F_r, F_θ, F_z	components of frictional force

NOMENCLATURE--continued

F_r' , F_θ' , F_z'	components of perturbation friction force
m	perturbation wavenumber
E'	perturbation kinetic energy
G	perturbation growth rate
ω	angular velocity (rate of change of θ) of perturbation phase lines
S	swirl ratio (of axisymmetric flow)
Γ	$(2\pi)^{-1}$ times the circulation of the axisymmetric flow at the rim of the updraft hole of the simulator
Q	$(2\pi)^{-1}$ times the volume flow rate through the simulator
r_0	radius of updraft hole in simulator
h	height of inflow region of simulator
u_0	radial velocity beneath rim of updraft hole
v_0	azimuthal velocity beneath rim of updraft hole
i	imaginary unit $\sqrt{-1}$; radial position index of finite difference variables
k	vertical position index of finite difference variables
I	maximum value of radial index i
K	maximum value of vertical index k
n	time index of finite difference variables
Δr , Δz , Δt	unit increments of independent variables used in finite difference equations
r_i , s_i	discrete radial position

NOMENCLATURE--continued

- $\tilde{u}, \tilde{w}, \tilde{U}, \tilde{V}, \tilde{W}$ temporary velocity components computed from tendency equations excluding pressure terms
- δ strength of time filter
- Δ contour interval used in plots

ABSTRACT

Two numerical models, described in detail herein, have been constructed and used to investigate the formation of secondary vortices in axisymmetrically-forced rotating flows. The particular type of vortex flow examined is that developed in a laboratory vortex simulator where secondary vortices have been produced and extensively studied. The first numerical model generated a collection of steady state, axisymmetric vortex flows based on a range of swirl ratios. The second model tested those flows for instability by simulating the behavior of small amplitude, axially asymmetric, linear perturbations superimposed on the flows: amplification of the perturbations indicated instability whereas damping indicated stability. For those flows found to be unstable, the linear perturbations of various azimuthal wavenumbers were analyzed in detail, and from the perturbation growth rates, structures, phase speeds, and energetics, the nature of the instability could be studied.

The results of the instability study show that the vortex is stable for the lowest swirl ratios but that above a certain value, instability persists indefinitely. The most rapidly growing wavenumber shifts steadily with increasing swirl from 1 to around 5 in the swirl range investigated. Growth rates were found to be high enough for secondary vortices to form in the laboratory simulator in just a few seconds. Structurally, the perturbation fields were found to have

a helical tilt and to be centered near the radius of maximum vertical vorticity in the axisymmetric vortex. They propagated in the same azimuthal direction as the rotation of the axisymmetric flow, but at a somewhat lower angular velocity at the surface. These linear results are all consistent with observed laboratory behavior. From this, it was concluded that linear theory is capable of explaining many important aspects of secondary vortices.

An analysis of the perturbation energy equation revealed that at the higher swirl ratios, the perturbation received most of its energy from the deformation of the axisymmetric flow due to the radial distribution of azimuthal velocity, while for low swirl the primary source was from the radial distribution of the vertical velocity. No other component of the axisymmetric vortex ever contributed more than about 25% of these terms.

Chapter 1

INTRODUCTION

1.1 General Statement of the Problem

Numerous observations of the intense swirling flow in tornadoes have revealed that a tornado vortex may take on a variety of configurations. Of particular interest to this study is the fact that some tornadoes possess a high degree of symmetry about their axis of rotation while others display large azimuthal variations in all three velocity components. The most readily observable feature of asymmetric tornadoes is the presence of a number of individual small but intense whirlwinds embedded within the tornadic circulation. These whirlwinds are located away from the center of the circulation and travel in an approximately circular path around that center while simultaneously spinning on their own axes. Examples of this type of behavior may be found in Fujita et al. (1970), Agee et al. (1975), and Forbes (1976). It may be seen from the photographs in these articles that the whirlwinds sometimes occur within the walls of a large tornado cloud (e.g., Agee et al., 1975, p. 326) rendering them nearly or totally invisible, and sometimes appear as distinct clouds themselves (as in Fujita et al., 1970, p. 45). Various names have been given to the small whirlwinds. These include subvortex, satellite vortex, suction vortex, secondary vortex, subsidiary vortex, and

multiple vortex, each term emphasizing a particular property of the whirlwind (Fujita et al., 1976). Rather than attempt to enlarge the list, this paper will adopt the term "secondary vortex" for reasons to be explained later.

The wind speeds in secondary vortices have been observed in nature and in numerical simulations to be significantly higher than the azimuthal mean winds associated with the larger tornado vortex (Fujita et al., 1976; Rotunno, 1982). Along with the stronger winds comes increased damage and disruption to objects on the ground. Since a secondary vortex revolves around the tornado center while the tornado travels in a comparatively straight path, the secondary vortex describes an approximate cycloidal trajectory with respect to the ground. Cycloidal damage patterns which result from this behavior are readily apparent, particularly in agricultural areas where the ground is uniform, but also in urban areas (Fujita, et al., 1976). Tornado damage to man made structures can result from a number of mechanisms which include direct aerodynamic forces from the wind, rapid changes in wind velocity (gusts), and rapid changes in pressure (Mehta, 1976). Because secondary vortices contain high wind speeds and the winds rotate with a small radius of curvature (implying very high spatial gradients of wind velocity and pressure) while at the same time they travel rapidly across the ground, they can inflict damage by all these mechanisms. Consequently, the proper consideration for the design of tornado-resistant structures must allow for the effects of secondary vortices. Understanding the conditions which

lead to secondary vortex formation, the mechanisms by which they form, and their basic structure and intensity in tornadoes are thus goals of practical as well as scientific importance. The general purpose of this work is to explore the reasons why secondary vortices occur and to gain some insight into their structure and behavior. The specific goals to be achieved and the method by which the study is to be conducted will be addressed once the problem has been explained in greater detail.

1.2 Focus of the Investigation

Due to the violent and transient nature of tornadoes, it is difficult to ascertain their velocity and pressure fields by direct measurement. Most conventional local-sensing instruments (e.g., anemometers and wind vanes) are not designed to withstand the strong winds encountered, and even if they were, it is virtually impossible to know exactly when and where to set up the instruments in advance. There are various remote sensing techniques which circumvent these problems but none so far has been able to give comprehensive results. Doppler radar is often used to measure the gross rotational and convergent wind patterns of tornadoes and the larger scale flow surrounding them, but is not able to resolve the small-scale structure within the tornado. Photogrammetry has achieved reasonable success in distinguishing sub-tornado scale features and has provided quantitative wind data both inside and outside secondary vortices. However, the measurements are limited to areas made visible by dust and debris, and

not obscured by other dust in the foreground; consequently, only a partial description of the flow is attained by this means. Furthermore, the swirling dust being photographed is diffuse making its location difficult to pinpoint, and thus the method is prone to a fair degree of uncertainty. Because of inadequacies in these and other measurement techniques, direct study of tornadoes has not yet been able to provide sufficient quantitative data for explaining the presence and characteristics of secondary vortices.

A valuable asset to the study of tornado dynamics and a useful alternative to direct tornado observation has been the laboratory vortex simulator. These devices have been capable of reproducing a wide variety of vortex configurations closely resembling their atmospheric counterparts. The basic function of the simulators is to generate vorticity in the working fluid and then to concentrate that vorticity by means of radial convergence and axial stretching of vortex tubes (Davies-Jones, 1976). The various simulators differ in the way this is accomplished. Davies-Jones pointed out that for a simulated vortex to have relevance to real tornadoes, the two flows must be geometrically and dynamically similar. Although some processes associated with tornadoes, such as deep moist convection and vortex translation, cannot be reproduced in the laboratory because of practical limitations, it is possible to artificially generate a flow similar to that which occurs in the vicinity of a tornado vortex. According to Davies-Jones, vortex simulators of the type first built by Ward (1972) are the most successful at accomplishing this. A Ward-type machine is designed to

model the tornadic flow that is associated with a large rotating cumulonimbus supercell. This flow is characterized by a large updraft having a diameter on the order of 10 km, a shallow surface inflow layer only 1 or 2 km deep which feeds the updraft, and a high level of angular momentum in the inward flowing air. Geometric similarity to this flow is obtained in Ward's machine by simply scaling down the flow dimensions equally. Dynamic similarity requires the two flows to have the same ratio of angular momentum of the inflow to volume flow rate through the system (Davies-Jones, 1973). Ward's machine is capable of varying this ratio throughout the range encountered in tornadic flows. Dynamic similarity also requires the Reynolds number of the simulated vortex to be the same as that in a tornado. This is not possible due to the large difference in scale; however, it has been demonstrated that since the Reynolds numbers in both cases are very large, the flow is insensitive to changes in Reynolds number and thus the two may still be considered to be alike. A Ward-type simulator therefore satisfies the necessary criteria for relevance to at least some tornadic flows. Because secondary vortices are readily producible in the simulator, and since the laboratory flow lends itself to much more careful scrutiny than do atmospheric tornadoes, we will focus our attention on the simulated secondary vortices.

A detailed description of the Purdue vortex simulator, a Ward-type machine from which extensive flow measurements have been taken and published, may be found in Church et al. (1979). Here, a discussion of the essential details of the simulator geometry and operation

will be given. The simulator is cylindrically symmetric and consists of two connecting chambers, one atop the other. The approximate size and shape of the apparatus are shown by a vertical cross section in Fig. 1.1. A fan located above the simulator drives the air out through a chimney leading from the top of the upper chamber. Air is drawn into the lower chamber through the open outer boundary. A wire screen which covers this opening is caused to rotate about the center axis of the chamber. This action imparts angular momentum to the air as it enters. The rotating air flows radially inward through the lower chamber until reaching the updraft hole which separates the two chambers. There, it turns upward and proceeds to flow through the upper chamber. At the top of the chamber, the air passes through a baffle which allows free vertical flow but suppresses any radial and azimuthal motion. The primary importance of the baffle is to prevent any turbulent motion generated by the fan from travelling upstream and affecting the dynamics within the chambers. By removing the rotation from the exiting fluid, the baffle also serves to distribute the pressure deficit caused by the action of the fan uniformly across the top of the chamber. The flow in the simulator is rendered visible by injecting smoke at key locations. It is evident that the lower and upper chambers are designed to channel the flow so as to resemble the inflow and updraft regions, respectively, of the flow in which a tornado is embedded. In the simulator, as in the atmosphere, the tornado vortex occurs well inside the outer boundary of the updraft and thus does not interact directly with the artificial chamber walls.

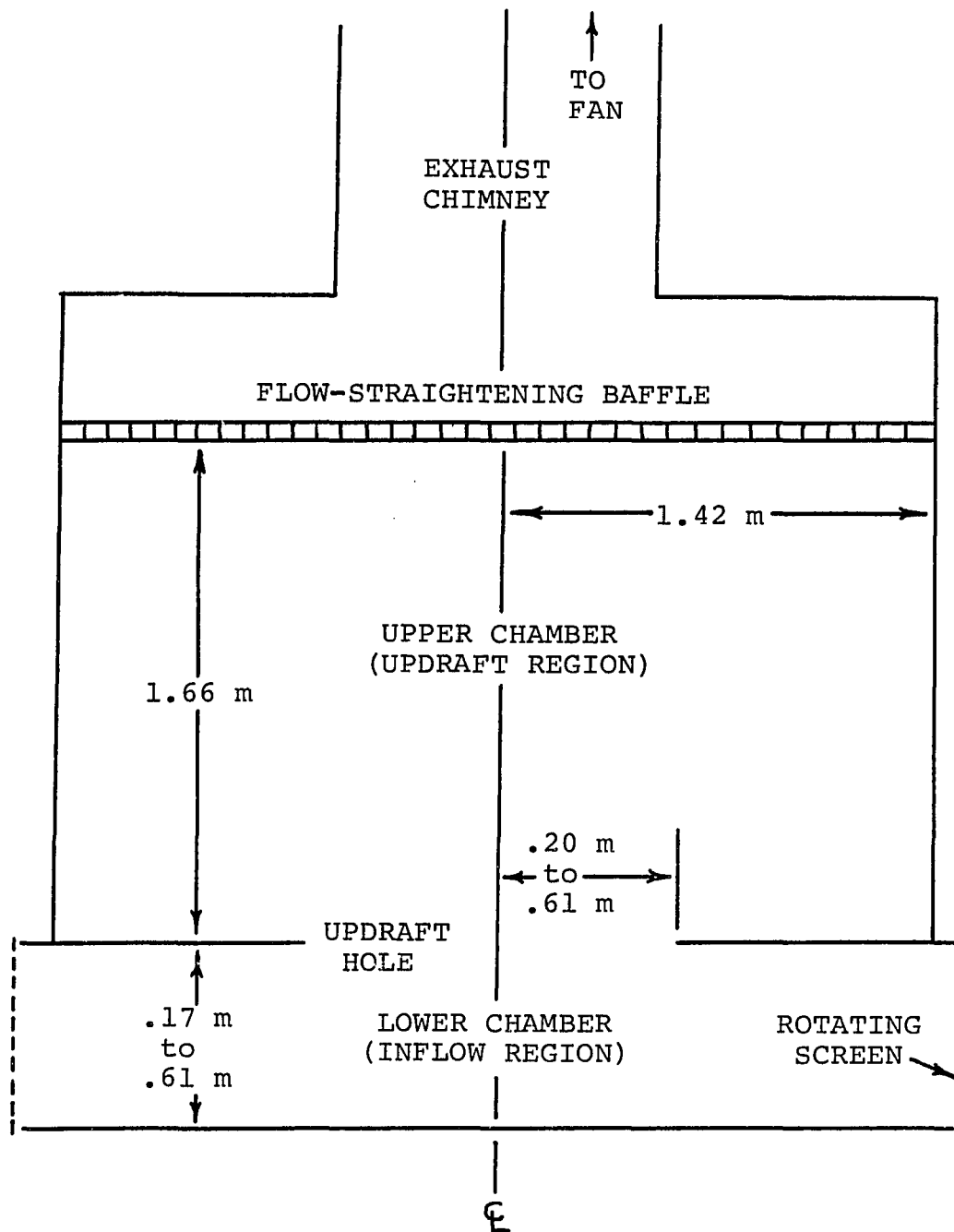


Figure 1.1. Cross section of the Purdue vortex simulator. The diagram is shown approximately to scale and all dimensions are given in meters. (After Church et al., 1979)

Four parameters governing the flow are adjustable in this simulator: (1) the radius of the updraft hole, (2) the height of the inflow region, (3) the speed of the fan (which controls the volume flow rate), and (4) the rotational speed of the screen (which controls the angular momentum of the inflow air). As these parameters are varied through their mechanically permissible ranges, the simulator generates its entire variety of flow regimes. It has been demonstrated both by experiment and by theoretical argument that there exists a nondimensional parameter, related algebraically to all four of the adjustable experimental parameters, which can alone determine the type of flow configuration which occurs. This parameter, known as the swirl ratio, is given by $S = r_0 \Gamma / 2Qh$, where r_0 is the radius of the updraft hole, h is the height of the inflow region, Q is $1/2\pi h$ times the total volumetric flow rate through the simulator, and Γ is $1/2\pi$ times the circulation of the air beneath the rim of the updraft hole. If S is held constant while the other quantities are varied, the quantitative nature of the flow may change substantially but the qualitative nature only a small amount. Therefore, by simply varying S through its range, all vortex configurations are obtained.

Experiments performed with the Purdue simulator have shown the following progression of vortex configurations to occur as the swirl ratio is increased from zero to high values (Church et al., 1979).

$S=0.0$ This is the case where the azimuthal velocity is zero. The flow changes from radial to vertical as it proceeds from the lower to the upper chamber.

- S=0.1 The radial and vertical velocity distributions are nearly identical to those for the no swirl case. Swirling velocity intensifies toward the center axis until a narrow, rapidly spinning core is reached. The core is laminar and nearly cylindrical throughout the height of the simulator except for the very top, at the baffle, where it widens abruptly and becomes turbulent.
- S=0.3 The breakdown point (the location at which the core becomes turbulent) has moved downward. Beneath this point the maximum upward velocity occurs along the axis but above the point the maximum updraft lies in an annular region and a sharp reduction occurs along the axis.
- S=0.5 The breakdown point has penetrated to the lower surface, and the entire core is turbulent and of greatly increased diameter. The reduced central updraft extends throughout the height of the simulator. The visual, rapidly spinning core is no longer vertical but spirals upward in a slowly diverging helical pattern. The helix itself revolves very little about the center of the chamber but propagates upward.
- S=0.7 The core is further expanded in diameter and the reduced central updraft has changed to a downdraft. The single helix has been replaced by a double helix which, unlike the single one, does revolve around the chamber center. The lower portion of

the helices are nearly vertical but tilt appreciably toward the horizontal higher up.

$S=1.2$ The two-secondary-vortex system has been replaced by three vortices. The tilt and angular velocity of the helices is similar to the double vortex case.

$S>1.2$ Further increases in the swirl ratio lead to a greater number of secondary vortices with six being the highest number achievable in this simulator. The radial and vertical flow outside the core region are qualitatively similar to the no-swirl case except that this flow is bounded by the core wall which continuously expands with S . When $S>2$, the core diameter has become large enough that the outer boundary of the chamber is beginning to influence the flow.

The particular values of S at which these states occur are not universal; a moderately weak dependence on the volumetric flow rate through the simulator (for a given value of S) has been observed (Church et al., 1979). Furthermore, comparisons made between two different Ward-type machines indicate that although the same sequence of states is produced, the corresponding swirl ratios are different. This may be due to a difference in the amount of turbulence present in the air entering the two simulators or the fact that the heights of the upper chambers from the updraft hole to the baffle are different (Gall, 1982). The main point to notice is that increasing the swirl ratio from low to high values causes the flow to undergo these remarkable

transitions. The simulated tornado begins as an axisymmetric vortex and later becomes asymmetric, developing a progressively increasing multiplicity of secondary vortices.

It is an important fact that the laboratory simulator is itself axially symmetric. The radial, rotational, and vertical components of the flow entering the machine are carefully controlled to be independent of azimuthal position as are the floor, walls, and ceiling of the chambers. As a consequence, the forcing of the flow by its environment is symmetric. This implies that the secondary vortices, an inherently asymmetric feature of the flow, are generated by the flow itself. That is, the flow undergoes a spontaneous transition from a symmetric to an asymmetric state as it is channeled through the simulator. It is for this reason that the term "secondary vortices" has been adopted to denote the whirlwinds; this choice emphasizes their arising directly from the symmetric parent or primary vortex.

The spontaneous development of secondary vortices manifests a basic physical property of the flow: namely, that of instability. More precisely, the simulator experiments indicate that axisymmetric flow of a high swirl ratio is unstable to small amplitude asymmetric perturbations. The condition of instability implies that any such perturbations introduced into the flow must grow with time, drawing their energy from the primary axisymmetric vortex. The predominance of axisymmetric flow at low swirl ratios, on the other hand, indicates that either axisymmetric flow is stable for those conditions, or that

asymmetric perturbations are limited by some mechanism from attaining very large amplitudes.

Given that secondary vortices arise as a consequence of instability, this work will employ the standard technique of a linear stability analysis to answer some basic questions concerning the onset and development of the vortices. The technique involves simulating the development of perturbations having specified azimuthal periodicities or wavenumbers by embedding them in an axisymmetric flow appropriate to the simulator. We shall be particularly concerned with the growth rates and structure of the linear perturbations as well as their general behavior and resemblance to the fully developed nonlinear vortices observed in the simulator. In addition, a detailed analysis will be made of the different energy sources of the growing perturbations. This will be used to determine the relative importance of the individual components of the primary vortex in contributing to the development of secondary vortices.

1.3 Survey of Vortex Instability Studies

The occurrence of instability in symmetrically-forced rotating flows is a widely known phenomenon and many different types of instability are possible. In the last two decades, stability criteria have been established for a wide variety of rotating flow configurations. Although most of this effort has been motivated by specific problems, such as those occurring in engineering fluid mechanics, the flows studied theoretically have usually been idealized in some way in order

to simplify the analysis or to maintain a certain degree of generality. As an example, the unperturbed flow is often assumed to be an infinitely long vortex having no variation in the axial direction. Such an approximation may be roughly valid for a fairly large portion of a tornado though it obviously cannot hold for the entire vortex. Among the studies which employ this assumption and which are not apparently motivated by concern with tornadoes are two notable examples that are, nevertheless, relevant to the tornado problem. The first, by Michalke and Timme (1967), deals with a vortex having three regions: an inner region (nearest the central axis) of uniform vorticity, a middle region of uniform but higher vorticity, and an outer region of zero vorticity. This structure is similar to that observed by Ward (1972) in simulated tornadoes that contain secondary vortices. Michalke and Timme found certain examples of this flow to be unstable to asymmetric perturbations but only to those containing three or more secondary vortices; the one- and two-vortex disturbances are always stable. A possible reason for this is that the effects of axial flow are not included in their investigation whereas in Ward's experiments, where one- and two-vortex systems are producible, axial motion is a major flow component. From this, it would appear that axial motion may play an essential role in determining the instability of a tornado vortex. The second study, by Maslowe (1974), carried out a similar stability analysis, this time for a vortex containing both azimuthal and axial flow. The distribution of azimuthal wind is simpler than that used by Michalke and Timme, consisting of a single region of uniform vorticity,

while the radial profile of axial wind is parabolic (the flow is, in effect, Poiseuille flow in solid-body rotation). Such a configuration is a reasonable approximation for the inner or core region of a tornado having moderate to high swirl (e.g., compare with Hoecker, 1960; or Rotunno, 1977) but does not, of course, bear any resemblance to the outer region where the flow is nearly irrotational. This flow was found to be unstable to perturbations of all wavenumbers except for the limiting cases of zero rotation or zero axial flow. The most unstable waves in this flow are of a spiral form similar to the secondary vortices observed in the simulator. This result tends to confirm the possible importance of axial motion on vortex instability.

Interest in applying a stability analysis to the tornado problem was stimulated by the observations of secondary vortices in natural and simulated tornadoes. Ward (1972) proposed that the secondary vortices arise from instability of an annular or cylindrical region of high vorticity which he found in his laboratory experiments. This annulus corresponds to the "middle region" of the vortex studied by Michalke and Timme. As a first step in investigating the tornado problem, Snow (1978) reexamined that vortex and analyzed the instability in much greater detail. He confirmed the results presented by Michalke and Timme and found some general similarities between the most unstable disturbances and the secondary vortices occurring in the simulator. His study does, however, share the same limitations as theirs with regard to the tornado in that axial flow is not considered. Rotunno (1978) combined a special case of the three-region vortex, one

in which the middle region is of infinitesimal thickness and the inner region is stagnant, with a two-celled distribution of axial flow. The axial flow was constant within each cell and the velocity discontinuity between the cells coincided with that in the azimuthal wind field. This vortex structure resulted in all wavenumbers, including 1 and 2, being unstable with the general helical disturbances growing more rapidly than vertically invariant ones. A comparison of this result with the corresponding one by Snow again demonstrates the influence of axial flow in destabilizing the lowest wavenumbers. One shortcoming of this particular vortex is that the waves having the highest growth rates are those with the highest wavenumbers. Rotunno attributed this result to the unrealistic infinitesimal thickness of the vortex sheet and argued that, no matter what wavenumbers are the most unstable, the diffusion will effectively dampen the shorter waves. However, this study does not allow any definitive conclusions to be drawn as to which wavenumber should actually dominate the flow for a given swirl ratio.

All the theoretical studies mentioned thus far have dealt with highly idealized flows that bear only a limited resemblance to natural or laboratory tornadoes. A more realistic vortex was tested for instability by Staley and Gall (1979). They examined horizontal cross sections at three different levels through the tornado wind profile obtained by Hoecker (1960). Radial and vertical motion were omitted from the cross sections under the assumption that the azimuthal wind is the primary source of instability, and the disturbances were assumed to be vertically constant. Interestingly, wavenumber 2 was

found to be highly unstable for all three levels although wavenumber 1 was neutral. Moreover, waves 2-4 had the highest growth rates with all wavenumbers greater than 7 being stable. Since the only essential difference between this study and that of Snow lies in the distribution of azimuthal velocity in the primary vortex, it must be concluded that that difference is solely responsible for producing the widely different results. An inspection of the Hoecker profiles used in Staley and Gall reveals that they fairly closely resemble a combined-Rankine vortex, one of the (neutrally stable) special cases considered by Snow. This fact demonstrates that, distinct from utilizing a gross simplification such as the neglecting of axial flow, there is another way in which idealized profiles may be limited: Even when an idealized profile closely resembles a real vortex, the slight departures therefrom may lead to significantly different results. Of course, the preliminary study of Staley and Gall must, itself, be suspected of oversimplifying the problem since it neglects axial flow.

Recently, Gall (1983) has carried out a more complete stability analysis for a vortex containing both axial and azimuthal flow. The vortex was generated by a numerical model (described in Gall, 1982) designed to approximate the flow in the laboratory simulator. In order to provide a simple explanation of the major vortex features, the following assumptions were employed in the model: (1) azimuthal velocity is constant with height; (2) radial velocity varies linearly with height in the lower simulator chamber and is zero in the upper chamber; and (3) vertical velocity varies quadratically in the lower chamber

and is constant in the upper chamber. With these assumptions, the numerical computations were in effect one-dimensional, being required only for determining the radial distribution of the variables in the vortex. It was the upper, axially constant portion of this modeled vortex, expanded to infinite length, that was tested for instability. Growth rates were obtained for a large number of combinations of azimuthal wavenumber, vertical wavelength, and swirl ratio. The most unstable disturbances were found to have vertical as well as azimuthal periodicities (i.e., a helical structure). A shift in the most unstable azimuthal wavenumber from low to high values, and an increase in the most unstable vertical wavelength were observed with increases in the swirl ratio. These results are qualitatively consistent with the behavior of secondary vortices in the laboratory simulator. A particularly interesting finding in this study was that, at low swirl ratios where only the low wavenumbers are unstable, the radial shear of the axial flow is the dominant source of energy for the disturbances while at higher swirl ratios, the radial shear of the azimuthal wind dominates. This is a possible explanation for why the vortex profiles (with no axial motion) studied by Snow and others failed to ever be unstable to wavenumber 1 and sometimes 2.

The study by Gall (1983) is probably more accurate than previous studies in representing the flow instability in the simulator and, presumably, in tornadoes since the unstable vortex, in spite of its simplifying assumptions, was an approximate flow solution for the simulator. This claim is supported by a general agreement with

observations. However, with that type of study, as with the others, no assessment can be made of the importance of radial flow, axial variations in the flow, or axial boundaries in determining the overall instability or unstable wave characteristics. The advantages of studying idealized vortices and finding instabilities of a general or fundamental nature are well recognized; nevertheless, only by considering all components of a vortex can a complete stability analysis be made of it.

1.4 Summary of this Investigation

A complete stability analysis of the laboratory simulator flow being the objective of this study, the restrictive assumptions used by Gall will be relaxed and an experimental procedure similar to his will be followed. An axisymmetric numerical model of the laboratory simulator will be used to produce a family of vortices based on a range of swirl ratios. This model will include all the important features of the simulator including the lower boundary, the baffle at the top, and the radial inflow of the lower chamber versus the impermeable outer wall of the upper chamber. Numerical computations will determine the two-dimensional, radial-height distribution of the flow variables which satisfies the appropriate boundary conditions. Each of these vortex flows will then be tested for instability to a range of azimuthal wavenumbers using a linear model which also conforms to the geometry of the simulator. The resulting growth rate spectra, structures, and energy budgets of the linear waves will be carefully analyzed to provide a detailed description of the vortex instability.

Chapter 2 of this work presents a detailed description of the axisymmetric model used for this study. A discussion is included of the model boundary conditions employed and their relevance to the simulator. An additional section mentions the testing procedures used to verify the model. In Chapter 3, these same areas are covered for the linear model. That chapter also contains a derivation of the energy equations used to analyze the energy budget of the unstable waves. The numerical results obtained from both models are presented in Chapter 4. An analysis and discussion of these results, followed by a final conclusion, comprise Chapter 5.

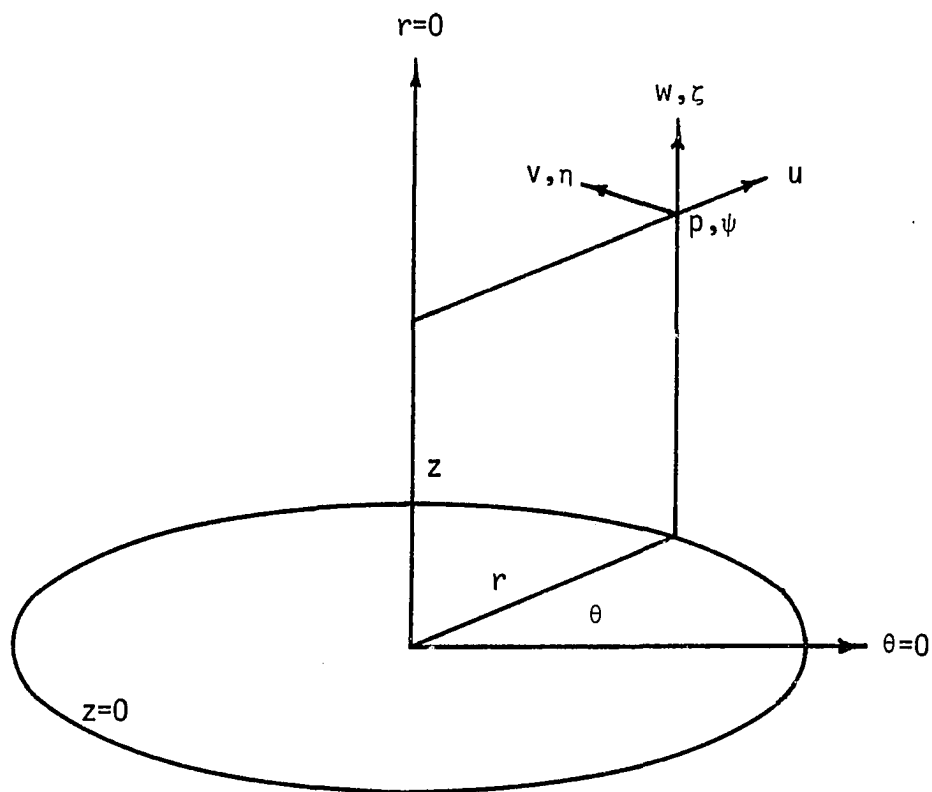
Chapter 2

DESCRIPTION OF THE AXISYMMETRIC MODEL

Of the many numerical methods available for the solution of the hydrodynamic equations, the one chosen here was deemed the most appropriate for the present problem. The reasons for selecting the various aspects of this method over possible alternatives will be explained as the discussion progresses.

2.1 Coordinate System and Model Variables

The cylindrical symmetry of the vortex simulator and of the vortex flow itself makes the use of a cylindrical coordinate system by far the most appropriate. This allows easy handling of the boundary conditions and contains the set of dependent variables which most readily describes vortex motion. Indeed, the axisymmetric vortex is just a modified form of a two-dimensional flow and can therefore be simulated on a two-dimensional grid in a cylindrical system. The coordinate system and the variables used in the model are shown in Fig. 2.1. The quantities listed as "dependent variables" are those which are actually used in the model calculations whereas the "auxiliary variables" are calculated from the dependent variables and are used only to provide a more complete description and visualization of the results. The notation is identical to that used by Rotunno (1977).



Independent Variables

r - radial position
 θ - azimuth angle
 z - height
 t - time

Dependent Variables

u - radial velocity
 v - azimuthal velocity
 w - vertical velocity
 p - pressure

Auxiliary Variables

η - azimuthal vorticity
 ζ - vertical vorticity
 ψ - stream function
 (in r - z plane)

Figure 2.1. Coordinate system and variables used in numerical models.

2.2 System of Hydrodynamic Equations

The complete system of hydrodynamic equations applicable to general fluid motions may be considerably simplified for this problem. A scale analysis of the flow in the simulator, assuming a characteristic length L of 1 m, a characteristic velocity V of 1 ms^{-1} , and an angular velocity Ω of the earth-based coordinate system of 10^{-4} s^{-1} indicates that the Rossby number $V/L\Omega$, which is a measure of the relative importance of inertial force to Coriolis force, has a numerical value of about 10^4 . Thus, the Coriolis force may be neglected. Furthermore, the Mach number V/C , where C is the speed of sound, is less than 10^{-2} indicating that dynamic compressibility effects are negligible as well. In addition, diabatic heating is absent from the flow, save for an insignificant contribution from viscous dissipation. Hence, the three equations of motion and the equation of continuity in the following form provide an accurate description of the flow.

$$\frac{\partial u}{\partial t} = -u \frac{\partial u}{\partial r} - \frac{v}{r} \frac{\partial u}{\partial \theta} - w \frac{\partial u}{\partial z} - \frac{1}{\rho} \frac{\partial p}{\partial r} + \frac{v^2}{r} + F_r \quad (2.1)$$

$$\frac{\partial v}{\partial t} = -u \frac{\partial v}{\partial r} - \frac{v}{r} \frac{\partial v}{\partial \theta} - w \frac{\partial v}{\partial z} - \frac{1}{r\rho} \frac{\partial p}{\partial \theta} - \frac{uv}{r} + F_\theta \quad (2.2)$$

$$\frac{\partial w}{\partial t} = -u \frac{\partial w}{\partial r} - \frac{v}{r} \frac{\partial w}{\partial \theta} - w \frac{\partial w}{\partial z} - \frac{1}{\rho} \frac{\partial p}{\partial z} + F_z \quad (2.3)$$

$$\frac{1}{\rho} \frac{\partial \rho}{\partial t} = -\frac{1}{r} \frac{\partial}{\partial r} (ur) - \frac{1}{r} \frac{\partial v}{\partial \theta} - \frac{\partial w}{\partial z} = 0 \quad (2.4)$$

Since gravity is not included in the vertical equation of motion, the pressure p is the nonhydrostatic part of the total pressure. The major advantage of these simplifications, apart from the reduction in

the amount of computation, is that sound and gravity waves are eliminated from the solution thereby permitting much longer timesteps in the numerical integration.

The terms F_r , F_θ , and F_z denote the components of frictional force and are defined as follows. This model adopts the usual form of fluid friction which is given by the vector equation $\vec{F} = \nu \nabla^2 \vec{V}$ and assumes that the eddy viscosity coefficient ν is constant throughout the fluid. Constant ν is a poor assumption for this problem since both laminar and turbulent regions often coexist in the flow. However, it is felt that a spatially varying viscosity coefficient unnecessarily complicates the problem and would not alter the flow significantly or change the final interpretations. The major benefit of including viscous dissipation in the model is the suppression of a spatial computational mode in the numerical integration. Furthermore, this form of frictional force can be written in a way which has the desirable property of conserving momentum in its finite difference form. From the vector identity $\nabla^2 \vec{V} = \nabla(\nabla \cdot \vec{V}) - \nabla \times (\nabla \times \vec{V})$ and the fact that $\nabla \cdot \vec{V} = 0$ for incompressible flow, it follows that $\vec{F} = -\nu \nabla \times (\nabla \times \vec{V})$. Written in component form, this becomes

$$F_r = \nu \left[\frac{\partial^2 u}{\partial z^2} - \frac{\partial^2 w}{\partial z \partial r} + \frac{1}{r^2} \frac{\partial^2 u}{\partial \theta^2} - \frac{1}{r^2} \frac{\partial}{\partial r} \left(r \frac{\partial v}{\partial \theta} \right) \right]$$

$$F_\theta = \nu \left[-\frac{1}{r} \frac{\partial^2 w}{\partial z \partial \theta} + \frac{\partial^2 v}{\partial z^2} + \frac{\partial}{\partial r} \left(\frac{1}{r} \frac{\partial}{\partial r} (rv) \right) - \frac{\partial}{\partial r} \left(\frac{1}{r} \frac{\partial u}{\partial \theta} \right) \right]$$

$$F_z = \nu \left[-\frac{1}{r} \frac{\partial}{\partial r} \left(r \frac{\partial u}{\partial z} \right) + \frac{1}{r} \frac{\partial}{\partial r} \left(r \frac{\partial w}{\partial r} \right) + \frac{1}{r^2} \frac{\partial^2 w}{\partial \theta^2} - \frac{1}{r} \frac{\partial^2 v}{\partial \theta \partial z} \right]$$

An alternative form of the equations of motion which is more suitable for numerical integration is the so-called flux form. This is obtained by adding to Eqs. 2.1 - 2.3 the continuity equation which has been multiplied by u , v or w , respectively. This gives the following set of equations when the friction terms are added.

$$\begin{aligned} \frac{\partial u}{\partial t} = & -\frac{1}{r} \frac{\partial}{\partial r} (uur) - \frac{1}{r} \frac{\partial}{\partial \theta} (uv) - \frac{\partial}{\partial z} (uw) - \frac{1}{\rho} \frac{\partial p}{\partial r} + \frac{v^2}{r} \\ & + v \left[\frac{\partial^2 u}{\partial z^2} - \frac{\partial^2 w}{\partial z \partial r} + \frac{1}{r^2} \frac{\partial^2 u}{\partial \theta^2} - \frac{1}{r^2} \frac{\partial}{\partial r} \left(r \frac{\partial v}{\partial \theta} \right) \right] \end{aligned} \quad (2.5)$$

$$\begin{aligned} \frac{\partial v}{\partial t} = & -\frac{1}{r} \frac{\partial}{\partial r} (uvr) - \frac{1}{r} \frac{\partial}{\partial \theta} (vv) - \frac{\partial}{\partial z} (vw) - \frac{1}{r\rho} \frac{\partial p}{\partial \theta} - \frac{uv}{r} \\ & + v \left[-\frac{1}{r} \frac{\partial^2 w}{\partial z \partial \theta} + \frac{\partial^2 v}{\partial z^2} + \frac{\partial}{\partial r} \left(\frac{1}{r} \frac{\partial}{\partial r} (rv) \right) - \frac{\partial}{\partial r} \left(\frac{1}{r} \frac{\partial u}{\partial \theta} \right) \right] \end{aligned} \quad (2.6)$$

$$\begin{aligned} \frac{\partial w}{\partial t} = & -\frac{1}{r} \frac{\partial}{\partial r} (uwr) - \frac{1}{r} \frac{\partial}{\partial \theta} (vw) - \frac{\partial}{\partial z} (ww) - \frac{1}{\rho} \frac{\partial p}{\partial z} \\ & + v \left[-\frac{1}{r} \frac{\partial}{\partial r} \left(r \frac{\partial u}{\partial z} \right) + \frac{1}{r} \frac{\partial}{\partial r} \left(r \frac{\partial w}{\partial r} \right) + \frac{1}{r^2} \frac{\partial^2 w}{\partial \theta^2} - \frac{1}{r} \frac{\partial^2 v}{\partial \theta \partial z} \right] \end{aligned} \quad (2.7)$$

The important advantage of the flux form is that mass and energy are exactly conserved in the finite difference version of the advective terms while they are not for the advective terms in Eqs. 2.1 - 2.3 (Haltiner and Williams, 1980, p. 178). The numerical conservation of energy, apart from being a faithful representation of the continuous equations, also prevents the possibility of nonlinear computational instability occurring in the numerical solution (Bryan, 1966). It should be pointed out that the equations could also have been written

in the "vorticity-stream function" form and solved using the mass and energy conserving finite difference operators developed by Arakawa (1966). Both methods have been used successfully to simulate flow in a cylindrical chamber, e.g., Warn-Varnas et al. (1978) and Rotunno (1977), and neither appears to have any great advantage over the other. It was a matter of the author's preference that the present method was chosen for this study.

Eqs. 2.4 - 2.7 comprise the complete set of four equations and four unknown variables which is solved numerically in both the axisymmetric and linear models. Each of the two models, however, contains one additional assumption which further simplifies the set. The purpose of the axisymmetric model is to find solutions which are axially symmetric, i.e., solutions in which θ -derivatives are zero. Hence, the set of equations used in that model reduces to

$$\frac{\partial u}{\partial t} = -\frac{1}{r} \frac{\partial}{\partial r} (uur) - \frac{\partial}{\partial z} (uw) - \frac{1}{\rho} \frac{\partial p}{\partial r} + \frac{v^2}{r} + v \left[\frac{\partial^2 u}{\partial z^2} - \frac{\partial^2 w}{\partial z \partial r} \right] \quad (2.8)$$

$$\frac{\partial v}{\partial t} = -\frac{1}{r} \frac{\partial}{\partial r} (uvr) - \frac{\partial}{\partial z} (vw) - \frac{uv}{r} + v \left[\frac{\partial^2 v}{\partial z^2} + \frac{\partial}{\partial r} \left(\frac{1}{r} \frac{\partial}{\partial r} (rv) \right) \right] \quad (2.9)$$

$$\begin{aligned} \frac{\partial w}{\partial t} = & -\frac{1}{r} \frac{\partial}{\partial r} (uwr) - \frac{\partial}{\partial z} (ww) - \frac{1}{\rho} \frac{\partial p}{\partial z} \\ & + v \left[-\frac{1}{r} \frac{\partial}{\partial r} \left(r \frac{\partial u}{\partial z} \right) + \frac{1}{r} \frac{\partial}{\partial r} \left(r \frac{\partial w}{\partial r} \right) \right] \end{aligned} \quad (2.10)$$

$$-\frac{1}{r} \frac{\partial}{\partial r} (ur) - \frac{\partial w}{\partial z} = 0 \quad (2.11)$$

2.3 Finite Difference Grid and Equations

The finite difference equations used to approximate Eqs. 2.8 - 2.11 are based on the grid lattice shown in Fig. 2.2. This grid is staggered in its placement of variables and is one of many possible designs. Arakawa and Lamb (1977) have discussed a variety of grid designs and found this one to produce the most accurate solutions for models using the primitive equations in two dimensions. On the grid, the dependent variables u , v , w , and p are no longer continuous in space but are defined at discrete points and labeled with radial index i and vertical index k . The radial and vertical grid spacings are Δr and Δz , respectively, and are uniform throughout the domain. Also defined are discrete radial distances r_i and s_i given by $r_i = \Delta r(i - \frac{3}{2})$ and $s_i = \Delta r(i - 1)$. The spatial indices vary over the ranges $1 \leq i \leq I$ and $1 \leq k \leq K$ with the extreme values representing boundary points which are located outside the computational domain and are added for computational convenience. All of the experiments performed in this study use $I = 32$ and $K = 62$. The relative positions of all variables having a given pair of indices, and the manner in which the indices are numbered are evident from Fig. 2.2. In addition to their discrete spatial representation, the dependent variables also change from being continuous in time to occupying discrete moments with a basic time increment Δt between successive steps.

The difference equations for general variables having spatial indices i , k and time index n are written in the following way.

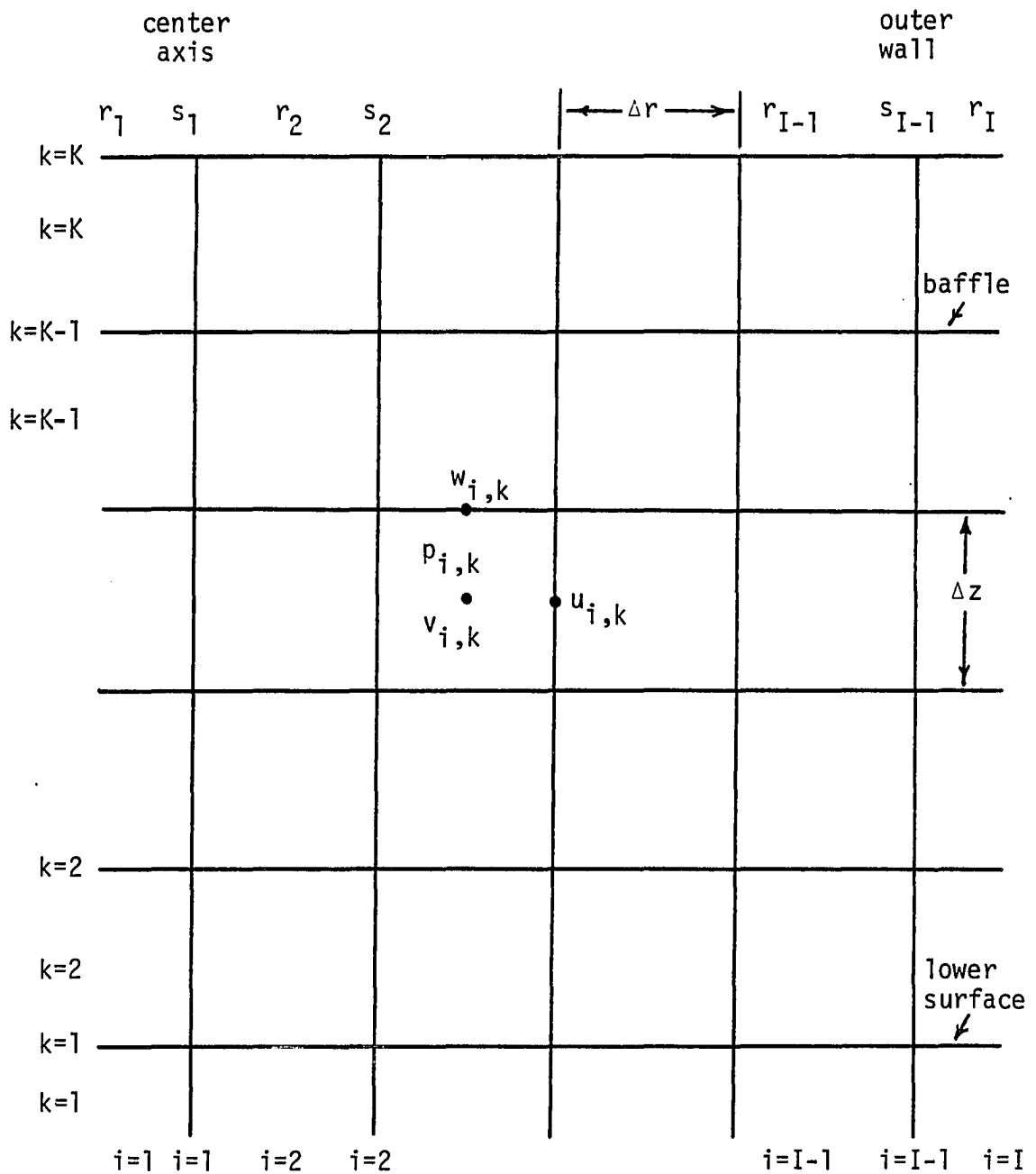


Figure 2.2. The finite difference grid on which the difference equations are based. The diagram indicates the relative placement of the dependent variables and the scheme for numbering indices.

$$\begin{aligned}
\frac{u_{i,k}^{n+1} - u_{i,k}^{n-1}}{2\Delta t} = & \left\{ \frac{1}{4\Delta r s_i} [(s_i u_{i,k} + s_{i-1} u_{i-1,k})(u_{i,k} + u_{i-1,k}) \right. \\
& - (s_{i+1} u_{i+1,k} + s_i u_{i,k})(u_{i+1,k} + u_{i,k})] \\
& + \frac{1}{4\Delta z} [(w_{i,k-1} + w_{i+1,k-1})(u_{i,k-1} + u_{i,k}) \\
& - (w_{i,k} + w_{i+1,k})(u_{i,k} + u_{i,k+1})] \\
& + \frac{1}{2} \left[\frac{v_{i,k} v_{i,k}}{r_i} + \frac{v_{i+1,k} v_{i+1,k}}{r_{i+1}} \right] \\
& + \frac{1}{\rho \Delta r} (p_{i-1,k} - p_{i,k}) \left. \right\}^n \\
& + \left\{ v \left[\frac{1}{\Delta z \Delta z} (u_{i,k-1} - 2u_{i,k} + u_{i,k+1}) \right. \right. \\
& \left. \left. - \frac{1}{\Delta z \Delta r} (w_{i+1,k} - w_{i,k} - w_{i+1,k-1} + w_{i,k-1}) \right] \right\}^{n-1} \quad (2.12)
\end{aligned}$$

$$\begin{aligned}
\frac{v_{i,k}^{n+1} - v_{i,k}^{n-1}}{2\Delta t} = & \left\{ \frac{1}{2r_i \Delta r} [s_{i-1} u_{i-1,k} (v_{i-1,k} + v_{i,k}) \right. \\
& - s_i u_{i,k} (v_{i,k} + v_{i+1,k})] \\
& + \frac{1}{2\Delta z} [w_{i,k-1} (v_{i,k-1} + v_{i,k}) - w_{i,k} (v_{i,k} + v_{i,k+1})] \\
& \left. - \frac{1}{2r_i r_i} v_{i,k} [s_{i-1} u_{i-1,k} + s_i u_{i,k}] \right\}^n
\end{aligned}$$

$$\begin{aligned}
& + \left\{ v \left[\frac{1}{\Delta r \Delta r} \left(\frac{r_{i+1} v_{i+1,k} - r_i v_{i,k}}{s_i} - \frac{r_i v_{i,k} - r_{i-1} v_{i-1,k}}{s_{i-1}} \right) \right. \right. \\
& \left. \left. + \frac{1}{\Delta z \Delta z} (v_{i,k-1} - 2v_{i,k} + v_{i,k+1}) \right] \right\}^{n-1} \quad (2.13)
\end{aligned}$$

$$\begin{aligned}
\frac{w_{i,k}^{n+1} - w_{i,k}^{n-1}}{2\Delta t} = & \left\{ \frac{1}{4r_i \Delta r} [s_{i-1}(u_{i-1,k} + u_{i-1,k+1})(w_{i-1,k} + w_{i,k}) \right. \\
& - s_i(u_{i,k} + u_{i,k+1})(w_{i,k} + w_{i+1,k})] \\
& + \frac{1}{4\Delta z} [(w_{i,k-1} + w_{i,k})(w_{i,k-1} + w_{i,k}) \\
& - (w_{i,k+1} + w_{i,k})(w_{i,k+1} + w_{i,k})] \\
& \left. + \frac{1}{\rho \Delta z} (p_{i,k} - p_{i,k+1}) \right\}^n \\
& + \left\{ v \left[\frac{1}{r_i \Delta r \Delta r} (s_i [w_{i+1,k} - w_{i,k}] - s_{i-1} [w_{i,k} - w_{i-1,k}]) \right. \right. \\
& - \frac{1}{r_i \Delta r \Delta z} (s_i [u_{i,k+1} - u_{i,k}] \\
& \left. \left. - s_{i-1} [u_{i-1,k+1} - u_{i-1,k}]) \right] \right\}^{n-1} \quad (2.14)
\end{aligned}$$

$$\frac{1}{r_i \Delta r} (u_{i,k} s_i - u_{i-1,k} s_{i-1}) + \frac{1}{\Delta z} (w_{i,k} - w_{i,k-1}) = 0 \quad (2.15)$$

Both the space and time differences are centered so that the equations possess second order accuracy. The particular form of the differences

is the two-dimensional analog of the scheme used by Williams (1969) to simulate thermal convection in a rotating annulus. That study demonstrated that the scheme is computationally stable and accurate for long term integrations.

2.4 Method of Solution

Eqs. 2.12 - 2.14 are prediction equations used to find the velocity components u , v and w at a new time level $n+1$ based on current values (time level n) and past values (time level $n-1$) of all variables. The expressions on the left-hand sides of those equations represent the average time derivatives of the velocity components from time level $n-1$ to $n+1$. Except for the viscosity terms, which are taken at time level $n-1$ to maintain computational stability (see Haltiner and Williams, 1980, p. 155), the terms on the right-hand side of these equations apply at time level n . Hence, time derivatives computed at time level n are used to advance the fields from time level $n-1$ to $n+1$; next, time derivatives computed at time level $n+1$ will be used to advance the fields from time level n to $n+2$, and so forth. This advancement scheme has been appropriately named the "leap frog" method and is one of the simplest and most accurate of the explicit schemes available (Kurihara, 1965).

The only variable which remains to be computed is the pressure, p , for which there is no explicit prediction equation since incompressibility has been assumed. There is, however, a constraint on the velocity fields, namely Eq. 2.15, as a result of the incompressibility assumption. As long as the boundary conditions are properly specified,

there is a unique pressure field at time level n which, by Eqs. 2.12 and 2.14, will cause the radial and vertical velocity fields at time level $n+1$ to satisfy Eq. 2.15. The determination of that pressure field involves the solution of a system of simultaneous linear equations and is therefore an implicit computation.

A convenient method for performing the pressure calculation is the following. Eqs. 2.12 and 2.14 are first used without the pressure terms to predict the temporary velocity components $\tilde{u}_{i,k}^{n+1}$ and $\tilde{w}_{i,k}^{n+1}$. Then, the part of the equations which remains to be solved is

$$u_{i,k}^{n+1} = \tilde{u}_{i,k}^{n+1} + \frac{2\Delta t}{\rho\Delta r} (p_{i,k}^n - p_{i+1,k}^n) \quad (2.16)$$

$$w_{i,k}^{n+1} = \tilde{w}_{i,k}^{n+1} + \frac{2\Delta t}{\rho\Delta z} (p_{i,k}^n - p_{i,k+1}^n) \quad (2.17)$$

and this will be done once pressure is computed. To get the pressure, Eqs. 2.16 and 2.17 are substituted into Eq. 2.15, which gives

$$\begin{aligned} & \frac{1}{\rho r_i \Delta r \Delta r} [s_{i-1} (p_{i-1,k}^n - p_{i,k}^n) - s_i (p_{i,k}^n - p_{i+1,k}^n)] \\ & + \frac{1}{\rho \Delta z \Delta z} (p_{i,k-1}^n - 2p_{i,k}^n + p_{i,k+1}^n) \\ & = \left[\frac{1}{r_i \Delta r} (s_i \tilde{u}_{i,k}^{n+1} - s_{i-1} \tilde{u}_{i-1,k}^{n+1}) \right. \\ & \left. + \frac{1}{\Delta z} (\tilde{w}_{i,k}^{n+1} - \tilde{w}_{i,k-1}^{n+1}) \right] \frac{1}{2\Delta t} \end{aligned} \quad (2.18)$$

The left side of Eq. 2.18 is a five-point Laplacian of pressure centered on $p_{i,k}^n$ while the right side is the negative divergence of the temporary velocity components divided by $2\Delta t$, and is also centered on the point $p_{i,k}^n$. When Eq. 2.18 is written in matrix form for the entire domain, it becomes $AP = -D$, where A is a square coefficient matrix containing only constant (in time) geometrical factors, P is a vector containing all interior points $p_{i,k}^n$ where $2 \leq i \leq I-1$ and $2 \leq k \leq K-1$, and D is a vector containing all the temporary divergences for the same points. One straightforward method of solving this matrix equation would be to compute A^{-1} , which need be done only once since it is constant for all time, and carry out the simple matrix multiplication $P = -A^{-1}D$ each time step. However, even for the moderate grid size of $I = 32$, $K = 62$, used in this study, P and D have $30 \times 60 = 1800$ points and A^{-1} has $1800 \times 1800 = 3,240,000$ points. This number is far too large to fit in any high-speed computer memory and this method would require the use of low speed memory every timestep. An alternative method, which has been used in this model, takes into account the fact that A is a very sparse matrix so that A^{-1} , while not being sparse, contains mostly redundant information. If the elements of P and D are written in the order of the sequence $p_{2,2}, p_{3,2}, \dots, p_{I-1,2}, p_{2,3}, p_{3,3}, \dots, p_{I-2,K-1}, p_{I-1,K-1}$, then A is a tridiagonal matrix with two additional diagonals located $I-2$ columns away on either side of the main diagonal. Then, if the system $AP = -D$ is solved by Gaussian Elimination, all the zero elements of A which lie beyond the outer diagonals can be ignored thereby greatly reducing the amount of

computational work. The standard Fortran subroutines DECOMP and SOLVE have been chosen for this purpose. These software packages are described in Forsythe et al. (1977) and are resident routines at the National Center for Atmospheric Research (NCAR NSSL Manual, 1975). By carrying out that part of Gaussian elimination which depends only on A, DECOMP decomposes A into a form containing the multipliers and pivot information, and ready for rapid solution of the matrix equation. For this case, this results in a banded matrix having a bandwidth of $2(I-2) + 1$. Since the order of A is $(I-2)(K-2)$, the band, which contains the only nonzero elements of the matrix, has approximately $[2(I-2) + 1](I-2)(K-2)$ elements. For the above example with $I = 32$ and $K = 62$, this number is 109800 which is a substantial improvement over the number in A^{-1} . These points are computed once and stored in a rectangular array for the duration of the run. The subroutine SOLVE, which has been slightly modified to accommodate only the band array and not the entire decomposed version of A, is called each timestep and rapidly computes the current solution P from the current vector D and the constant band array. Once the pressure for time level n is found, the radial and vertical velocities for time level n+1 are computed from Eqs. 2.16 and 2.17, and Eq. 2.15 is automatically satisfied. This completes the advancement of all dependent variables by one time level.

Many methods which have been used in numerical models to invert an elliptic equation such as Eq. 2.18 employ a successive relaxation technique in which the correct solution is approached asymptotically

through iteration (Haltiner and Williams, 1980). Such schemes have the advantage of requiring very little computer storage but involve a compromise between speed and accuracy. When near exact solutions are needed, relaxation methods require many iterations causing them to be inefficient. The method which has been used for this study is both accurate (to computer round-off error) and fast, the pressure calculations requiring only about one-third of the total time involved in the model integration.

It was mentioned above that a spatial computational mode appears in the numerical solution and can be sufficiently damped by the use of viscosity terms in the numerical equations. This computational mode arises because the hydrodynamic equations, which contain only first order derivatives in the advective, pressure and divergence terms of the continuous equations, are raised to second order when cast in difference form, thereby permitting the second solution. Since the numerical time differences have likewise been raised from first to second order, a spurious computational mode also appears in time between successive time levels. This is damped in the present model by applying a weak filter every timestep. The filter has the form

$$\bar{q}_{i,j}^n = q_{i,j}^n + \delta(\bar{q}_{i,j}^{n-1} - 2q_{i,j}^n + q_{i,j}^{n+1}),$$

where $q = u, v, \text{ or } w$, and is used to modify the velocity components at time level n after they have been computed for time level $n+1$. The coefficient δ controls the strength of the filter with $\delta = 0$ causing no filtering and $\delta = 0.5$ causing complete filtering of the $2\Delta t$ mode

(Asselin, 1972). A value of $\delta = 0.1$ has been used for this model. Since the axisymmetric model is used to find a steady-state solution, the dependent variables of two consecutive time levels approach each other asymptotically with time so that time filtering does not affect the final solution.

2.5 Spatial and Temporal Boundary Conditions

The model equations 2.12, 2.13, 2.14 and 2.18 may be used to compute new values of only the interior variables since the spatial derivatives are represented by centered differences. The variables at the upper, lower, inner, and outer boundaries must be assigned by other methods which depend on the physical boundary conditions appropriate to the problem. One basic approximation employed in this model which determines many of the boundary conditions is that the bottom, top, and sides of the vortex chamber exert no tangential force on the fluid. This free-slip condition has been adopted for the following reasons. Although real fluids actually have zero slip at rigid boundaries due to viscosity, it is generally true that in high Reynolds number flow, such as that in the vortex simulator, only a narrow layer next to the boundary is significantly retarded. Across this layer, known as the boundary layer, the fluid makes a rapid transition from zero velocity on the boundary to finite velocity similar to that which would occur if the flow were inviscid. Outside the boundary layer, the tangential stress exerted by the boundary is insignificant compared to the inertial forces. The existence of the boundary layer was first hypothesized by Prandtl in 1904 and has

subsequently been verified experimentally for a wide variety of low viscosity flow fields (Batchelor, 1967). Because secondary vortices, the object of interest of this study, are not a boundary layer phenomenon but occur in the free interior flow, to numerically resolve the boundary layer with a high density grid is considered unnecessarily complicated. Without that resolution, a free-slip boundary condition provides the most accurate simulation of the interior flow.

Some further comments should be made concerning the application of the free-slip condition to the individual boundaries in the model. An additional effect which the lower boundary stress has on the vortex is the inducement of a radial inflow in the boundary layer. This phenomenon is readily observed in measurements made by Baker (1981) of the simulator flow for radial distances less than about 30 cm where approximate cyclostrophic balance occurs above the boundary layer. The secondary circulation arises because the viscous stress of the surface retards the azimuthal velocity thereby upsetting the approximate cyclostrophic balance and allowing the radial pressure force to drive air into the center of the vortex. This effect is eliminated by the assumption of a free-slip condition; however, since it is of the same magnitude and confined just to the narrow boundary layer as the other viscous boundary effects, it is considered to be equally negligible. The outer radial boundary of the computational domain has been chosen to coincide with the radius of the updraft hole, rather than the outer wall of the simulator, and is therefore a fictitious boundary. The grid is abbreviated in this way in order to confine the

computations to the central region where the secondary vortices are present. A free-slip condition is naturally the most appropriate for this boundary; then the only artificial effect of the boundary is the forcing of zero radial velocity at that radius. This method was used by Rotunno (1977) and realistic simulations in the central region were obtained. The no-slip upper boundary condition is perhaps the most difficult one to justify since the top is an outflow boundary and the honeycomb baffle forces the air to exit vertically. However, the viscous drag of the baffle does not appear to be noticed very far upstream as the azimuthal velocity remains nearly constant with height until only a few centimeters below the top. Thus, a free-slip condition appears to be reasonable. Probably the major influence that the baffle has on the flow in the simulator is the removal (at the top) of the central pressure deficit associated with the azimuthal rotation (Church et al., 1979). In this model, the pressure at the upper boundary may be independently specified which allows this effect to be included.

The free-slip condition having thus been rationalized, the details of specifying numerical boundary values for all variables are now listed.

A. Inner Boundary

None of the variables at the inner boundary enter into the computations since they are always multiplied by the value of the center radius which is zero. (The one exception to this occurs in the azimuthal friction component where the center radius is multiplied by its reciprocal making the quantity indeterminate. The proper effect

of azimuthal stress at the center is obtained by subtracting the quantity $4\nu v_{2,k}/\Delta r \Delta r$ from the tendency of $v_{2,k}$ each timestep.) The variables are nevertheless assigned special values for the purpose of graphic representation. Following from axial symmetry, the assignments $u_{1,k} = 0$, $v_{1,k} = -v_{2,k}$, $w_{1,k} = w_{2,k}$, and $p_{1,k} = p_{2,k}$ for $1 \leq k \leq K$ are made upon the completion of a timestep.

B. Lower Boundary

From the free-slip condition, $u_{i,1} = u_{i,2}$ and $v_{i,1} = v_{i,2}$. The impermeability of the boundary dictates $w_{i,1} = 0$, and $p_{i,1} = p_{i,2}$ is set only for graphic representation. These assignments apply for $2 \leq i \leq I$ and are made at the end of each timestep.

C. Outer Boundary

The outer boundary contains two regions, the lower one coinciding with the inflow region and the upper one representing an impermeable wall. The division between the regions occurs at the same height as a "w" point whose vertical index will be denoted as L . For $2 \leq k \leq L$, $u_{I-1,k}$ and $v_{I,k}$ are specified and constant for all time, thus determining the volume flow rate and the inflow circulation. Vertical velocity is chosen so that the azimuthal component of vorticity of the flow entering the chamber is zero. The importance of this condition was discussed in Rotunno (1977) and the zero vorticity inflow is appropriate to the vortex simulator outside the viscous boundary layers. The numerical form of the vertical velocity is $w_{I,k} = w_{I-1,k} + (u_{I-1,k+1} - u_{I-1,k})\Delta r/\Delta z$. For $L < k < K$, the boundary

conditions are $u_{I-1,k} = 0$, $v_{I,k} = v_{I-1,k}(r_I/r_{I-1})$, and $w_{I,k} = w_{I-1,k}$, the latter two being the free-slip conditions. The pressure at the outer boundary has no bearing on the flow but is assigned for graphic representation as $p_{I,k} = p_{I-1,k}$.

D. Upper Boundary

The upper boundary is the most complicated as it may be an outflow and inflow boundary simultaneously, and exactly what portion is inflow is not in general known a priori. Special care must be taken in order that flow disturbances impinging on the open boundary be allowed to pass out of the domain without being appreciably reflected back into the interior. If this is not done, a spurious computational mode is likely to be generated. The possibility of this occurring is well known and many methods have been devised for minimizing false reflections at the boundaries (e.g., Orlanski, 1976; Lilly, 1981). Most of the methods use the advective equation with an upstream difference to extrapolate information from the interior to the boundary, and the various methods differ primarily in the way the characteristic advective speed is chosen. For the case of the vortex simulator, the selection of an appropriate boundary condition is relatively easy since neither sound nor gravity waves can exist in the flow. The advective extrapolation technique is used with the local vertical velocity w chosen as the representative advective speed. The upper boundary conditions are written in numerical form as follows. For $2 \leq i \leq I-1$,

$$u_{i,K}^{n+1} = 0 \quad \text{if } c < 0$$

$$v_{i,K}^{n+1} = 0 \quad \text{if } d < 0$$

$$u_{i,K}^{n+1} = u_{i,K}^{n-1} \frac{(1-c)}{(1+c)} + u_{i,K-1}^n \frac{2c}{(1+c)} \quad \text{if } c \geq 0$$

$$v_{i,K}^{n+1} = v_{i,K}^{n-1} \frac{(1-d)}{(1+d)} + v_{i,K-1}^n \frac{2d}{(1+d)} \quad \text{if } d \geq 0$$

$$w_{i,K}^{n+1} = w_{i,K-1}^{n+1}$$

where

$$c = \frac{\Delta t}{2\Delta z} (w_{i,K-1}^n + w_{i+1,K-1}^n)$$

and

$$d = \frac{\Delta t}{\Delta z} w_{i,K-1}^n$$

Unlike the other boundaries where a simple assignment of variables based on one time level is possible, computation of the upper boundary conditions for horizontal velocity requires using variables at three time levels simultaneously. When a steady state is approached, the choice for the horizontal velocity components converges to the free-slip condition. The top pressure $p_{i,K}$, as mentioned before, must be specified and is set to zero at all radii for these experiments.

E. Initial Temporal Boundary

Because the desired solution of the axisymmetric model is the final steady state result, the actual values assigned initially to the dependent variables are inconsequential. A value of zero has arbitrarily been chosen for all interior variables for time levels $n = 1$ and $n = 2$ while the spatial boundary values are set according to the conditions previously mentioned. Thus, all the quantities necessary for performing the first integration and determining the solution at $n = 3$ are provided.

2.6 General Development of the Solution

After one iteration, the solution at $n = 3$ has a fully developed radial and vertical flow structure because continuity is always satisfied, and a radial inflow has been imposed. The swirling velocity, on the other hand, requires many iterations to fully penetrate the domain. As this takes place, the radial and vertical velocity fields continually readjust under the influence of the developing swirling flow. After several hundred iterations, the solution has very nearly reached its steady state value. The model is typically integrated out to several times this amount, however, in order to provide as close a solution to the true steady state solution as is reasonably possible.

2.7 Model Testing and Verification

In order to insure the validity of the axisymmetric model and to locate possible errors in the formulation of the equations or in

the computer code, three tests were devised whereby solutions generated by the model could be compared to known results. In the first and simplest test, the upper, lower, and outer boundaries were made everywhere impermeable so that the model would simulate the flow in an enclosed cylindrical container. A solid-body rotation with no radial or axial motion was imposed on the flow as the initial condition and the free-slip condition was used at all boundaries. As the model was integrated forward in time, the flow remained unchanged and the associated pressure field was constant with height and parabolic with radius. This results is in exact accordance with the analytic solution.

Because the first test considered a simplistic flow, it could verify only a portion of the model. A second test was performed using a fully general flow for which all three velocity components and their spatial and time derivatives were nonzero. The same boundary conditions were used as before except that the free-slip condition was replaced by no-slip on all boundaries. The initial condition consisted of solid-body rotation in the interior fluid and a 10% faster rotation of the cylindrical container. Tangential viscous stress exerted by the container walls caused the fluid to spin up and, in the process, develop inertial waves. All experimental parameters including fluid density and viscosity, dimensions of the container, and angular velocity were chosen to match those used in a previous numerical simulation of this problem described in Warn-Varnas et al. (1978). Both experiments used the same finite difference equations and grids.

A comparison was made between the test results and those reported in Warn-Varnas et al. and no difference was apparent.

For the third test, the model was set up to resemble the tornado simulator. The same conditions as those described in Section 2.5 were used with two exceptions: (1) instead of imposing a radially-constant pressure at the top, the pressure was chosen to satisfy the condition of cyclostrophic balance with the azimuthal flow; and, (2) the vertical derivative of azimuthal velocity at the top of the model was set to zero in regions where a downdraft existed, as well as where updrafts occurred. This allowed a direct comparison to be made with the numerical simulations of the laboratory simulator by Rotunno (1977) which employed the same conditions. Although the two models use completely different formulations of the fluid equations, their mutual agreement was nearly exact.

The performance of the axisymmetric model in these tests demonstrates the accuracy and validity of its formulation and computer coding.

Chapter 3

DESCRIPTION OF THE LINEAR MODEL

The linear model is necessarily very similar in design to the axisymmetric model. For the linearization process to be strictly valid, it is important that the same form of the equations and the same boundary conditions be used wherever appropriate. Hence, most of the methods and terminology described in Chapter 2, including the coordinate system and variables, will apply here. To begin with, the model development proceeds from Eqs. 2.4 - 2.7.

3.1 Linearization of the Hydrodynamic Equations

The goal here is to derive the equations which describe the behavior of small-amplitude, azimuthally varying perturbations of an axisymmetric flow which is in steady-state equilibrium. To this end, the dependent variables are each expressed as the sum of their azimuthal average and the departure from the average:

$$u(r, \theta, z, t) = \bar{u}(r, z, t) + u'(r, \theta, z, t)$$

$$v(r, \theta, z, t) = \bar{v}(r, z, t) + v'(r, \theta, z, t)$$

$$w(r, \theta, z, t) = \bar{w}(r, z, t) + w'(r, \theta, z, t)$$

$$p(r, \theta, z, t) = \bar{p}(r, z, t) + p'(r, \theta, z, t)$$

where the average is defined, for example, as

$$\bar{u}(r, z, t) = \frac{1}{2\pi} \int_0^{2\pi} u(r, \theta, z, t) d\theta$$

(The time dependence of the azimuthal mean quantities is retained here as this step is purely a matter of definition. Its omission will be justified later.) The above expressions are substituted into Eqs.

2.4 - 2.7 to give

$$\begin{aligned} \frac{\partial \bar{u}}{\partial t} + \frac{\partial u'}{\partial t} = & -\frac{1}{r} \frac{\partial}{\partial r} (\bar{u}ur) - \frac{2}{r} \frac{\partial}{\partial r} (\bar{u}u'r) - \frac{1}{r} \frac{\partial}{\partial r} (u'u'r) \\ & - \frac{1}{r} \frac{\partial}{\partial \theta} (\bar{u}v') - \frac{1}{r} \frac{\partial}{\partial \theta} (u'\bar{v}) - \frac{1}{r} \frac{\partial}{\partial \theta} (u'v') - \frac{\partial}{\partial z} (\bar{u}w) \\ & - \frac{\partial}{\partial z} (\bar{u}w') - \frac{\partial}{\partial z} (u'\bar{w}) - \frac{\partial}{\partial z} (u'w') - \frac{1}{\rho} \frac{\partial \bar{p}}{\partial r} - \frac{1}{\rho} \frac{\partial p'}{\partial r} \\ & + \frac{\bar{v}v}{r} + 2\frac{\bar{v}v'}{r} + \frac{v'v'}{r} + v \left[\frac{\partial^2 \bar{u}}{\partial z^2} - \frac{\partial^2 \bar{w}}{\partial z \partial r} + \frac{\partial^2 u'}{\partial z^2} - \frac{\partial^2 w'}{\partial z \partial r} \right. \\ & \left. + \frac{1}{r^2} \frac{\partial^2 u'}{\partial \theta^2} - \frac{1}{r^2} \frac{\partial}{\partial r} \left(r \frac{\partial v'}{\partial \theta} \right) \right] \end{aligned} \quad (3.1)$$

$$\begin{aligned} \frac{\partial \bar{v}}{\partial t} + \frac{\partial v'}{\partial t} = & -\frac{1}{r} \frac{\partial}{\partial r} (\bar{u}vr) - \frac{1}{r} \frac{\partial}{\partial r} (\bar{u}v'r) - \frac{1}{r} \frac{\partial}{\partial r} (u'\bar{v}r) \\ & - \frac{1}{r} \frac{\partial}{\partial r} (u'v'r) - \frac{2}{r} \frac{\partial}{\partial \theta} (\bar{v}v') - \frac{1}{r} \frac{\partial}{\partial \theta} (v'v') - \frac{\partial}{\partial z} (\bar{v}w) \\ & - \frac{\partial}{\partial z} (\bar{v}w') - \frac{\partial}{\partial z} (v'\bar{w}) - \frac{\partial}{\partial z} (v'w') - \frac{1}{r\rho} \frac{\partial p'}{\partial \theta} - \frac{\bar{u}v}{r} \\ & - \frac{\bar{u}v'}{r} - \frac{u'\bar{v}}{r} - \frac{u'v'}{r} + v \left[\frac{\partial^2 \bar{v}}{\partial z^2} + \frac{\partial}{\partial r} \left(\frac{1}{r} \frac{\partial}{\partial r} (r\bar{v}) \right) \right. \\ & \left. - \frac{1}{r} \frac{\partial^2 w'}{\partial z \partial \theta} + \frac{\partial^2 v'}{\partial z^2} + \frac{\partial}{\partial r} \left(\frac{1}{r} \frac{\partial}{\partial r} (rv') \right) - \frac{\partial}{\partial r} \left(\frac{1}{r} \frac{\partial u'}{\partial \theta} \right) \right] \end{aligned} \quad (3.2)$$

$$\begin{aligned}
\frac{\partial \bar{w}}{\partial t} + \frac{\partial w'}{\partial t} = & -\frac{1}{r} \frac{\partial}{\partial r} (\bar{u}wr) - \frac{1}{r} \frac{\partial}{\partial r} (\bar{u}w'r) - \frac{1}{r} \frac{\partial}{\partial r} (u'\bar{w}r) \\
& - \frac{1}{r} \frac{\partial}{\partial r} (u'w'r) - \frac{1}{r} \frac{\partial}{\partial \theta} (\bar{v}w') - \frac{1}{r} \frac{\partial}{\partial \theta} (v'\bar{w}) \\
& - \frac{1}{r} \frac{\partial}{\partial \theta} (v'w') - \frac{\partial}{\partial z} (\bar{w}w) - 2 \frac{\partial}{\partial z} (\bar{w}w') - \frac{\partial}{\partial z} (w'w') \\
& - \frac{1}{\rho} \frac{\partial \bar{p}}{\partial z} - \frac{1}{\rho} \frac{\partial p'}{\partial z} + v \left[-\frac{1}{r} \frac{\partial}{\partial r} (r \frac{\partial \bar{u}}{\partial z}) + \frac{1}{r} \frac{\partial}{\partial r} (r \frac{\partial \bar{w}}{\partial r}) \right. \\
& \left. - \frac{1}{r} \frac{\partial}{\partial r} (r \frac{\partial u'}{\partial z}) + \frac{1}{r} \frac{\partial}{\partial r} (r \frac{\partial w'}{\partial r}) + \frac{1}{r^2} \frac{\partial^2 w'}{\partial \theta^2} - \frac{1}{r} \frac{\partial^2 v'}{\partial \theta \partial z} \right] \quad (3.3)
\end{aligned}$$

$$\frac{1}{r} \frac{\partial}{\partial r} (\bar{u}r) + \frac{1}{r} \frac{\partial}{\partial r} (u'r) + \frac{1}{r} \frac{\partial \bar{v}}{\partial \theta} + \frac{1}{r} \frac{\partial v'}{\partial \theta} + \frac{\partial \bar{w}}{\partial z} + \frac{\partial w'}{\partial z} = 0 \quad (3.4)$$

In this form, the equations are simply an expanded but equivalent version of the general equations of motion and continuity.

With the objective of this exercise in mind, the following restrictive assumptions are now made:

- (1) The perturbations are vanishingly small compared to the mean variables.
- (2) The mean variables are chosen to represent an axisymmetric flow which is a steady-state solution for this problem. In practice, this solution is generated by the axisymmetric model of Chapter 2.

Under the first assumption, all terms which are second order in the perturbation quantities are negligible and can be omitted from the

equations. The remaining terms are all of the zeroth or first order in the perturbation variables. Since by definition, the azimuthal mean of a perturbation variable is zero, none of the first order terms makes any contribution to the axisymmetric flow (i.e., zeroth and first order terms are orthogonal) and thus each of the four equations is separable into a zeroth order and a first order equation. The zeroth order equations, which are identical to Eqs. 2.8 - 2.11 used in the axisymmetric model, are automatically satisfied according to the second assumption and, since the nonlinear terms have been omitted, the mean variables are constant in time. The first order equations are therefore the desired linear perturbation equations. The three momentum equations describe the tendencies of the perturbation velocity components as they interact with the steady-state axisymmetric flow, and the continuity equation imposes a constraint on the velocity components from which the perturbation pressure field may be obtained. The linear equations are written succinctly as follows.

$$\begin{aligned}
\frac{\partial u'}{\partial t} = & -\frac{2}{r} \frac{\partial}{\partial r} (\bar{u} u' r) - \frac{\bar{u}}{r} \frac{\partial v'}{\partial \theta} - \frac{\bar{v}}{r} \frac{\partial u'}{\partial \theta} - \frac{\partial}{\partial z} (\bar{u} w') - \frac{\partial}{\partial z} (u' \bar{w}) \\
& - \frac{1}{\rho} \frac{\partial p'}{\partial r} + 2 \frac{\bar{v} v'}{r} + v \left[\frac{\partial^2 u'}{\partial z^2} - \frac{\partial^2 w'}{\partial z \partial r} + \frac{1}{r^2} \frac{\partial^2 u'}{\partial \theta^2} \right. \\
& \left. - \frac{1}{r^2} \frac{\partial}{\partial r} \left(r \frac{\partial v'}{\partial \theta} \right) \right] \tag{3.5}
\end{aligned}$$

$$\begin{aligned}
\frac{\partial v'}{\partial t} = & -\frac{1}{r} \frac{\partial}{\partial r} (\bar{u}v'r) - \frac{1}{r} \frac{\partial}{\partial r} (u'\bar{v}r) - 2 \frac{\bar{v}}{r} \frac{\partial v'}{\partial \theta} - \frac{\partial}{\partial z} (\bar{w}v') \\
& - \frac{\partial}{\partial z} (v'\bar{w}) - \frac{1}{r\rho} \frac{\partial p'}{\partial \theta} - \frac{\bar{u}v'}{r} - \frac{u'\bar{v}}{r} + v \left[-\frac{1}{r} \frac{\partial^2 w'}{\partial z \partial \theta} \right. \\
& \left. + \frac{\partial^2 v'}{\partial z^2} + \frac{\partial}{\partial r} \left(\frac{1}{r} \frac{\partial}{\partial r} (rv') \right) - \frac{\partial}{\partial r} \left(\frac{1}{r} \frac{\partial u'}{\partial \theta} \right) \right] \quad (3.6)
\end{aligned}$$

$$\begin{aligned}
\frac{\partial w'}{\partial t} = & -\frac{1}{r} \frac{\partial}{\partial r} (\bar{u}w'r) - \frac{1}{r} \frac{\partial}{\partial r} (u'\bar{w}r) - \frac{\bar{v}}{r} \frac{\partial w'}{\partial \theta} - \frac{\bar{w}}{r} \frac{\partial v'}{\partial \theta} \\
& - 2 \frac{\partial}{\partial z} (\bar{w}w') - \frac{1}{\rho} \frac{\partial p'}{\partial z} + v \left[-\frac{1}{r} \frac{\partial}{\partial r} \left(r \frac{\partial u'}{\partial z} \right) \right. \\
& \left. + \frac{1}{r} \frac{\partial}{\partial r} \left(r \frac{\partial w'}{\partial r} \right) + \frac{1}{r^2} \frac{\partial^2 w'}{\partial \theta^2} - \frac{1}{r} \frac{\partial^2 v'}{\partial \theta \partial z} \right] \quad (3.7)
\end{aligned}$$

$$\frac{1}{r} \frac{\partial}{\partial r} (u'r) + \frac{1}{r} \frac{\partial v'}{\partial \theta} + \frac{\partial w'}{\partial z} = 0 \quad (3.8)$$

It may be noted that as the behavior of a linear solution is independent of its amplitude, the solution may be allowed to grow large during the integration of the above equations. The relevance of the linear solution to small amplitude perturbations on the axisymmetric flow is automatically insured by the removal of the nonlinear terms.

3.2 Fourier Decomposition of the Perturbation Variables

A major objective of this study is to determine the dependency which the instability of the axisymmetric vortex has on the azimuthal scale of the perturbations. For this purpose, the perturbations are decomposed into Fourier Series and each constituent harmonic is

considered separately. This step is legitimate since the perturbations are linear, implying no interaction between individual harmonics. An important secondary benefit which arises from considering the harmonics individually is that the growth of a three-dimensional perturbation can be simulated on a two-dimensional grid in radius and height, the sinusoidal variation in θ being implicit. With this method, the θ -derivatives which appear in Eqs. 3.5 - 3.8 can be computed analytically. The Fourier decompositions are written in the following way.

$$\begin{aligned}
 u'(r, \theta, z, t) &= \operatorname{Re} \sum_{m=0}^{\infty} U_m(r, z, t) e^{im\theta} \\
 v'(r, \theta, z, t) &= \operatorname{Re} \sum_{m=0}^{\infty} V_m(r, z, t) e^{im\theta} \\
 w'(r, \theta, z, t) &= \operatorname{Re} \sum_{m=0}^{\infty} W_m(r, z, t) e^{im\theta} \\
 p'(r, \theta, z, t) &= \operatorname{Re} \sum_{m=0}^{\infty} P_m(r, z, t) e^{im\theta}
 \end{aligned} \tag{3.9}$$

where U_m , V_m , W_m , and P_m are complex coefficients, m is the azimuthal wavenumber (denoting the number of cycles in the range $0 \leq \theta \leq 2\pi$), $i = \sqrt{-1}$, and "Re" stands for the "real part of." Substituting these expressions, one wavenumber at a time, into Eqs. 3.5 - 3.8 results in each term containing the factor $e^{im\theta}$. This quantity is divided out requiring the simultaneous omission of the symbol "Re." Upon omitting the subscript m from the complex coefficients, the Fourier-decomposed linear perturbation equations become

$$\begin{aligned} \frac{\partial U}{\partial t} = & -\frac{2}{r} \frac{\partial}{\partial r} (\bar{u}Ur) - \frac{\bar{u}imV}{r} - \frac{\bar{v}imU}{r} - \frac{\partial}{\partial z} (\bar{u}W) - \frac{\partial}{\partial z} (U\bar{w}) \\ & - \frac{1}{\rho} \frac{\partial P}{\partial r} + 2 \frac{\bar{v}V}{r} + v \left[\frac{\partial^2 U}{\partial z^2} - \frac{\partial^2 W}{\partial z \partial r} - \frac{m^2}{r^2} U - \frac{im}{r^2} \frac{\partial}{\partial r} (rV) \right] \end{aligned} \quad (3.10)$$

$$\begin{aligned} \frac{\partial V}{\partial t} = & -\frac{1}{r} \frac{\partial}{\partial r} (\bar{u}Vr) - \frac{1}{r} \frac{\partial}{\partial r} (U\bar{v}r) - 2 \frac{\bar{v}imV}{r} - \frac{\partial}{\partial z} (\bar{v}W) \\ & - \frac{\partial}{\partial z} (V\bar{w}) - \frac{imP}{\rho r} - \frac{\bar{u}V}{r} - \frac{U\bar{v}}{r} + v \left[-\frac{im}{r} \frac{\partial W}{\partial z} + \frac{\partial^2 V}{\partial z^2} \right. \\ & \left. + \frac{\partial}{\partial r} \left(\frac{1}{r} \frac{\partial}{\partial r} (rV) \right) - im \frac{\partial}{\partial r} \left(\frac{U}{r} \right) \right] \end{aligned} \quad (3.11)$$

$$\begin{aligned} \frac{\partial W}{\partial t} = & -\frac{1}{r} \frac{\partial}{\partial r} (\bar{u}Wr) - \frac{1}{r} \frac{\partial}{\partial r} (U\bar{w}r) - \frac{\bar{v}imW}{r} - \frac{\bar{w}imV}{r} - 2 \frac{\partial}{\partial z} (\bar{w}W) \\ & - \frac{1}{\rho} \frac{\partial P}{\partial z} + v \left[-\frac{1}{r} \frac{\partial}{\partial r} \left(r \frac{\partial U}{\partial z} \right) + \frac{1}{r} \frac{\partial}{\partial r} \left(r \frac{\partial W}{\partial r} \right) \right. \\ & \left. - \frac{m^2}{r^2} W - \frac{im}{r} \frac{\partial V}{\partial z} \right] \end{aligned} \quad (3.12)$$

$$\frac{1}{r} \frac{\partial}{\partial r} (rU) + \frac{imV}{r} + \frac{\partial W}{\partial z} = 0 \quad (3.13)$$

(Note that the factor im , which appears in some terms, results from θ -derivatives; i.e., $\partial e^{im\theta} / \partial \theta = ime^{im\theta}$.)

The above is the continuous form of the equations which constitute the linear model. The predicted variables are now complex, and the entire three-dimensional perturbation fields can be reconstructed by recalling Eqs. 3.9. The interpretation of the complex

coefficients is facilitated by expressing them in polar form as, for example, $U = U_0 i^{-i\alpha}$ where U_0 and $-\alpha$ are the modulus and argument, respectively, of U . Then, we can write $u' = \text{Re}(U_0 i^{-i\alpha} e^{im\theta}) = \text{Re}(U_0 e^{i(m\theta-\alpha)}) = U_0 \cos(m\theta-\alpha)$. Thus, U_0 is the amplitude of the sinusoidal variation in u' at a particular height and radius. Furthermore, since $\cos(m\theta-\alpha) = 1$ at the azimuthal position $m\theta = \alpha$, the quantity α , referred to as the phase angle, is the angle (at a particular height and radius) where u' crests. The identical interpretation of amplitude and phase angle holds for all other perturbation variables.

3.3 Finite Difference Grid and Equations

The finite difference form of the linear Eqs. 3.10 - 3.13 is based on the same grid as the axisymmetric model. The design of the difference operators is likewise identical for both models, although the linear model contains additional terms which arise from azimuthal derivatives. Continuing to denote mean variables by overbars and perturbation quantities by capital letters, the finite difference form of the linear equations is written as

$$\begin{aligned} \frac{U_{i,k}^{n+1} - U_{i,k}^{n-1}}{2\Delta t} = & \left\{ \frac{1}{4s_i \Delta r} [(s_i \bar{u}_{i,k} + s_{i-1} \bar{u}_{i-1,k})(U_{i,k} + U_{i-1,k}) \right. \\ & + (s_i U_{i,k} + s_{i-1} U_{i-1,k})(\bar{u}_{i,k} + \bar{u}_{i-1,k}) \\ & \left. - (s_{i+1} \bar{u}_{i+1,k} + s_i \bar{u}_{i,k})(U_{i+1,k} + U_{i,k}) \right\} \end{aligned}$$

$$\begin{aligned}
& - (s_{i+1}U_{i+1,k} + s_i U_{i,k})(\bar{u}_{i+1,k} + \bar{u}_{i,k})] \\
& + \frac{1}{\rho \Delta r} (P_{i-1,k} - P_{i,k}) \\
& + \frac{1}{4\Delta z} [(\bar{w}_{i,k-1} + \bar{w}_{i+1,k-1})(U_{i,k-1} + U_{i,k}) \\
& + (W_{i,k-1} + W_{i+1,k-1})(\bar{u}_{i,k-1} + \bar{u}_{i,k}) \\
& - (\bar{w}_{i,k} + \bar{w}_{i+1,k})(U_{i,k} + U_{i,k+1}) \\
& - (W_{i,k} + W_{i+1,k})(\bar{u}_{i,k} + \bar{u}_{i,k+1})] \\
& - \frac{im}{2s_i} [\bar{u}_{i,k}(V_{i,k} + V_{i+1,k}) + U_{i,k}(\bar{v}_{i,k} + \bar{v}_{i+1,k})] \\
& + \left. \frac{\bar{v}_{i,k}V_{i,k}}{r_i} + \frac{\bar{v}_{i+1,k}V_{i+1,k}}{r_{i+1}} \right\}^n \\
& + \left\{ v \left[\frac{1}{\Delta z \Delta z} (U_{i,k-1} - 2U_{i,k} + U_{i,k+1}) \right. \right. \\
& - \frac{1}{\Delta r \Delta z} (W_{i+1,k} - W_{i,k} - W_{i+1,k-1} + W_{i,k-1}) \\
& \left. \left. + \frac{im}{s_i s_i} (imU_{i,k} - \frac{1}{\Delta r} [r_{i+1}V_{i+1,k} - r_i V_{i,k}]) \right] \right\}^{n-1}
\end{aligned} \tag{3.14}$$

$$\begin{aligned}
\frac{v_{i,k}^{n+1} - v_{i,k}^{n-1}}{2\Delta t} = & \left\{ \frac{s_{i-1}}{2r_i \Delta r} [\bar{u}_{i-1,k}(v_{i-1,k} + v_{i,k}) \right. \\
& + U_{i-1,k}(\bar{v}_{i-1,k} + \bar{v}_{i,k})] \\
& - \frac{s_i}{2r_i \Delta r} [\bar{u}_{i,k}(v_{i,k} + v_{i+1,k}) \\
& + U_{i,k}(\bar{v}_{i,k} + \bar{v}_{i+1,k})] - \frac{imP_{i,k}}{\rho r_i} \\
& + \frac{1}{2\Delta z} [\bar{w}_{i,k-1}(v_{i,k-1} + v_{i,k}) \\
& + W_{i,k-1}(\bar{v}_{i,k-1} + \bar{v}_{i,k}) - \bar{w}_{i,k}(v_{i,k} + v_{i,k+1}) \\
& - W_{i,k}(\bar{v}_{i,k} + \bar{v}_{i,k+1})] - \frac{2im}{r_i} \bar{v}_{i,k} v_{i,k} \\
& - \frac{1}{2r_i r_j} [\bar{v}_{i,k}(s_{i-1}U_{i-1,k} + s_i U_{i,k}) \\
& + v_{i,k}(s_{i-1}\bar{u}_{i-1,k} + s_i \bar{u}_{i,k})] \left. \right\}^n \\
& + \left\{ v \left[\frac{1}{s_i \Delta r \Delta r} (r_{i+1}v_{i+1,k} - r_i v_{i,k}) \right. \right. \\
& - \frac{1}{s_{i-1} \Delta r \Delta r} (r_i v_{i,k} - r_{i-1} v_{i-1,k}) \\
& + \frac{1}{\Delta z \Delta z} (v_{i,k-1} - 2v_{i,k} + v_{i,k+1}) \\
& \left. \left. - \frac{im}{\Delta r} \left(\frac{U_{i,k}}{s_i} - \frac{U_{i-1,k}}{s_{i-1}} \right) - \frac{im}{r_i \Delta z} (W_{i,k} - W_{i,k-1}) \right] \right\}^{n-1}
\end{aligned}
\tag{3.15}$$

$$\begin{aligned}
\frac{W_{i,k}^{n+1} - W_{i,k}^{n-1}}{2\Delta t} = & \left\{ \frac{s_{i-1}}{4r_i\Delta r} [\bar{u}_{i-1,k} + \bar{u}_{i-1,k+1}](W_{i-1,k} + W_{i,k}) \right. \\
& + (U_{i-1,k} + U_{i-1,k+1})(\bar{w}_{i-1,k} + \bar{w}_{i,k}) \\
& - \frac{s_i}{4r_i\Delta r} [(\bar{u}_{i,k} + \bar{u}_{i,k+1})(W_{i,k} + W_{i+1,k}) \\
& + (U_{i,k} + U_{i,k+1})(\bar{w}_{i,k} + \bar{w}_{i+1,k})] \\
& + \frac{1}{\rho\Delta z} (P_{i,k} - P_{i,k+1}) \\
& + \frac{1}{2\Delta z} [(\bar{w}_{i,k-1} + \bar{w}_{i,k})(W_{i,k-1} + W_{i,k}) \\
& - (\bar{w}_{i,k} + \bar{w}_{i,k+1})(W_{i,k} + W_{i,k+1})] \\
& - \frac{im}{2r_i} [\bar{w}_{i,k}(V_{i,k} + V_{i,k+1}) \\
& \left. + W_{i,k}(\bar{v}_{i,k} + \bar{v}_{i,k+1}) \right] \Big\}^n \\
& + \left\{ \frac{v}{r_i} \left[\frac{1}{\Delta r\Delta r} (s_i[W_{i+1,k} - W_{i,k}] \right. \right. \\
& - s_{i-1}[W_{i,k} - W_{i-1,k}]) \\
& \left. - \frac{1}{\Delta r\Delta z} (s_i[U_{i,k+1} - U_{i,k}] - s_{i-1}[U_{i-1,k+1} - U_{i-1,k}]) \right]
\end{aligned}$$

$$+ \operatorname{im} \left(\frac{\operatorname{im} W_{i,k}}{r_i} - \frac{1}{\Delta Z} [V_{i,k+1} - V_{i,k}] \right) \Bigg\}^{n-1} \quad (3.16)$$

$$\begin{aligned} \frac{1}{r_i \Delta r} (s_i U_{i,k} - s_{i-1} U_{i-1,k}) + \frac{1}{\Delta Z} (W_{i,k} - W_{i,k-1}) \\ + \frac{\operatorname{im} V_{i,k}}{r_i} = 0 \end{aligned} \quad (3.17)$$

3.4 Method of Solution

The linear finite difference equations are integrated by a numerical technique exactly paralleling that of the axisymmetric model. Eqs. 3.14 - 3.16 are first solved with the omission of the pressure terms to obtain the temporary velocity fields $\tilde{U}_{i,k}^{n+1}$, $\tilde{V}_{i,k}^{n+1}$ and $\tilde{W}_{i,k}^{n+1}$. The final nondivergent velocity fields are related to the temporary velocities by the expressions

$$U_{i,k}^{n+1} = \tilde{U}_{i,k}^{n+1} + \frac{2\Delta t}{\rho \Delta r} (p_{i,k}^n - p_{i+1,k}^n) \quad (3.18)$$

$$V_{i,k}^{n+1} = \tilde{V}_{i,k}^{n+1} - \frac{2\Delta t}{\rho r_i} \operatorname{im} p_{i,k}^n \quad (3.19)$$

$$W_{i,k}^{n+1} = \tilde{W}_{i,k}^{n+1} + \frac{2\Delta t}{\rho \Delta Z} (p_{i,k}^n - p_{i,k+1}^n) \quad (3.20)$$

Before they can be computed, the pressure is first obtained from

$$\frac{1}{\rho r_i \Delta r \Delta r} \left[s_{i-1} (p_{i-1,k}^n - p_{i,k}^n) - s_i (p_{i,k}^n - p_{i+1,k}^n) \right]$$

$$\begin{aligned}
& + \frac{1}{\rho \Delta z \Delta z} \left(p_{i,k-1}^n - 2p_{i,k}^n + p_{i,k+1}^n \right) - \frac{m^2 p_{i,k}^n}{\rho r_i r_i} \\
& = \left[\frac{1}{r_i \Delta r} \left(s_i \tilde{u}_{i,k}^{n+1} - s_{i-1} \tilde{u}_{i-1,k}^{n+1} \right) + \frac{im \tilde{v}_{i,k}^{n+1}}{r_i} \right. \\
& \quad \left. + \frac{1}{\Delta z} \left(\tilde{w}_{i,k}^{n+1} - \tilde{w}_{i,k-1}^{n+1} \right) \right] \frac{1}{2\Delta t} \tag{3.21}
\end{aligned}$$

which is derived by substituting Eqs. 3.18 - 3.20 into Eq. 3.17. Eq. 3.21 represents a system of simultaneous linear equations and is solved by Gaussian elimination as described in Chapter 2. Having thus obtained $p_{i,k}^n$, Eqs. 3.18 - 3.20 are evaluated thereby completing the advancement of all interior variables by one time step.

The linear model, like the axisymmetric one, requires a weak filter between successive time levels to prevent the development of a computational mode. The filter used for this purpose is

$$\bar{Q}_{i,k}^n = Q_{i,k}^n \left(\frac{\bar{Q}_{i,k}^{n-1} Q_{i,k}^{n+1}}{Q_{i,k}^n Q_{i,k}^n} \right)^\delta$$

where Q denotes U , V or W and the exponent δ is the strength of the filter with $\alpha = 0$ causing no filtering and $\delta = 0.5$ causing complete filtering of the $2\Delta t$ mode. It will be noted that, while the filter used for the axisymmetric model tends to pull the solution at time level n toward the arithmetic mean of the solutions at $n-1$ and $n+1$, the filter shown here pulls it toward their geometric mean. This

choice of a filter is the most appropriate for a solution which varies exponentially with time, which, as will be discussed later in the chapter, is the case for the linear solution after a sufficient amount of integration. Thus, once exponential growth dominates the perturbation field and the desired solution is approached, the effect of the filter diminishes to zero. (Actually, the quantity $Q_{j,k}$ is complex, but it is easily shown that application of the filter causes successive solutions to tend toward uniform spacing--arithmetically with respect to their phase angles and geometrically with respect to their amplitudes, which is the desired effect.)

3.5 Spatial Boundary Conditions

As was true for the axisymmetric model, the boundary values of the field variables in the linear model cannot be computed from the momentum and continuity equations and must be specified according to the physical boundary conditions imposed on the flow. For the most part, the boundary constraints applied to the axisymmetric flow are also appropriate for the perturbation fields but there are some differences, as will be seen below.

A. Inner Boundary

Although no variables at the inner boundary enter into the computations (except in the azimuthal frictional force, which is modified as in Chapter 2), they are assigned values in order to provide the correct graphic representation when they are plotted. This process is more complicated for the perturbation fields than for the

axisymmetric fields since it is wavenumber dependent and both the amplitude and phase angle of the complex variables must be considered. The amplitudes of all variables are set to zero on the center axis, except for U and V at wavenumber 1, where the amplitudes are assigned the values of the next outer points. The phase angles of all variables are chosen to be equal to those of the next outer points.

B. Lower Boundary

The conditions at the lower boundary are identical for both models; thus, we have $U_{i,1} = U_{i,2}$, $V_{i,1} = V_{i,2}$, $W_{i,1} = 0$ and $P_{i,1} = P_{i,2}$. The phase angle of $W_{i,1}$ is set equal to that of $W_{i,2}$ for graphic representation.

C. Outer Boundary

Recall from Section 2.5 that the axisymmetric model specified u , v and w at the inflow port whereas above, only u was specified (set to zero) while v and w satisfied the free-slip condition. The same procedure is used for the perturbation velocity fields. In this case, we require $U_{I-1,k} = V_{I,k} = W_{I,k} = 0$ for the inflow port so that no perturbation kinetic energy is advected into the domain. Above, we have $V_{I,k} = V_{I-1,k}(r_I/r_{I-1})$ and $W_{I,k} = W_{I-1,k}$. The phase angle of $U_{I-1,k}$ is set equal to that for $U_{I-2,k}$ for graphic representation.

D. Upper Boundary

As in the axisymmetric model, the conditions $W_{i,K} = W_{i,K-1}$ and $P_{i,K} = 0$ are applied at the upper boundary. Likewise, the advective extrapolation condition is used and its linearized form is

$$U_{i,K}^{n+1} = U_{i,K}^{n-1} \left(\frac{1-c}{1+c} \right) + U_{i,K-1}^n \left(\frac{2c}{1+c} \right) + (\bar{u}_{i,K-1} - \bar{u}_{i,K}) \left(\frac{2a}{1+c} \right) \text{ for } c \geq 0$$

$$U_{i,K}^{n+1} = 0 \text{ for } c < 0$$

$$V_{i,K}^{n+1} = V_{i,K}^{n-1} \left(\frac{1-d}{1+d} \right) + V_{i,K-1}^n \left(\frac{2d}{1+d} \right) + (\bar{v}_{i,K-1} - \bar{v}_{i,K}) \left(\frac{2b}{1+d} \right) \text{ for } d \geq 0$$

$$V_{i,K}^{n+1} = 0 \text{ for } d < 0$$

$$W_{i,K}^{n+1} = W_{i,K-1}^{n+1}$$

where

$$a = \frac{\Delta t}{2\Delta z} \left(W_{i,K-1}^n + W_{i+1,K-1}^n \right),$$

$$b = \frac{\Delta t}{\Delta z} W_{i,K-1}^n,$$

$$c = \frac{\Delta t}{2\Delta z} (\bar{w}_{i,K-1} + \bar{w}_{i+1,K-1}), \text{ and}$$

$$d = \frac{\Delta t}{\Delta z} \bar{w}_{i,K-1}.$$

Notice that $U_{i,K}$ and $V_{i,K}$ are set to zero whenever $\bar{w} < 0$, rather than when $\bar{w} + W < 0$. This follows from the assumption that $|W| \ll \bar{w}$.

3.6 Initialization and Development of Solution

The linear perturbation equations 3.10 - 3.13, along with the spatial boundary conditions, form a closed system of first order linear partial differential equations with constant coefficients. They are solved here by using the initial value technique (Brown, 1969). That

method requires the specifying of initial values for the field variables, and the model arbitrarily sets $U_{i,k} = V_{i,k} = W_{i,k} = 0.001$ for $1 < i < I$ and $1 < k < K$, and for the first two time levels. Notice that if all variables were initially zero, including the boundary values, they would remain identically zero for any number of integrations due to the nature of the equations.

For the first few hundred iterations of the model, the evolving solution becomes completely altered, under the influence of the boundary conditions and the axisymmetric flow, from its arbitrary initial state. Eventually, however, the solution begins to acquire a characteristic *structure*, defined as the mutual relationship between the amplitudes and phase angles of all variables of all fields. As the integration progresses, the structure changes ever more slowly and finally becomes essentially constant in time. This occurrence indicates that the most rapidly growing mode of the finite difference equations (or the least damped mode if none grow) has dominated the perturbation field and the desired solution has been computed (Brown, 1969).

Note that "constant structure" does not imply a constancy in the amplitude or phase of the entire perturbation as a whole but only in the relation among its components. In fact, the amplitude of the solution composed of a single mode varies exponentially with time while its phase angle changes at a constant rate. This can easily be seen by realizing that constancy of structure implies that the quotient between any two field variables is a (complex) constant in time.

It follows that for a single-mode solution, Eqs. 3.14 - 3.16 can all be reduced to the form $\frac{\partial}{\partial t} q_{i,k} = C q_{i,k}$ where C is a complex constant. This equation possesses the solution $q_{i,k} = Q_{i,k} e^{Ct} = Q_{i,k} e^{(C_r t)} e^{(i C_i t)}$ (the subscripts of C denoting the real and imaginary parts) which explicitly demonstrates the above properties. The quantity C_r is termed the growth rate of the perturbation and is inversely proportional to the e-folding time of the perturbation amplitude. The quantity C_i is the phase speed of the perturbation and is related to the angular velocity ω of the perturbation around the axis of the simulator by $\omega = C_i/m$ where m is the wavenumber. These two constants are important parameters for characterizing a perturbation solution.

3.7 Derivation of Energy Equations

While important characteristics of the linear perturbations are revealed through their growth rates, phase speeds and structures, the ways in which the perturbations extract energy from the axisymmetric flow can be determined from a perturbation energy budget equation. It is possible to derive an energy equation based on the "flux form" of the momentum equations (2.5 - 2.7) but a derivation using Eqs. 2.1 - 2.3 provides a simpler and more informative set of energy terms. In a procedure analogous to that followed in Section 3.1, the substitutions

$$u(r, \theta, z, t) = \bar{u}(r, z, t) + u'(r, \theta, z, t)$$

$$v(r, \theta, z, t) = \bar{v}(r, z, t) + v'(r, \theta, z, t)$$

$$w(r, \theta, z, t) = \bar{w}(r, z, t) + w'(r, \theta, z, t)$$

$$p(r, \theta, z, t) = \bar{p}(r, z, t) + p'(r, \theta, z, t)$$

are applied to Eqs. 2.1 - 2.3 and the zeroth and second order terms are omitted. This results in the linear equations

$$\begin{aligned} \frac{\partial u'}{\partial t} = & -\bar{u} \frac{\partial u'}{\partial r} - u' \frac{\partial \bar{u}}{\partial r} - \frac{\bar{v}}{r} \frac{\partial u'}{\partial \theta} - \bar{w} \frac{\partial u'}{\partial z} - w' \frac{\partial \bar{u}}{\partial z} \\ & - \frac{1}{\rho} \frac{\partial p'}{\partial r} + 2 \frac{\bar{v}v'}{r} + F_r' \end{aligned} \quad (3.22)$$

$$\begin{aligned} \frac{\partial v'}{\partial t} = & -\bar{u} \frac{\partial v'}{\partial r} - u' \frac{\partial \bar{v}}{\partial r} - \frac{\bar{v}}{r} \frac{\partial v'}{\partial \theta} - \bar{w} \frac{\partial v'}{\partial z} - w' \frac{\partial \bar{v}}{\partial z} \\ & - \frac{1}{r\rho} \frac{\partial p'}{\partial \theta} - \frac{\bar{u}v'}{r} - \frac{u'\bar{v}}{r} + F_\theta' \end{aligned} \quad (3.23)$$

$$\begin{aligned} \frac{\partial w'}{\partial t} = & -\bar{u} \frac{\partial w'}{\partial r} - u' \frac{\partial \bar{w}}{\partial r} - \frac{\bar{v}}{r} \frac{\partial w'}{\partial \theta} - \bar{w} \frac{\partial w'}{\partial z} - w' \frac{\partial \bar{w}}{\partial z} \\ & - \frac{1}{\rho} \frac{\partial p'}{\partial z} + F_z' \end{aligned} \quad (3.24)$$

The time derivative of perturbation kinetic energy is given by

$$\frac{\partial E'}{\partial t} = \frac{\partial}{\partial t} \left(\frac{1}{2} u'^2 + \frac{1}{2} v'^2 + \frac{1}{2} w'^2 \right) = u' \frac{\partial u'}{\partial t} + v' \frac{\partial v'}{\partial t} + w' \frac{\partial w'}{\partial t} \quad (3.25)$$

When the time derivatives on the right hand side of Eq. 3.25 are replaced by the right hand sides of Eqs. 3.22 - 3.24 and some of the terms are regrouped, the following energy equation results.

$$\frac{\partial E'}{\partial t} = - \frac{1}{2r} \frac{\partial}{\partial r} (\bar{u}u'u'r + \bar{u}v'v'r + \bar{u}w'w'r)$$

$$\begin{aligned}
& + \frac{1}{2r} \frac{\partial(\bar{u}r)}{\partial r} [u'u' + v'v' + w'w'] \\
& - \frac{1}{2r} \frac{\partial}{\partial \theta} (\bar{v}u'u' + \bar{v}v'v' + \bar{v}w'w') \\
& + \frac{1}{2r} \frac{\partial \bar{v}}{\partial \theta} [u'u' + v'v' + w'w'] \\
& - \frac{1}{2} \frac{\partial}{\partial z} (\bar{w}u'u' + \bar{w}v'v' + \bar{w}w'w') \\
& + \frac{1}{2} \frac{\partial \bar{w}}{\partial z} [u'u' + v'v' + w'w'] \\
& - u'u' \frac{\partial \bar{u}}{\partial r} - w'u' \frac{\partial \bar{u}}{\partial z} - u'v' \frac{\partial \bar{v}}{\partial r} - w'v' \frac{\partial \bar{v}}{\partial z} - u'w' \frac{\partial \bar{w}}{\partial r} \\
& - w'w' \frac{\partial \bar{w}}{\partial z} + \frac{u'v'\bar{v}}{r} - \frac{\bar{u}v'v'}{r} - \frac{1}{r\rho} \frac{\partial}{\partial r} (p'u'r) - \frac{1}{r\rho} \frac{\partial}{\partial \theta} (p'v') \\
& - \frac{1}{\rho} \frac{\partial}{\partial z} (p'w') + u'F_r' + v'F_\theta' + w'F_z' \\
& + p' \left[\frac{1}{\rho r} \frac{\partial}{\partial r} (u'r) + \frac{1}{r\rho} \frac{\partial v'}{\partial \theta} + \frac{1}{\rho} \frac{\partial w'}{\partial z} \right] \tag{3.26}
\end{aligned}$$

The terms which are singly underlined sum to zero according to the continuity equations 2.11 and 3.8 for the axisymmetric and perturbation flow components. To the remaining terms, we apply a volume integral over the entire domain in order to obtain the net energy contribution from each term. The doubly underlined terms integrate to zero given the above-mentioned boundary conditions while the triply underlined terms reduce to surface integrals. These simplifications result in the following volume-integrated perturbation kinetic energy equation.

$$\begin{aligned}
\frac{\partial}{\partial t} \iiint E' r \, dr \, d\theta \, dz = & \iiint \left[\left\{ u'v' \left(\frac{\bar{v}}{r} - \frac{\partial \bar{v}}{\partial r} \right) \right\}_1 \right. \\
& + \left\{ -u'w' \frac{\partial \bar{w}}{\partial r} \right\}_2 + \left\{ -u'u' \frac{\partial \bar{u}}{\partial r} - v'v'\bar{u} \right\}_3 \\
& + \left\{ -v'w' \frac{\partial \bar{v}}{\partial z} \right\}_4 + \left\{ -w'w' \frac{\partial \bar{w}}{\partial z} \right\}_5 \\
& + \left\{ -w'u' \frac{\partial \bar{u}}{\partial z} \right\}_6 \\
& + \left. \left\{ u'F_{r'} + v'F_{\theta'} + w'F_{z'} \right\}_8 \right] r \, dr \, d\theta \, dz \\
& + \iiint \left\{ \left[-\bar{w}E' \right]_{\text{TOP}} \right\}_7 r \, dr \, d\theta \\
& + \iiint \left\{ \left[-\frac{p'w'}{\rho} \right]_{\text{TOP}} \right\}_9 r \, dr \, d\theta \tag{3.27}
\end{aligned}$$

Braces numbered with subscripts have been used to divide the various terms of the energy equation into nine different groups. The physical meaning of each group and the importance of each in the growth of the perturbations will be discussed in Section 4.5.

3.8 Linear Model Testing and Verification

To the author's knowledge, the stability of an axisymmetric cylindrical flow having both axial and radial variations, as well as nonzero radial motion, has never been tested and no results are available against which the linear model could be directly compared. In

searching for possible errors in the formulation of the equations or in the computer coding, the only methods which encompassed the entire model involved self-checking procedures. One method was by making a slow and careful comparison with the axisymmetric model, to which the linear model bears a strong resemblance. Another test involved comparing the tendency of the volume-integrated perturbation kinetic energy, computed from the finite difference version of Eq. 3.27, with the energy tendency computed directly from the perturbation velocity fields. This is a valuable technique because it helps to verify both formulations.

Some additional methods were devised to help insure the reliability of certain portions of the model. One such method was simply to verify that the divergence of the velocity field was maintained at zero as required by Eq. 3.17. Two other tests involved making comparisons with established stability properties of somewhat simplified vortex flows. The first test reproduced some results by Staley and Gall (1979) in which azimuthal wind profiles obtained from Hoecker's (1960) Dallas tornado measurements were tested for instability. Even though their model used the eigenvalue method of solution and the equations were formulated in terms of the stream function, excellent agreement was obtained. It should be mentioned that, for this particular test, the linear model had to be modified slightly in order to constrain the perturbation fields to be axially constant. The second test obtained stability measurements and linear perturbation structures for the flow investigated by Maslowe (1974) as described in Section 1.3.

Once again, the linear model required some modification in order that an axial wavenumber could be specified. This experiment was also performed independently by Staley and Gall (unpublished) with their eigenvalue model and very close agreement was found between all three models.

Chapter 4

EXPERIMENTS AND RESULTS

This chapter describes the particular numerical experiments which were selected to conduct the stability analysis, and discusses in detail the pertinent experimental results. A discussion and analysis of these results and their relevance to laboratory observations will be given in Chapter 5. Following the convention used in Chapter 3, axisymmetric field variables are denoted by overbars while perturbation variables contain prime symbols. Unless otherwise specified, all numerical quantities are based on the MKS (Meter, Kilogram, Second) system of units.

4.1 Specifications of Numerical Experiments

A. Linear Dimensions

As mentioned in Section 2.7, the axisymmetric model was tested against Rotunno's model by using the same geometric dimensions and boundary conditions, and comparing the results. Those particular dimensions, which correspond to Ward's simulator rather than the Purdue simulator, have been retained for all experiments in the present study. Thus, the vertical and radial extents of the computational domain are 1.2192 m and 0.6096 m, respectively, and the inflow region comprises the lowest fourth of the outer boundary. With 30 grid intervals spanning the distance from the center axis to the outer

boundary, and 60 intervals from the lower surface to the baffle, the radial and vertical grid spacings are equal and have a value of 0.0203 m.

B. Eddy Viscosity Coefficient

A few experiments were run using an eddy viscosity coefficient of $\nu = 0.000186 \text{ m}^2\text{s}^{-1}$, the value most often used by Rotunno (1977). However, a somewhat higher value was needed in the linear model to provide reasonably smooth perturbation fields. Rotunno chose the above figure as the lowest value for which his axisymmetric model would give smooth solutions but what value actually gives the best representation of the flow in the simulator is not known. One method for obtaining a crude estimate of the eddy viscosity coefficient is to invoke mixing length theory (Holton, 1972) which relates the viscosity coefficient to the shear σ of the mean (i.e., averaged over unresolved turbulent fluctuations) wind and the characteristic linear dimension L of the turbulent eddies according to the formula

$$\nu = L^2 |\sigma|$$

Simulator flow measurements (e.g., Church et al., 1979) indicate that wind shears of at least 2 s^{-1} occur over large regions of the vortex while visual inspection of smoke injected into the flow at higher swirl ratios reveals turbulent fluctuations on the scale of, perhaps, a few centimeters. This implies that the eddy viscosity coefficient may reach $0.01 \text{ m}^2\text{s}^{-1}$ in some regions. On the other hand, where laminar flow predominates, such as at low swirl ratios, values not too

different from the molecular viscosity coefficient of $0.000015 \text{ m}^2\text{s}^{-1}$ may be appropriate. Based on this possible range, an intermediate value of $\nu = 0.001 \text{ m}^2\text{s}^{-1}$ was chosen for the majority of experiments.

C. Density

The value used for the density has no bearing on the fluid motion since the flow is incompressible. Density in this case merely acts as a scaling factor for determining the absolute (but not relative) magnitude of the spatial pressure variations. That is, the quotient p/ρ , rather than p , is the fundamental quantity which is uniquely determined for a given flow. In order to make the two quantities equal, all experiments use $\rho = 1.0 \text{ kg}\cdot\text{m}^{-3}$ which is, incidentally, approximately its true value.

D. Swirl Ratio

The range of swirl ratio explored in this study is from 0.0 to 3.0. This includes the extent of expected atmospheric values (Church et al., 1979) and covers the limits of available data for the simulators. Recall that the swirl ratio is given by $S = r_0 \Gamma / 2Qh$ where r_0 is the radius of the updraft hole, Γ is $1/2\pi$ times the circulation at r_0 , Q is $1/2\pi h$ times the volumetric flow rate through the simulator, and h is the height of the inflow region. Denoting the inward radial velocity and the azimuthal velocity at r_0 by $-\bar{u}_0$ and \bar{v}_0 , respectively, we can write $Q = -r_0 \bar{u}_0$ and $\Gamma = \bar{v}_0 r_0$. From these relations it follows that $S = -\bar{v}_0 r_0 / 2\bar{u}_0 h$. Since in all experiments, $r_0 = 2h$, the swirl

ratio is given by the ratio of \bar{v}_0 to $-\bar{u}_0$. Following Rotunno's simulations, all numerical experiments in this study use $\bar{u}_0 = -0.3048 \text{ ms}^{-1}$.

E. Linear Wavenumber

Wavenumbers from 1 up to a maximum of 6 were tested for instability in the linear model. This is the range of the number of secondary vortices which has been obtainable in the laboratory simulators. For a given swirl ratio, the selection of linear wavenumbers to be tested was guided in part by the observed linear growth rate spectrum: Sufficiently high wavenumbers were tested to establish the wavenumber of maximum growth rate but not the wavenumber where zero growth begins.

F. List of Axisymmetric and Linear Experiments

In accordance with the findings of the laboratory vortex simulations, the numerical experiments were chosen to emphasize the dependency of the linear waves on the swirl ratio rather than on other experimental parameters. The axisymmetric and linear experiments which comprise that part of the study are listed in the upper portion of Table 4.1. Entries in the first column are arbitrarily-designated axisymmetric experiment numbers while those in the last six columns are linear experiment numbers. The absence of an entry indicates that the particular linear experiment was not performed. It is important to note that all linear experiments use the same eddy viscosity coefficient as the axisymmetric experiment to which they correspond.

Table 4.1. List of Numerical Experiments

Axisymmetric Experiment Number	Swirl Ratio	Eddy Viscosity Coefficient	Linear Experiment Number					
			m=1	m=2	m=3	m=4	m=5	m=6
1	0.1	0.001	1	2				
2	0.3	0.001	<u>3</u>	4				
3	0.5	0.001	<u>5</u>	<u>6</u>	7			
4	0.7	0.001	8	9	10	11		
5	1.0	0.001	12	<u>13</u>	14	15	<u>16</u>	
6	1.5	0.001	17	18	19	20	21	
7	2.0	0.001	22	23	24	<u>25</u>	26	
8	2.5	0.001	27	28	29	30	31	32
9	3.0	0.001	33	<u>34</u>	35	36	<u>37</u>	38
10	1.0	0.000186	39	40	41	42	43	

The lower portion of Table 4.1 contains additional experiments which were run with the lower value for the viscosity coefficient.

4.2 Axisymmetric Model Solutions

Six of the axisymmetric experiments listed in the upper part of Table 4.1 have been selected for displaying the characteristics of the vortex over the investigated range of swirl ratio. In Figs. 4.1 - 4.12, various components of the steady state solutions for these experiments are plotted. All contour plots are radial-vertical cross sections with the vertical line on the left side denoting the center axis of the simulator. The lower surface of the simulator, the inflow and outflow ports, and the fictitious outer computational boundary are also shown. Below each plot is given the swirl ratio and a quantity called Δ denoting the contour interval. Negative-valued contour lines are represented by a broken pattern while the zero- and positive-valued lines are solid.

Figs. 4.1 and 4.2 contain plots of the stream function which is defined by $\frac{\partial \bar{\psi}}{\partial r} = -\bar{w}r$ and $\frac{\partial \bar{\psi}}{\partial z} = \bar{u}r$ with $\bar{\psi}$ set to zero at the lower right corner. Thus, the streamfunction contours are everywhere parallel to the flow and contain equal volume flow rates between them. For the case $S = 0.1$, outflow occurs over all the upper boundary as indicated by the stream field. For larger values of S , however, a central region of $\bar{\psi} > 0$ develops implying that air within the region has entered through the baffle at the top rather than from the normal inflow region. As mentioned in Chapter 1, this occurrence is a regular

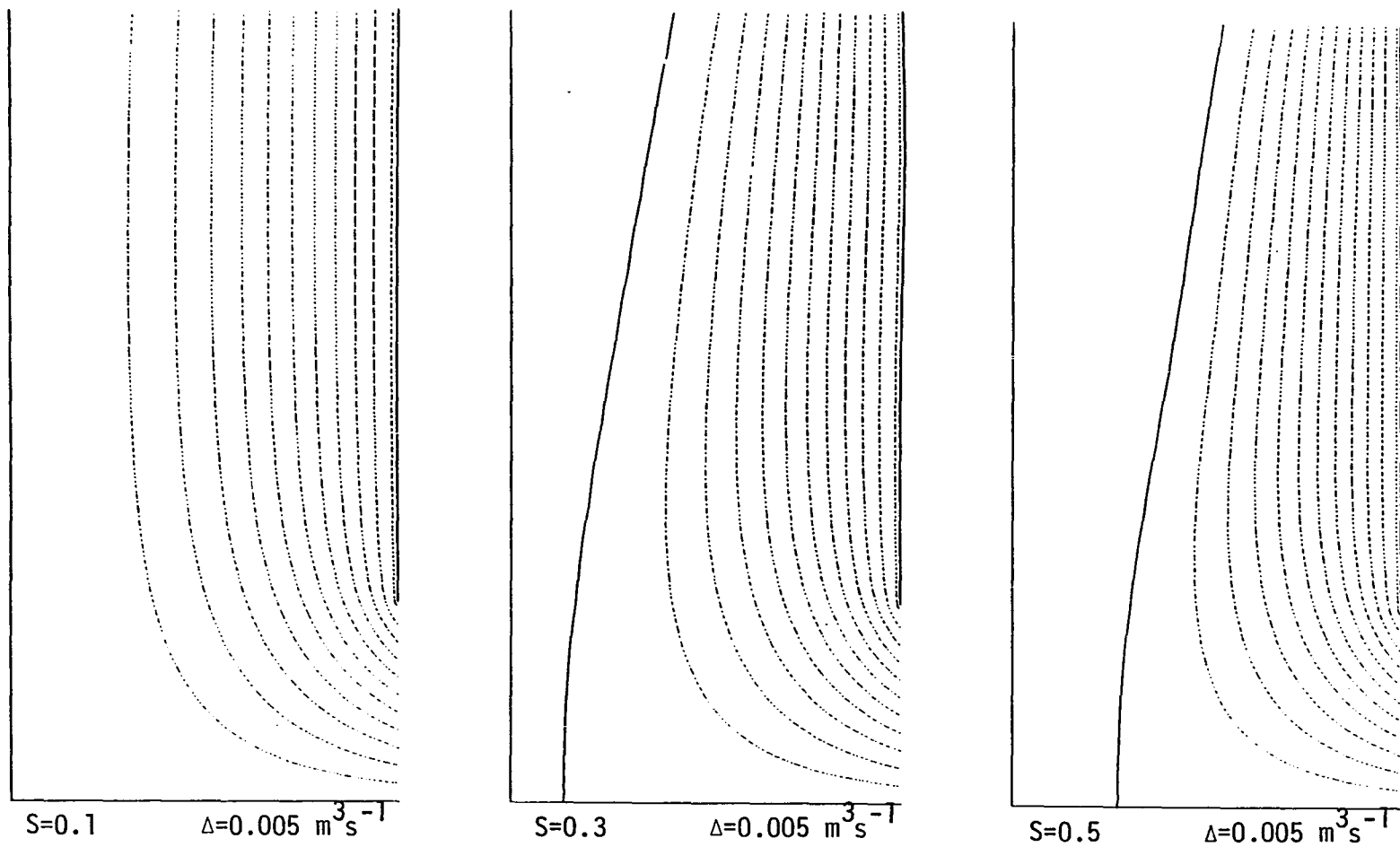


Figure 4.1. Radial-height cross sections of numerically-generated stream function fields. The swirl ratio is denoted by S while the contour interval is indicated by Δ . Negative-valued contours are represented by a broken pattern while the zero and positive contours are solid lines.

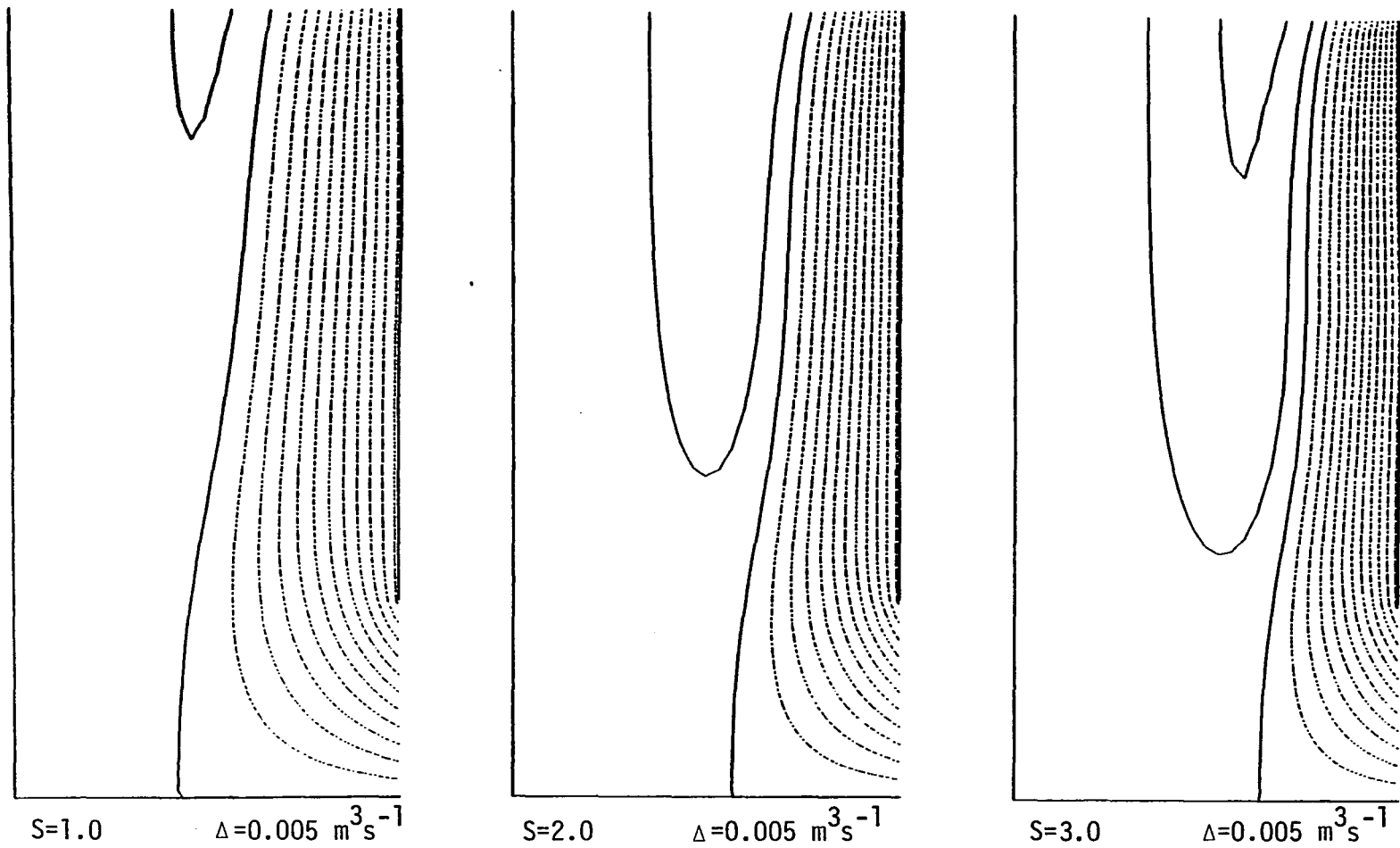


Figure 4.2. Same as in Figure 4.1 but for higher swirl cases.

feature of high swirl flow in the laboratory simulator. The $\bar{\psi} = 0$ contour separating the two regions can be seen to increase its radial position both with height and with swirl ratio.

The radial velocity plots shown in Figs. 4.3 and 4.4 indicate that significant radial motion occurs only near the inflow region with the strongest flow at the inflow boundary itself. In accordance with Figs. 4.1 and 4.2, the inward flow becomes confined within the increasingly narrow ring as S increases. The moderate outward radial flow which develops at the top for high swirl ratios is associated with the baffle's destruction of the radial pressure gradient and, consequently, of the approximate cyclostrophic balance.

From Figs. 4.5 and 4.6, it is apparent that the azimuthal velocity fields contain a strong radial dependence with maximum values occurring along a line which lies at a radius increasing with both height and swirl ratio. Close inspection reveals that relation $\bar{v}r = \text{constant}$, implying constant angular momentum, holds fairly closely outside the maximum, while inside the maximum, \bar{v} falls quickly to nearly zero. For $S = 0.1$, this latter transition occurs near the center of the chamber and thus indicates approximate solid-body rotation. For higher swirl ratios, however, the inner shear region lies at greater radii and consequently involves a high rate of fluid deformation. As will be seen later, this deformation is an important contributor to the instability of the vortex. A comparison of these plots with their counterparts in Figs. 4.1 and 4.2 shows that, except for the case $S = 0.1$ where no downdraft occurs, the curve $\bar{\psi} = 0$ consistently lies near

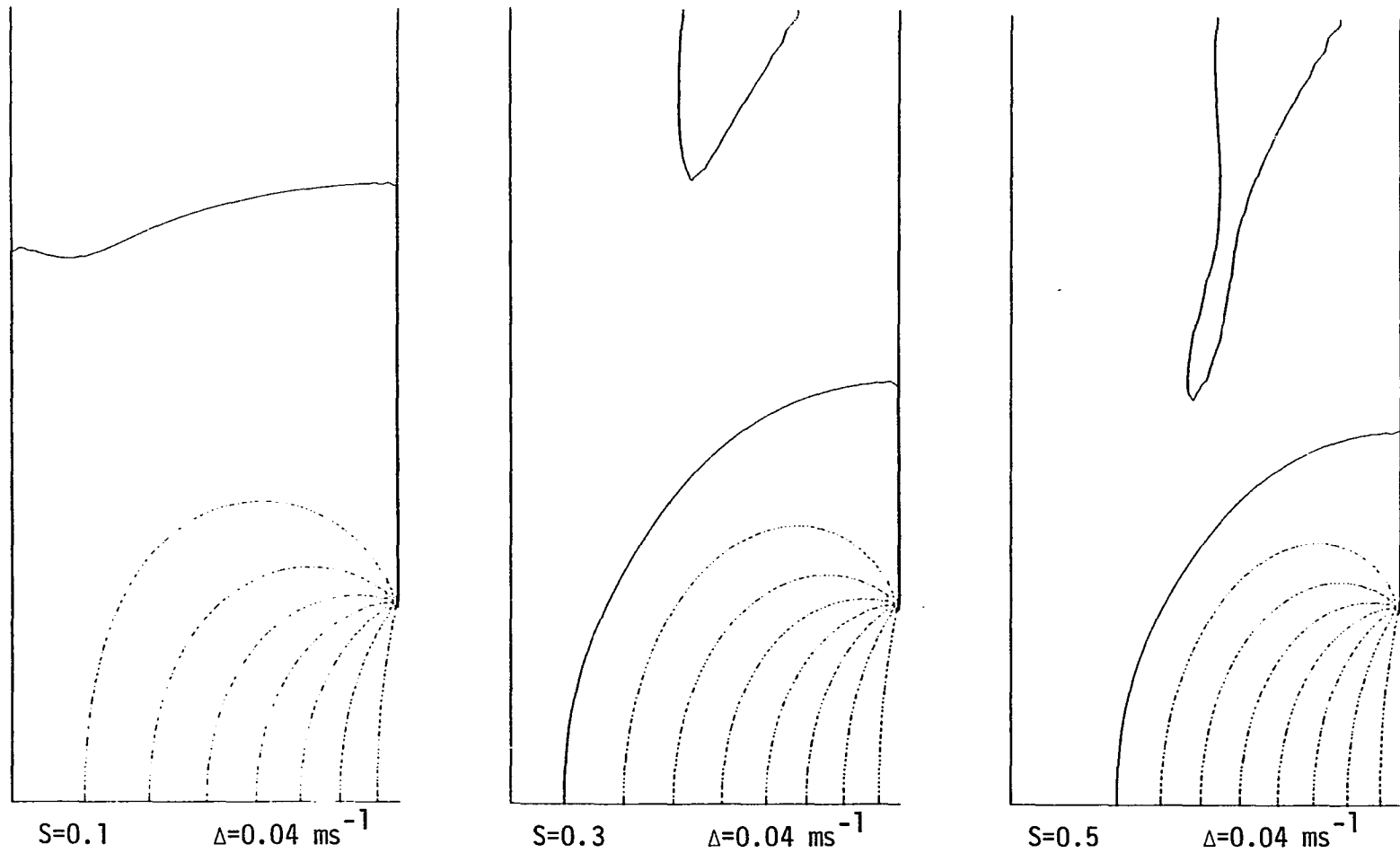


Figure 4.3. Same as in Figure 4.1 but for radial velocity.

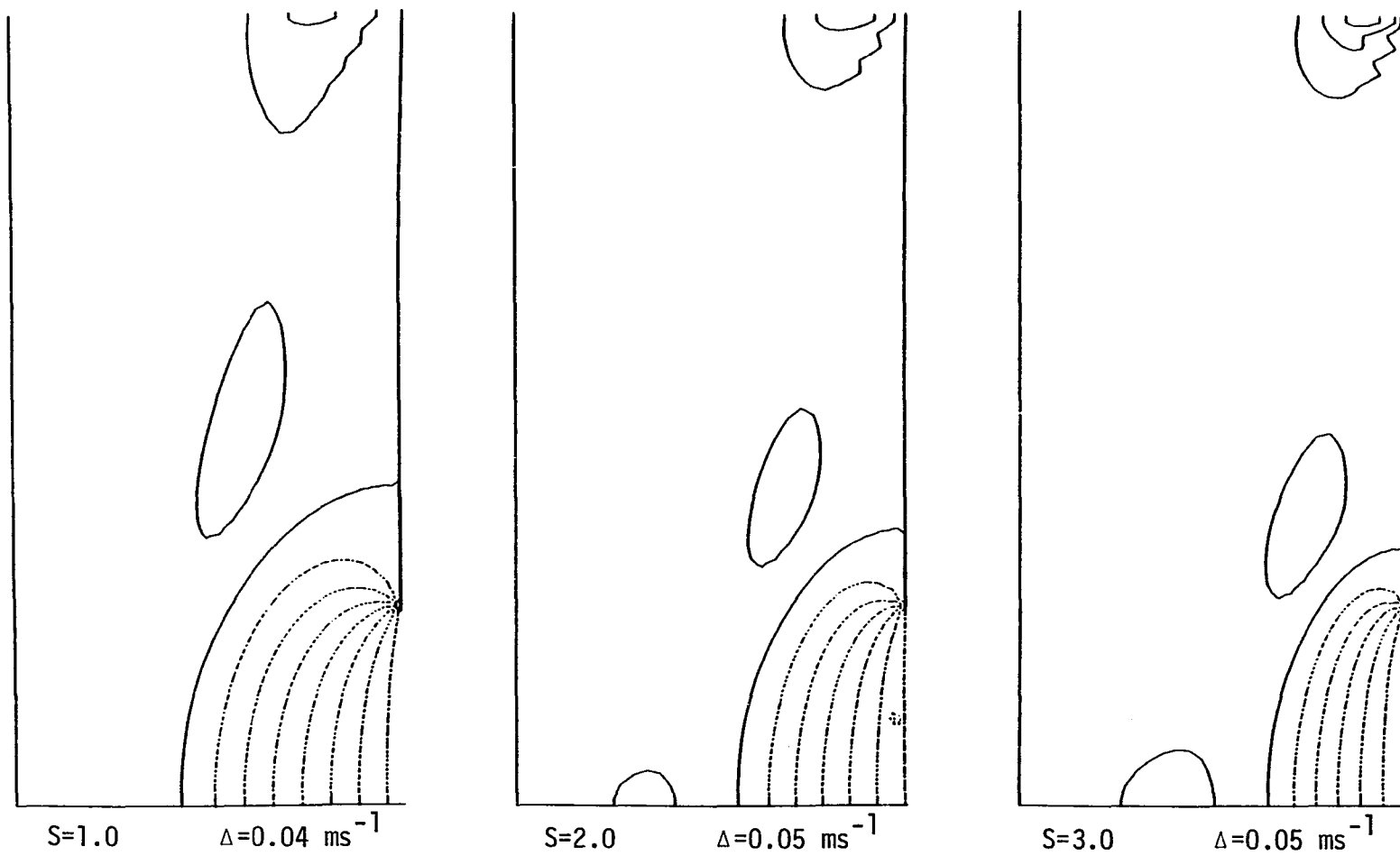


Figure 4.4. Same as in Figure 4.1 but for radial velocity and higher swirl cases.

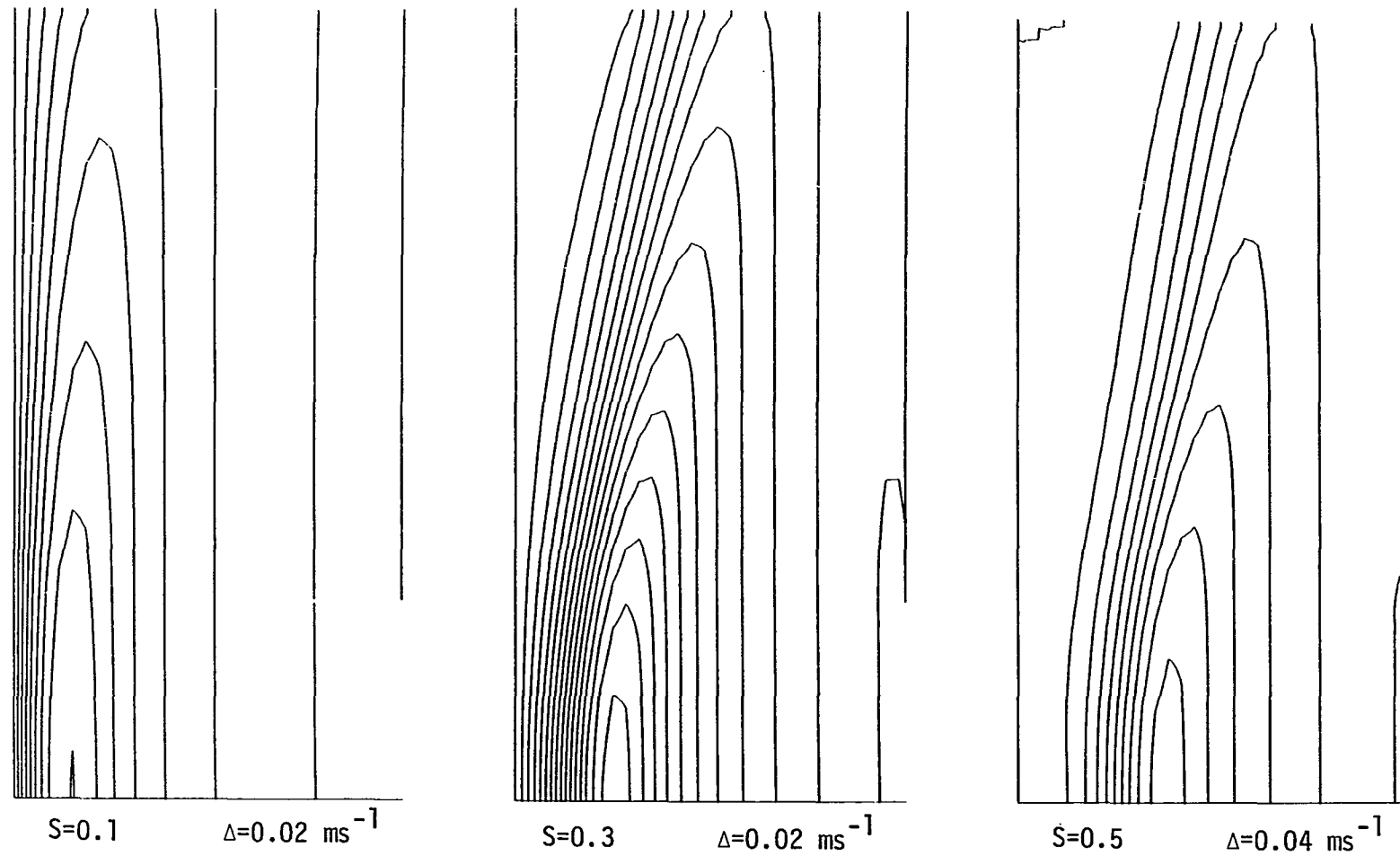


Figure 4.5. Same as in Figure 4.1 but for azimuthal velocity.

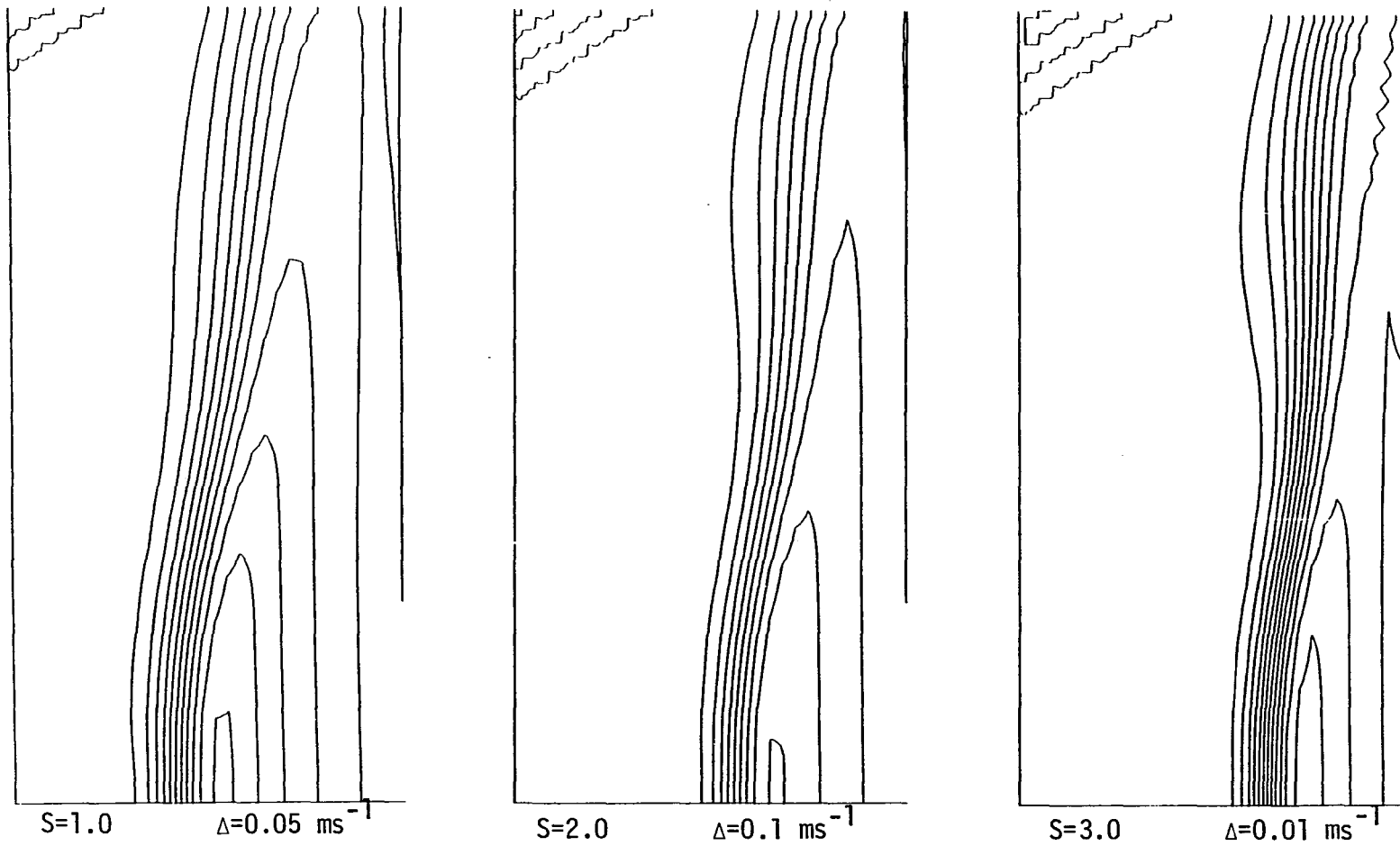


Figure 4.6. Same as in Figure 4.1 but for azimuthal velocity and higher swirl cases.

the center of the inner shear zone. This is a consequence of the fact that air entering through the baffle contains no swirl and thus large azimuthal stresses occur across the $\bar{\psi} = 0$ boundary.

The vertical velocity fields, shown in Figs. 4.7 and 4.8, can be seen to be strongly affected by the swirl ratio. For $S = 0.1$, \bar{w} is everywhere positive and rather weakly dependent on radius while, at $S = 0.3$, a central downdraft has appeared giving rise to a strong radial shear of the vertical wind. As S is further increased, the shear zone moves outward, and the downdraft occupies a greater volume while the updraft becomes more confined. Because the inflow is constrained to occur at a constant rate, the confinement of the updraft results in significant increases in the maximum upward velocity (which always occurs along the outer radial boundary) and, consequently, in the strength of the shear. For the cases where it is present, the zone of large $\partial\bar{w}/\partial r$ approximately coincides with the zone of large $\partial\bar{v}/\partial r$.

The vertical vorticity and its dependence on S are shown in Figs. 4.9 and 4.10. For $S = 0.1$, the maximum $\bar{\zeta}$ occurs along the center axis, while for higher S , the maximum moves outward. The initial departure of the maximum from the center is accompanied by a decrease in the magnitude of the maximum vorticity; otherwise, the magnitude increases with S . The region over which significant vorticity occurs is relatively narrow, leaving rather large areas of near zero values. An important point to notice is that negative values of vorticity do not occur in the axisymmetric vortex.

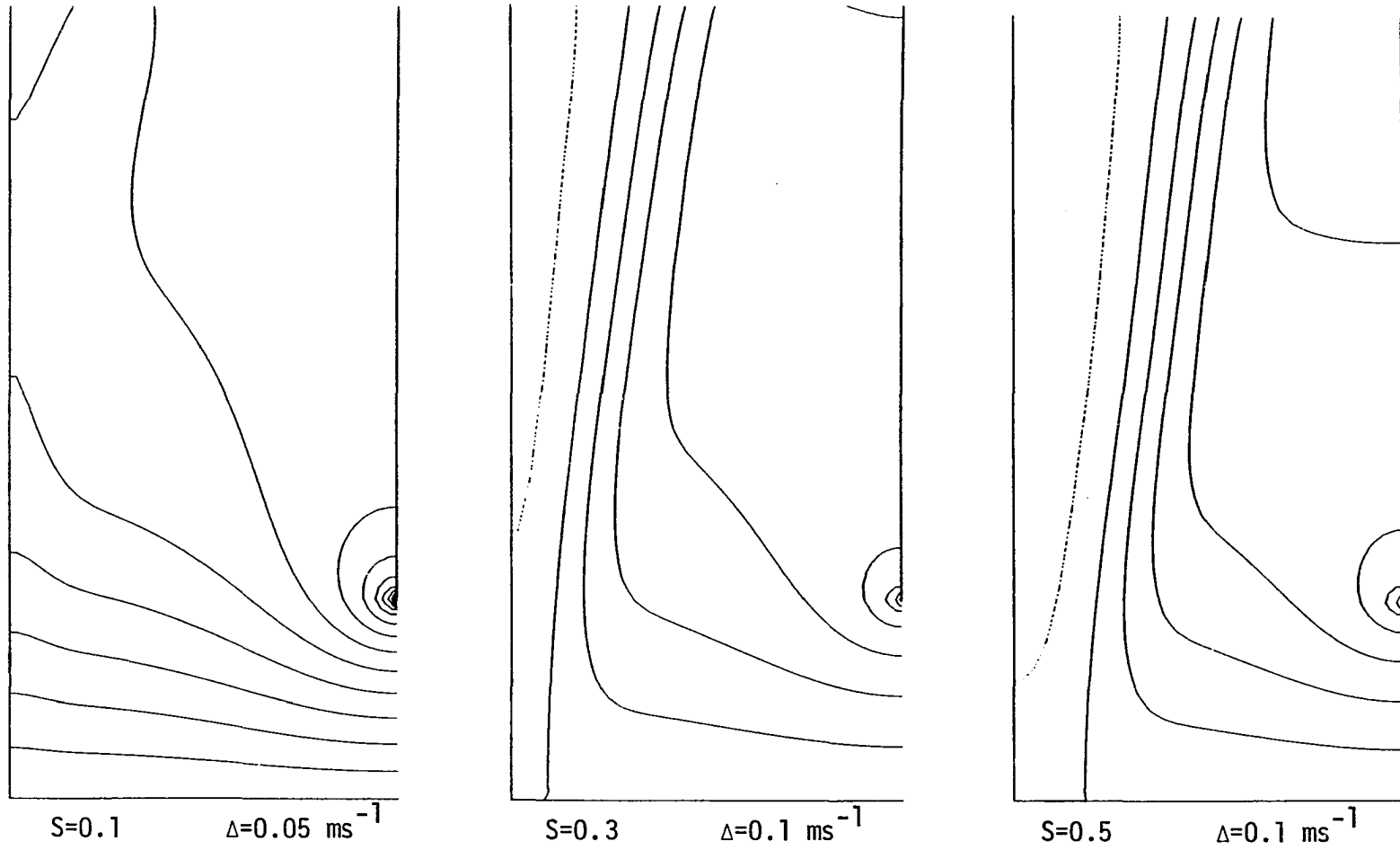


Figure 4.7. Same as in Figure 4.1 but for vertical velocity.

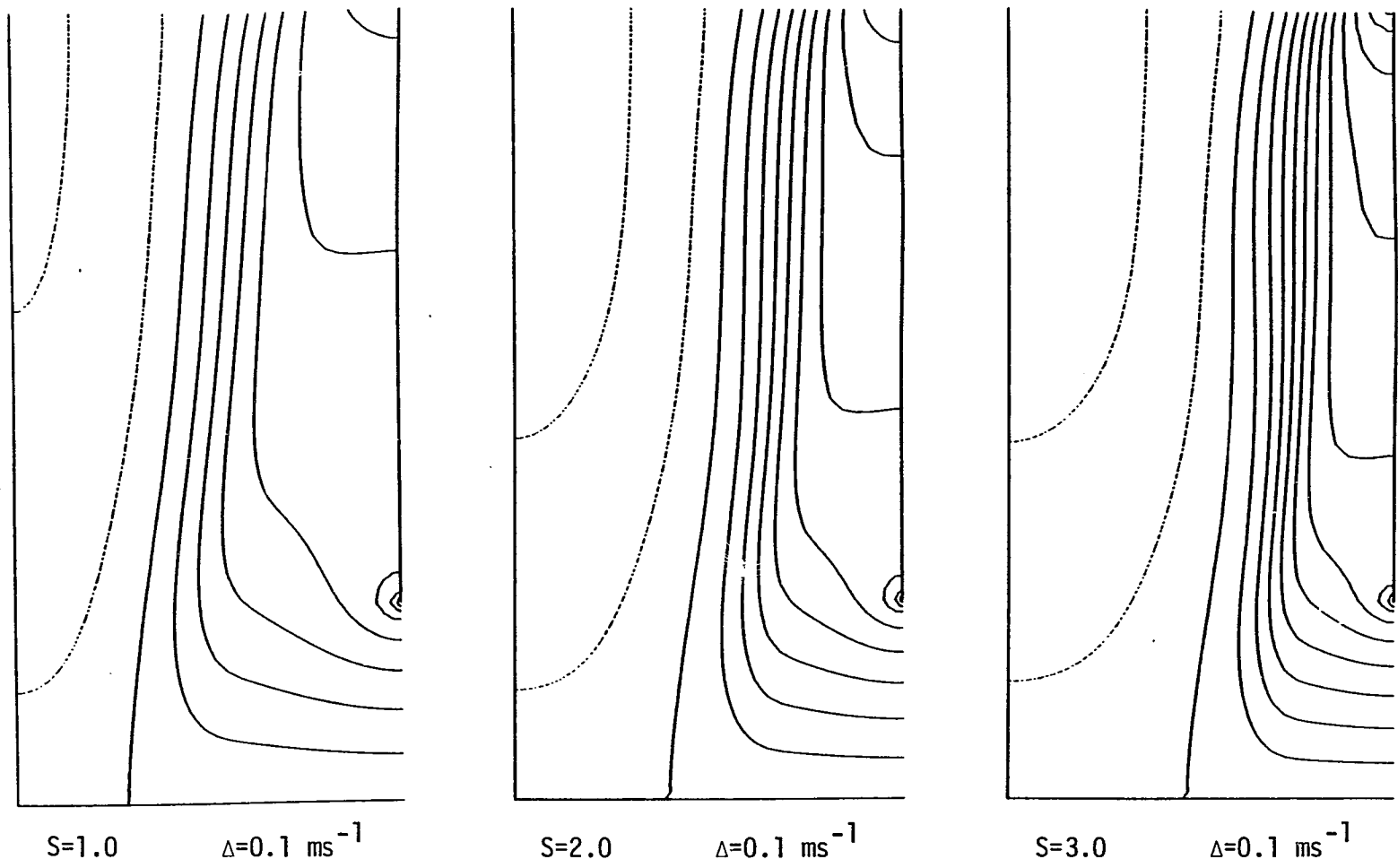


Figure 4.8. Same as in Figure 4.1 but for vertical velocity and higher swirl cases.

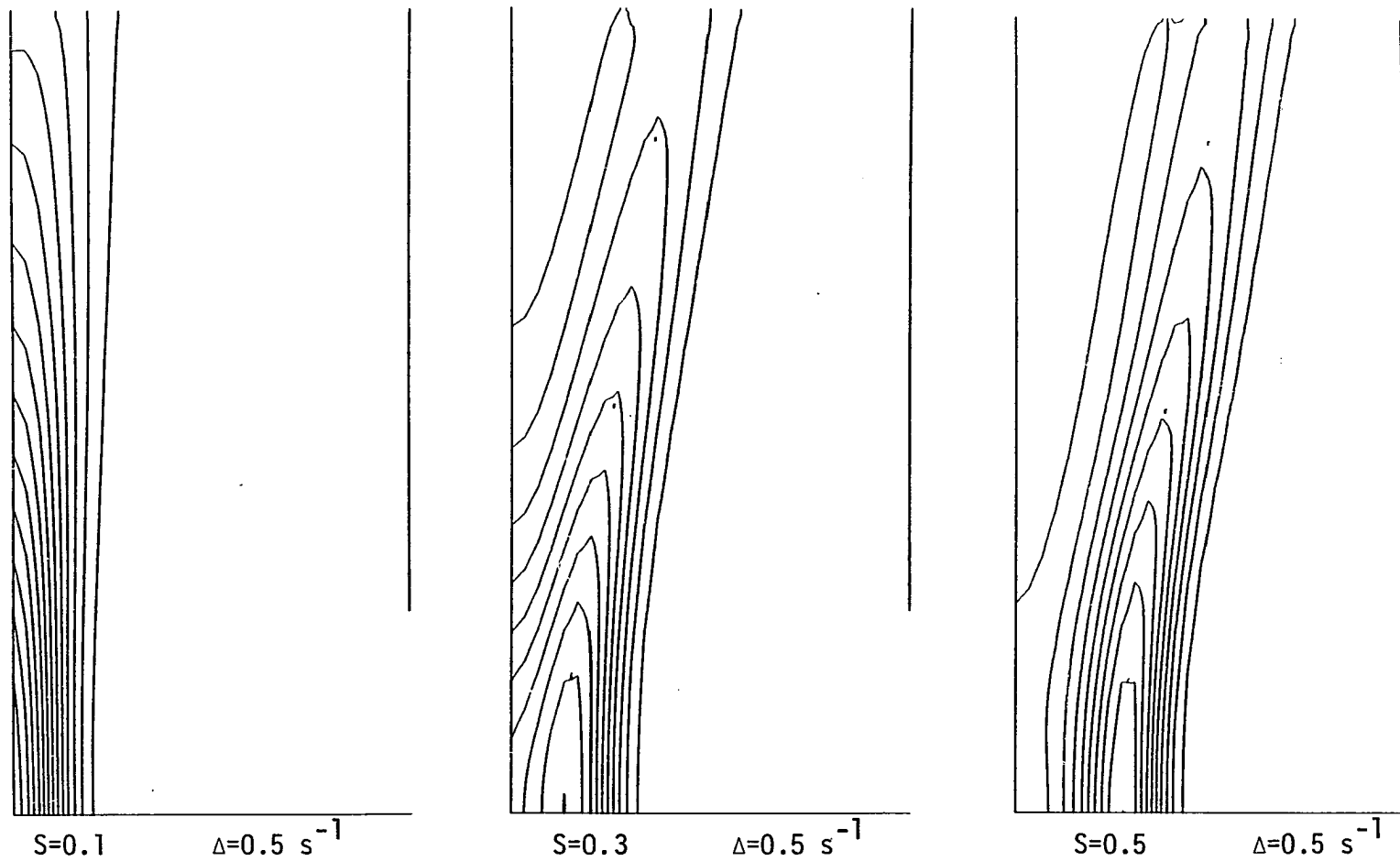


Figure 4.9. Same as in Figure 4.1 but for vertical vorticity.

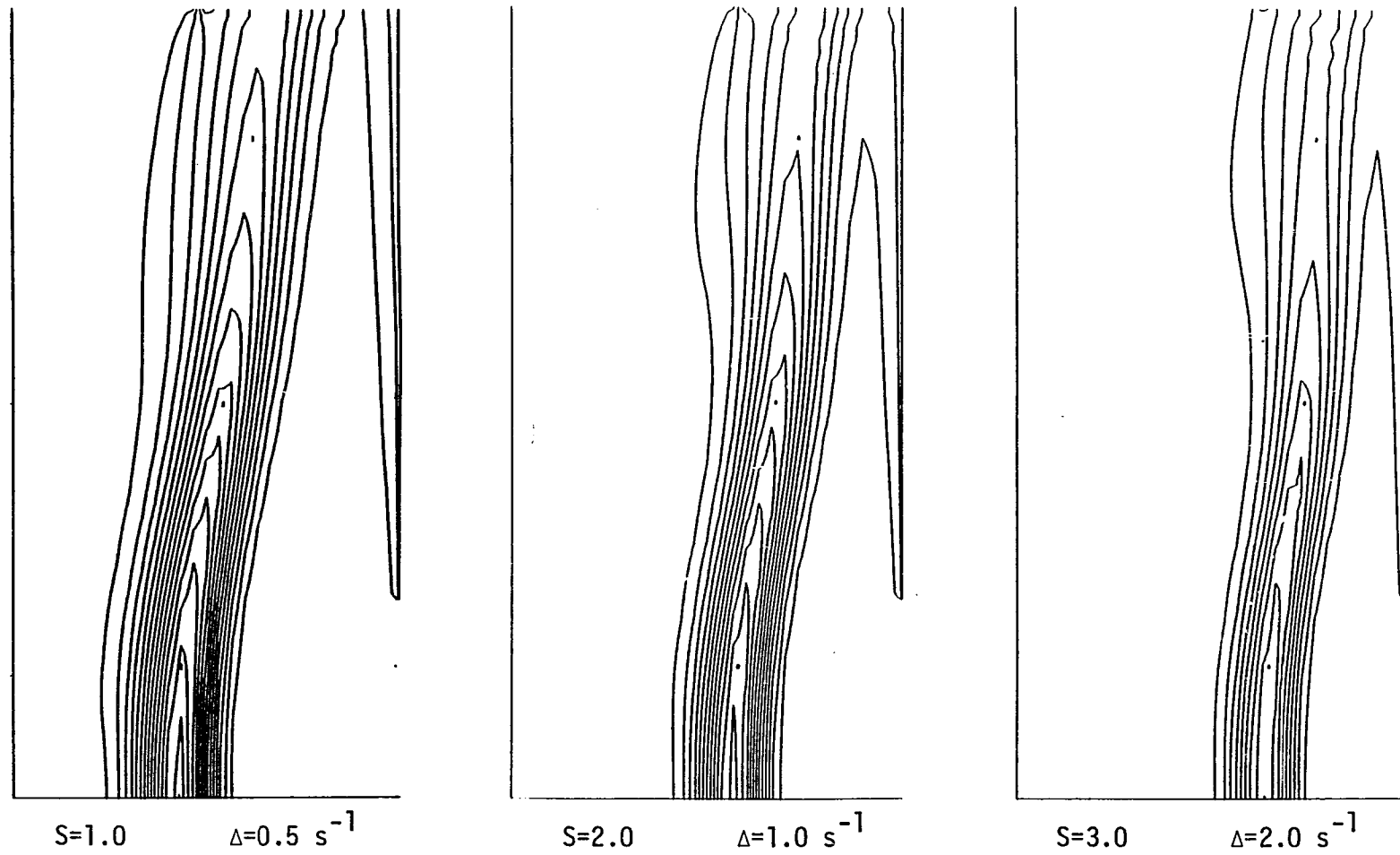


Figure 4.10. Same as in Figure 4.1 but for vertical vorticity and higher swirl cases.

Figs. 4.11 and 4.12 contain plots of the azimuthal component of vorticity. The primary contributor to this quantity is the radial shear of the vertical wind since \bar{u} is near zero where significant vorticity occurs. In keeping with the behavior of \bar{w} , the region of strong vorticity moves outward with increasing S . As suggested in Chapter 1, and as will be demonstrated in subsequent sections, the presence of significant shear of \bar{w} in the axisymmetric vortex has a major influence in its instability on the structure of the unstable waves.

In order to obtain some estimate of the effect which the eddy viscosity coefficient has on the vortex, a few experiments were run using the lower value of $\nu = 0.000186$. The axisymmetric fields of \bar{v} , \bar{w} , $\bar{\zeta}$, and $\bar{\eta}$ for the case $S = 1.0$ are shown in Fig. 4.13. A comparison of these with the corresponding case in previous figures shows that while the decrease in ν has only a small effect on the maximum strengths and positions of \bar{v} and \bar{w} , it greatly decreases the width of their shear zones. This, in turn, concentrates the vorticity leading to significantly higher maximum values of $\bar{\zeta}$ and $\bar{\eta}$.

4.3 Growth Rates of Linear Perturbations

Recall from Section 3.6 that for a particular axisymmetric flow, the linear model is integrated forward in time until the perturbation field is dominated by the most rapidly growing mode having the specified azimuthal wavenumber, and the perturbation amplitude increases exponentially with time. If the amplitude is thus written as $A = A_0 e^{Gt}$, then G symbolizes what is defined as the growth rate.

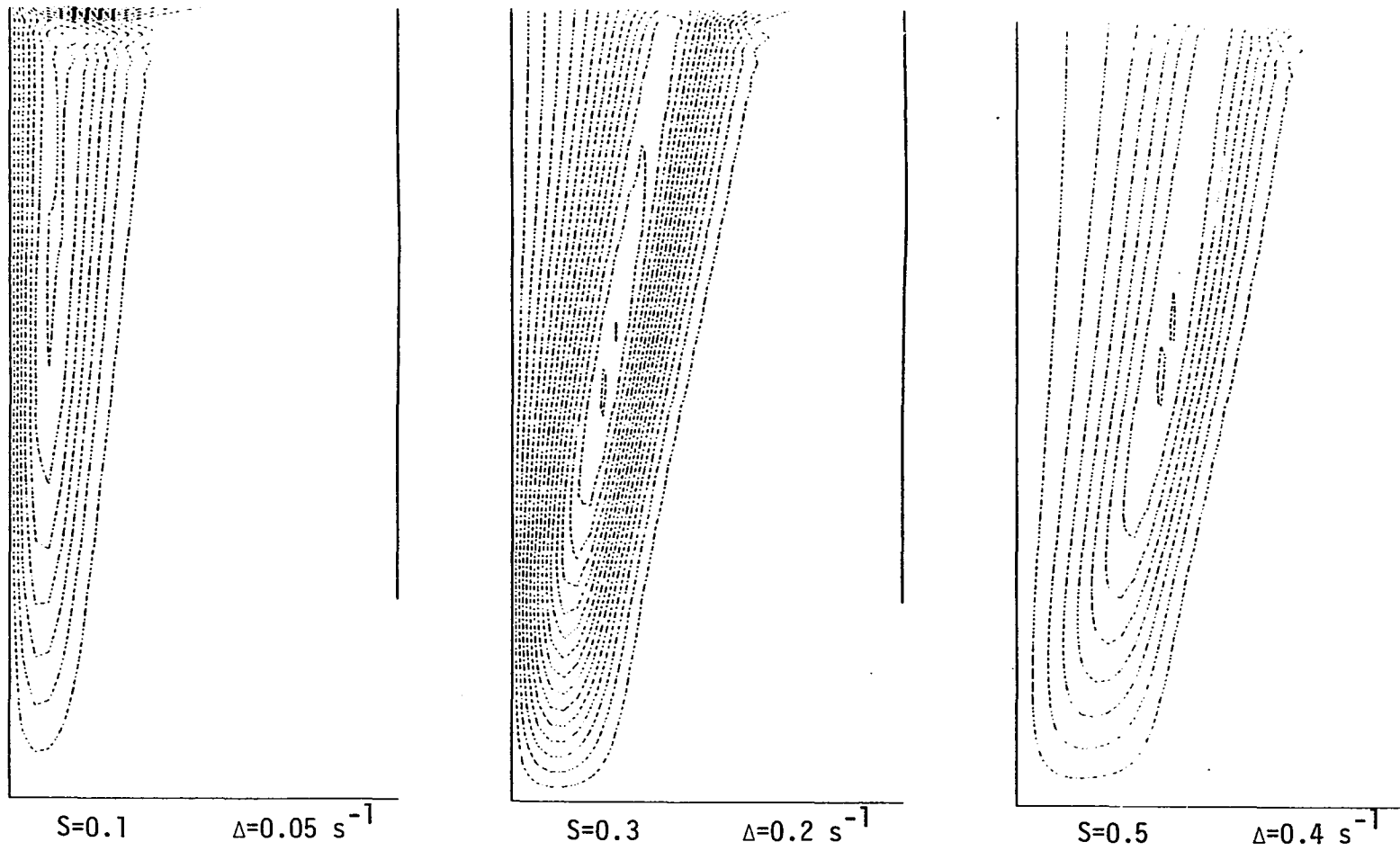


Figure 4.11. Same as in Figure 4.1 but for azimuthal vorticity.

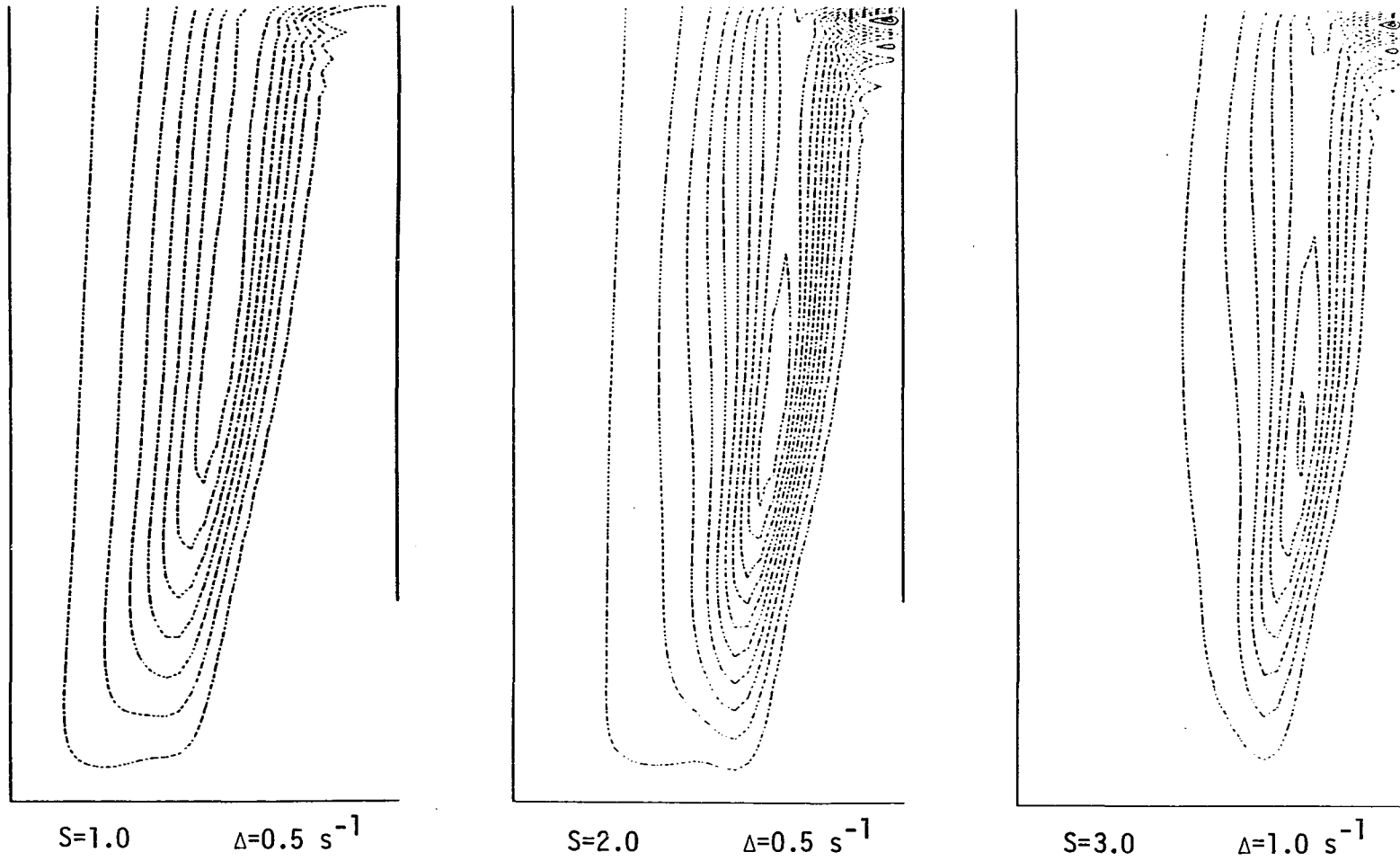


Figure 4.12. Same as in Figure 4.1 but for azimuthal vorticity and higher swirl cases.

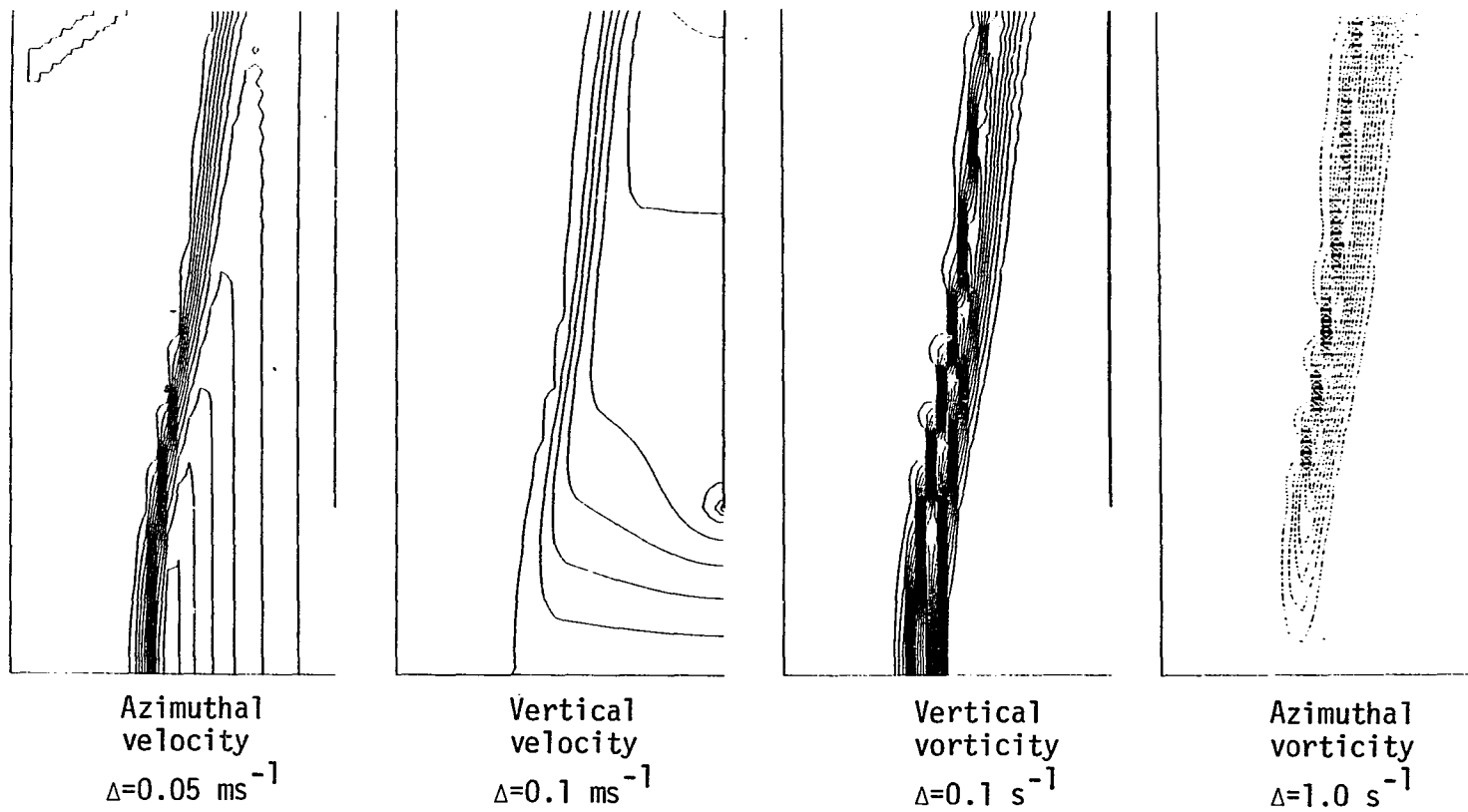


Figure 4.13. Radial-height cross sections of various numerically generated fields for the case $S=1.0$ and $\nu=0.000186$. Contour scheme is as in Figure 4.1.

G has the dimension of t^{-1} and is the reciprocal of the e-folding time of the amplitude.

A contour plot of the linear growth rate as a function of swirl ratio and azimuthal wavenumber for axisymmetric experiments 1-9 is shown by the curves in Fig. 4.14. Over the given domain, G ranges from 0 to near 2 indicating a variation from stable conditions to unstable flow in which large amplitude perturbations can appear in only a few seconds. The critical curve separating stable from unstable conditions appears as a nearly straight line passing just above $S=0.1$ for wavenumber 1 and just below $S = 1.0$ for wavenumber 5. Thus, as S increases from zero, the longer waves become unstable before the shorter waves. All wavenumbers are stable for $S \leq 0.1$. The growth rate of wavenumber 1 increases with S to a maximum value of around 0.35 at $S = 0.3$ to 0.5, and then decreases monotonically for higher S . For all other wavenumbers, the growth rate increases monotonically with S over the domain investigated. For the most part, the higher the wavenumber, the higher is the rate of increase of growth rate with S , once S is high enough for amplification of a particular wavenumber to take place. This behavior results in an overall shift in the most unstable wavenumber from low to high values as S increases. At and below $S = 0.6$, wavenumber 1 has the highest growth rate. Beginning around $S = 0.7$, wavenumber 2 becomes the most unstable and continues until about $S = 1.0$ when wavenumber 3 takes over. Wavenumber 4 is the most unstable from around $S = 1.5$ to $S = 2.5$ and wavenumber 5 dominates above there.

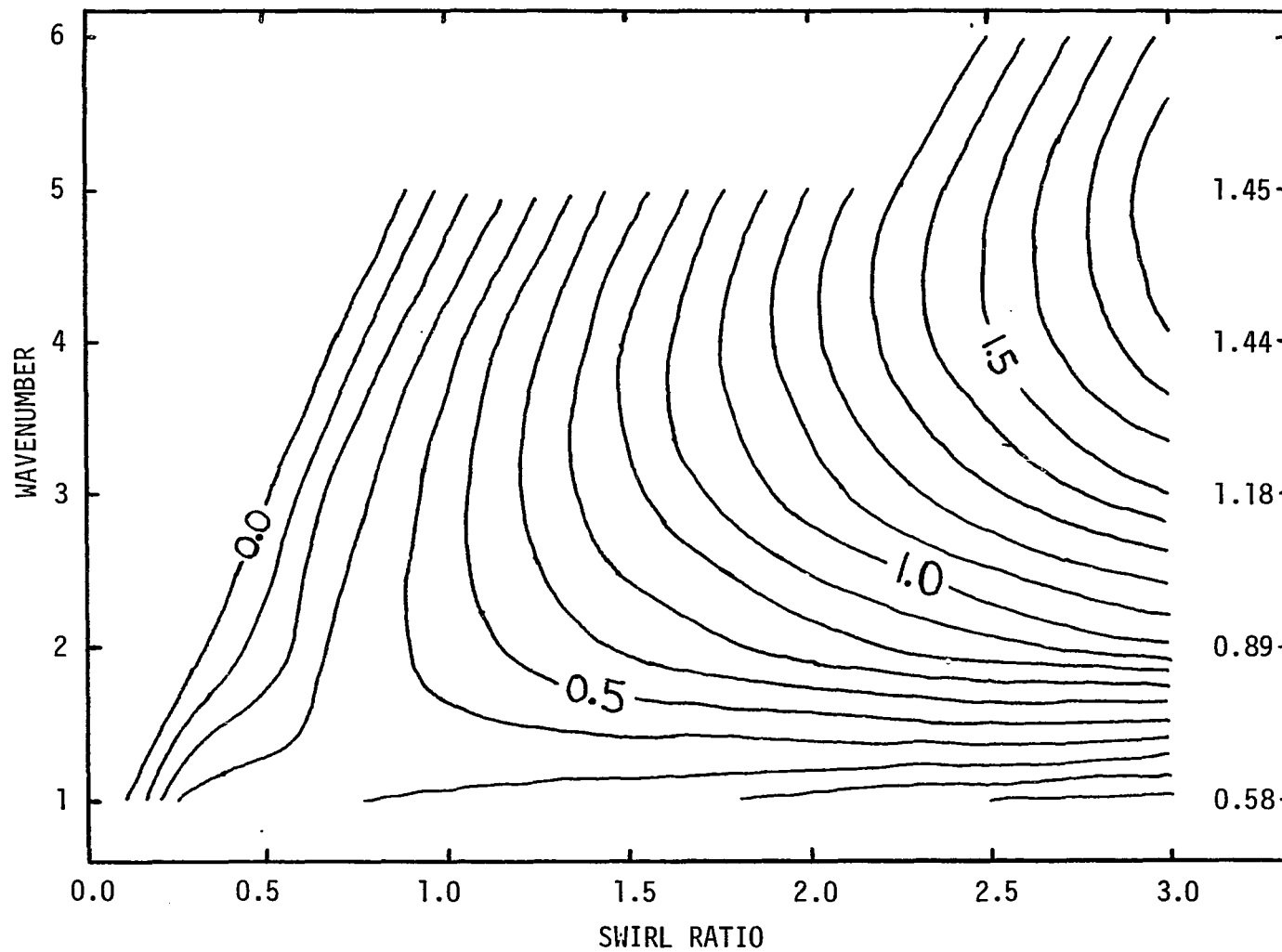


Figure 4.14. Growth rates of linear perturbations in s^{-1} as a function of swirl ratio and wavenumber. The contours represent cases with $\nu=0.001$ and the numbers to the right of the plot are growth rates for the case $\nu=0.000186$ and $S=1.0$.

The numbers listed to the right of the contour field in Fig. 4.14 represent linear growth rates for wavenumbers 1-5 and $S = 1.0$ obtained by using an eddy viscosity coefficient of $\nu = 0.000186$. The reduction in viscosity causes a significant increase in the growth rates of all wavenumbers. Moreover, the most unstable wavenumber for that swirl ratio has gone from 2 or 3 to 4 or 5. The growth rate values are, except for wavenumber 1, similar to those obtained at around $S = 2.5$ with $\nu = 0.001$.

4.4 Linear Perturbation Structures

Because the linear experiments are too numerous to all be discussed in detail, a subset of eight has been used for displaying the structures of the linear perturbations. The experiments in this set are those underlined in Table 4.1 and they correspond to the axisymmetric solutions shown in Figs. 4.1 - 4.12. These particular linear experiments were chosen to reveal the full qualitative variety of linear wave structures which occurs within the investigated experimental domain, without being overly redundant. Thus, the other experiments are, to a large degree, interpolations of these. In selecting these experiments, an emphasis was put on those representing the most unstable wavenumber for a particular swirl ratio. In addition, experiments 16 and 34 were added to represent extreme departures on either side of the "most unstable wavenumber" zone. (Experiment 33 was not chosen since its growth rate is only 0.05 s^{-1} .)

The structures of the linear perturbations have been illustrated here by reconstructing the sinusoidal perturbation fields from the

complex solutions, as discussed in Section 3.2, and plotting horizontal cross sections of the fields at certain levels. Figs. 4.15 - 4.34, which display the cross sections, follow a particular format: Each figure contains six plots which are grouped into two columns. A column represents one field for a given experiment with the cross sections taken at levels of $1/6$, $3/6$ and $5/6$ of the distance from the lower surface of the baffle. The top figure in a column represents the highest of those levels (nearest the baffle). The u' and v' fields for a given experiment are always grouped together in a figure, as are the w' and p' fields. The other type of field shown, ζ' , is grouped in pairs from different experiments. A set of perpendicular axes is centered over each plot to aid in comparing the locations of various features in the solutions. In addition, a circle representing the location of the maximum axisymmetric vorticity at the given level is included in each plot. This is useful for comparing the radial positions of not only features in different perturbation fields but also perturbation versus axisymmetric features.

The contour lines on the plots denote degrees of strength within the fields with negative values indicated by a dashed pattern. At any given level and radius, a variation in azimuth angle through a range of 2π is accompanied by a sinusoidal fluctuation in the field value. All plots in any given column use the same contour interval so that relative magnitudes at the different levels can be compared. The relative strengths of different fields in a given experiment can be compared by referring to the value of Δ which is shown under each

Figure 4.15. Horizontal cross sections through the linear perturbation fields of u' and v' for $S=0.3$ and $m=1$. In any column, the plots represent three different, equally spaced levels for the same field, and all have the same contour interval as given by Δ . The circle added to each plot denotes the location of the maximum value of ζ for that level. See text for a more complete description.

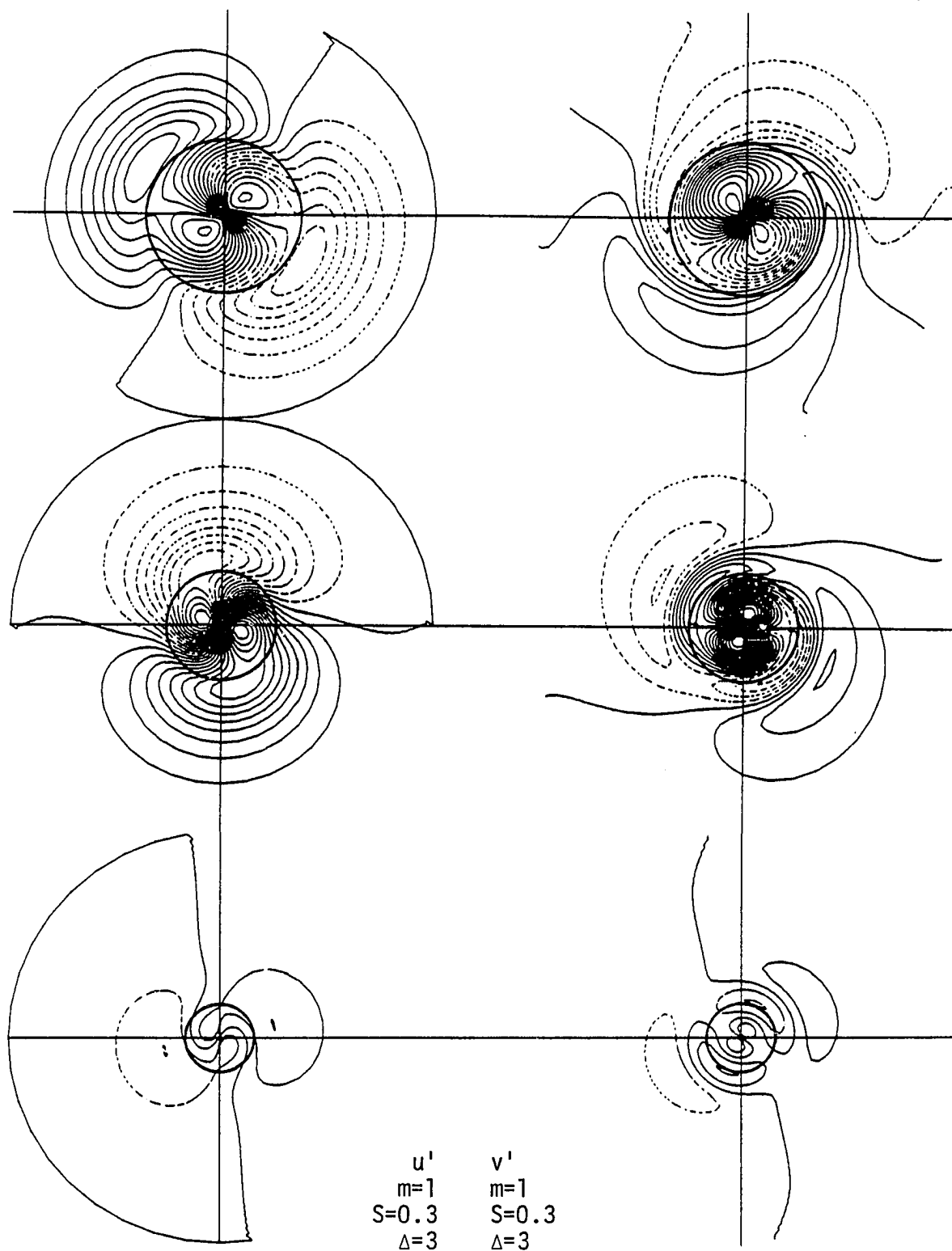


Figure 4.15. Horizontal cross sections through the linear perturbation fields of u' and v' for $S=0.3$ and $m=1$.

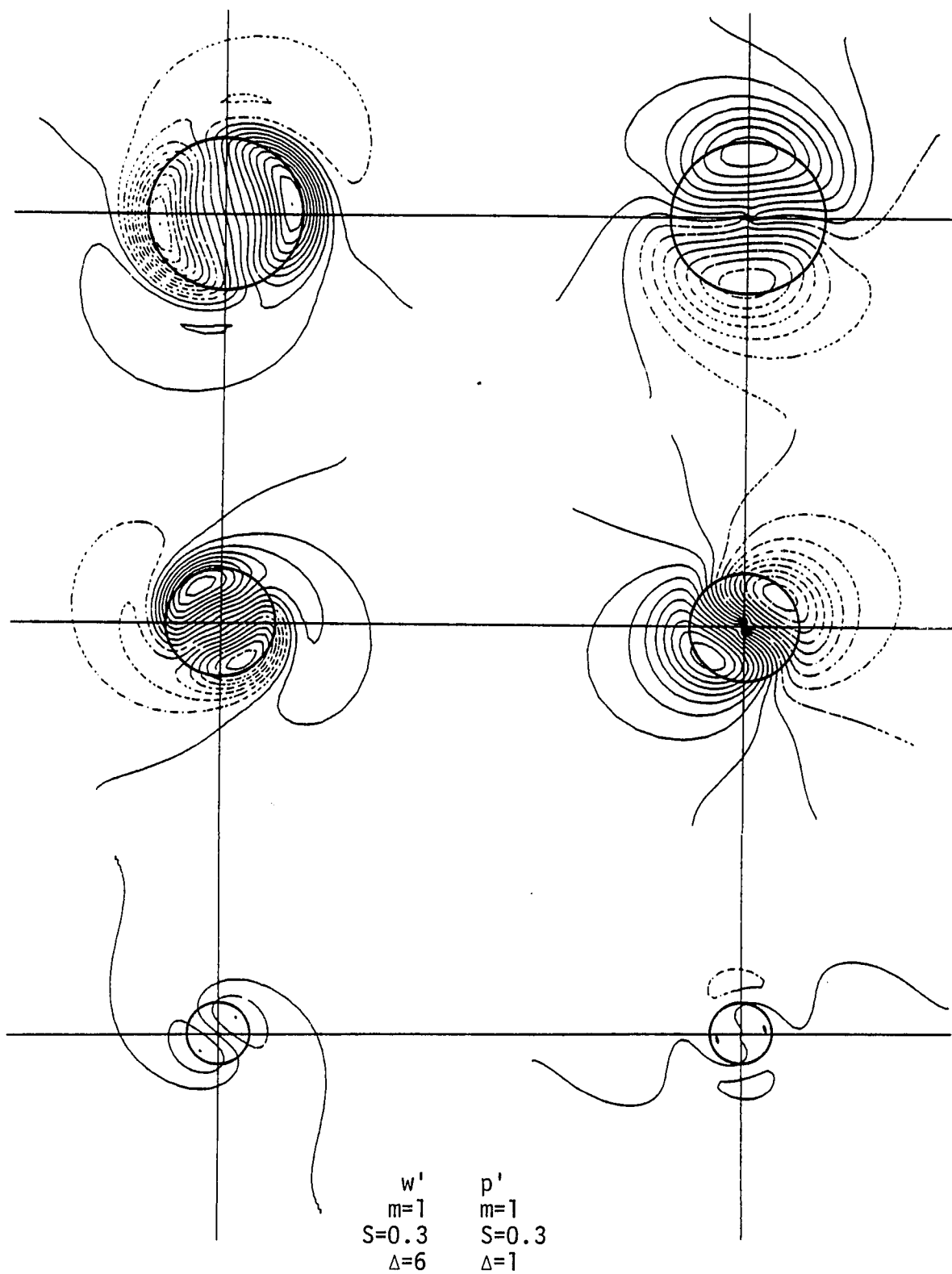


Figure 4.16. Same as in Figure 4.15 but for the fields w' and p' with $m=1$ and $S=0.3$.

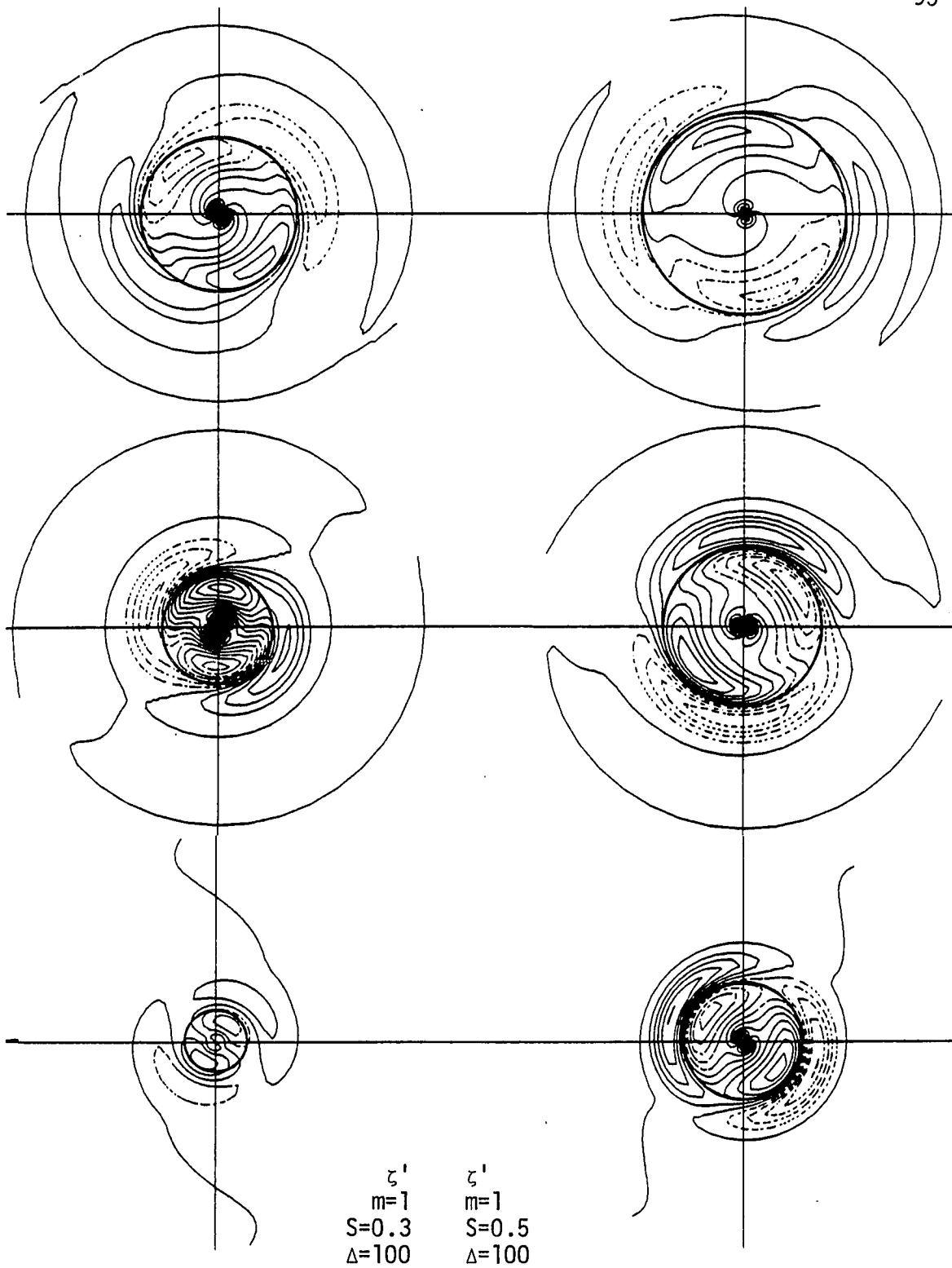


Figure 4.17. Same as in Figure 4.15 but for the fields ζ' with $m=1$ and $S=0.3$, and ζ' with $m=1$ and $S=0.5$.

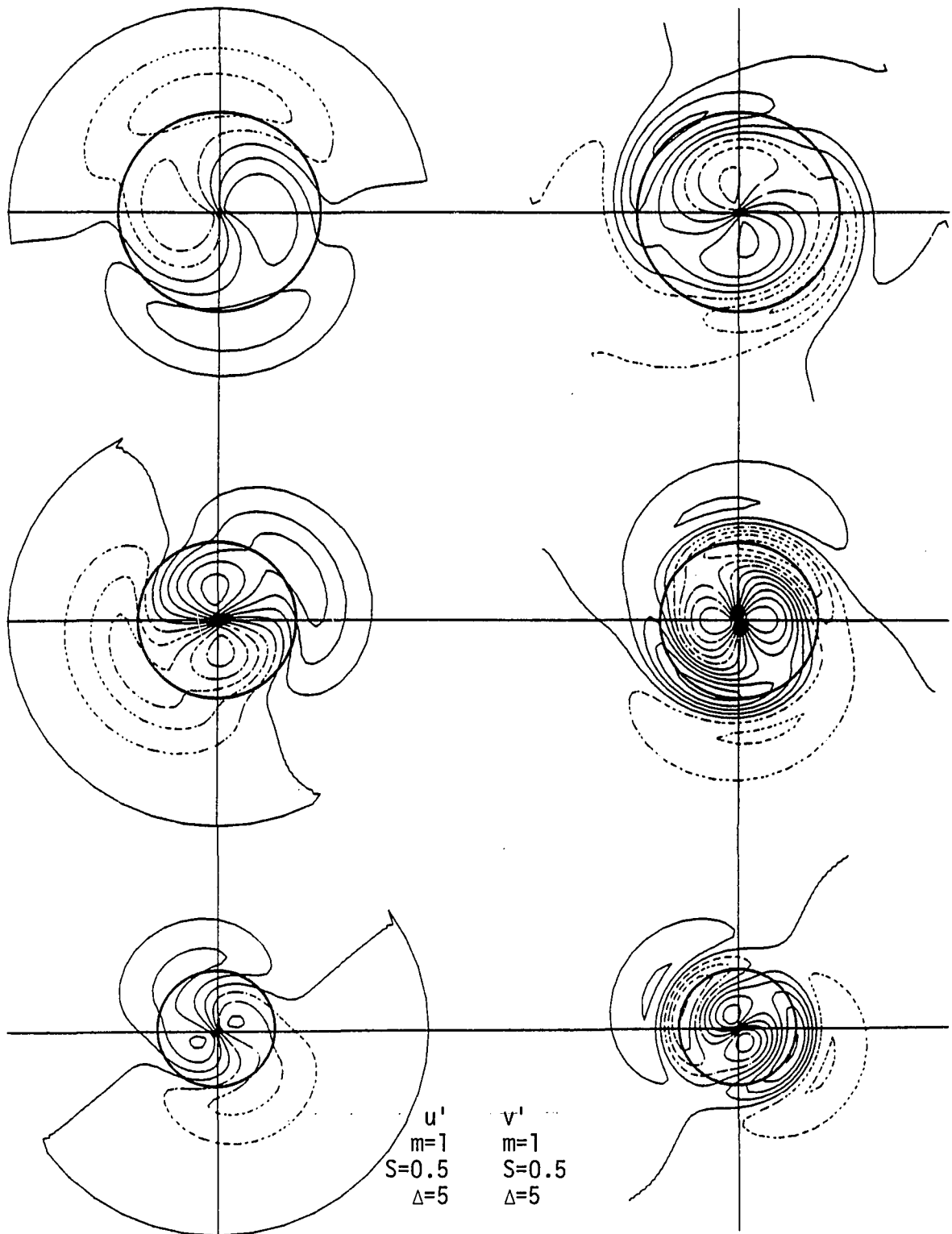


Figure 4.18. Same as in Figure 4.15 but for the fields u' and v' with $m=1$ and $S=0.5$.

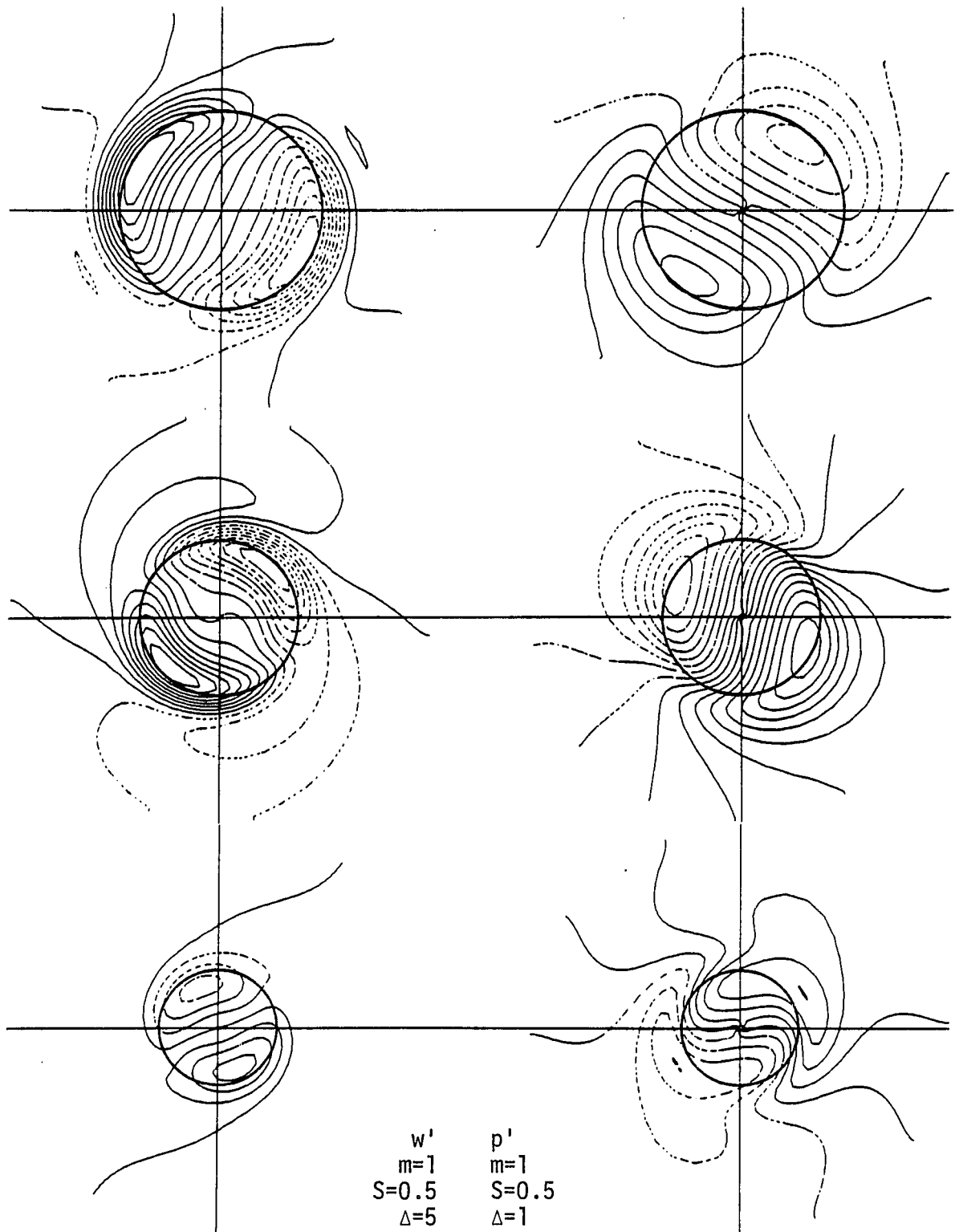


Figure 4.19. Same as in Figure 4.15 but for the fields w' and p' with $m=1$ and $S=0.5$.

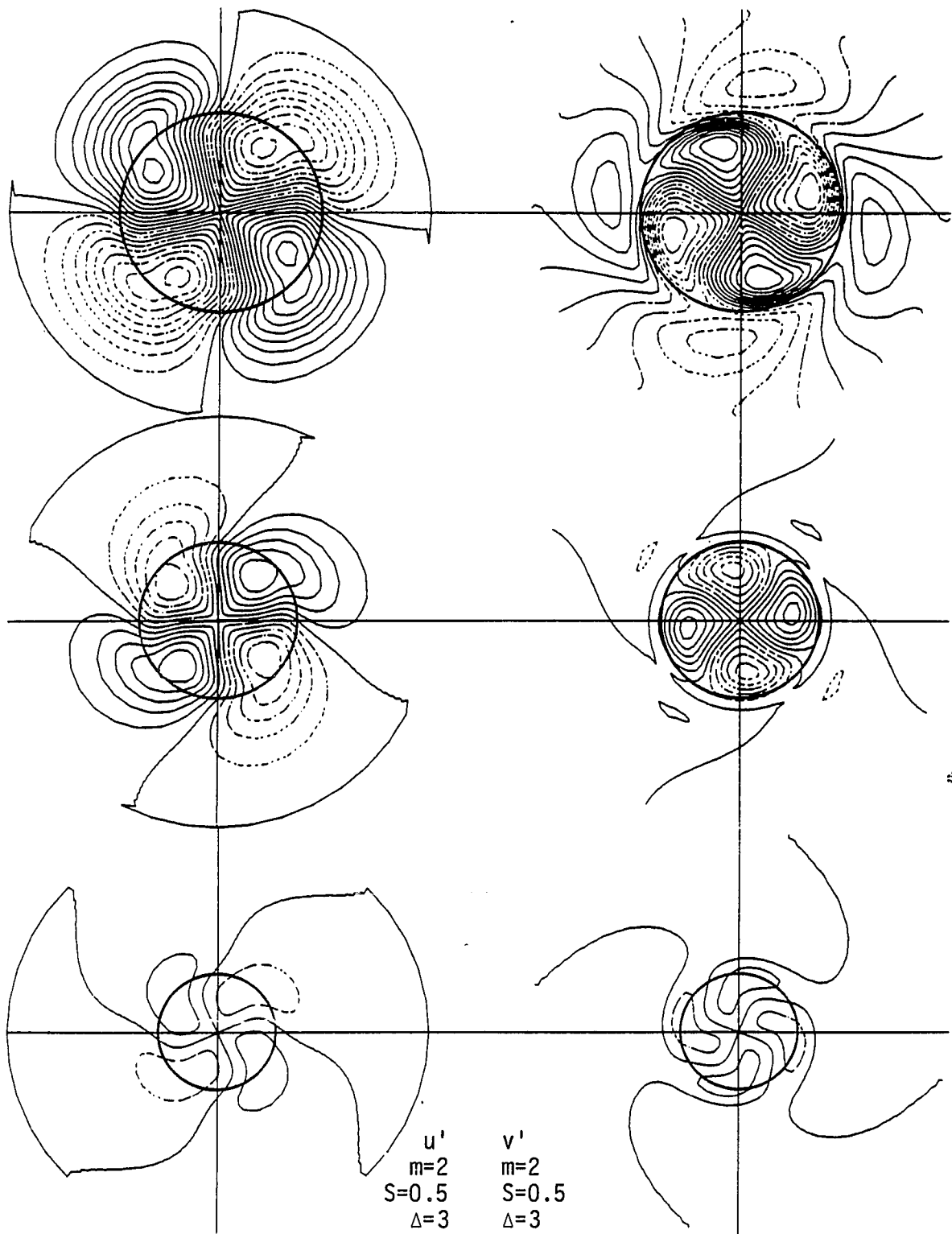


Figure 4.20. Same as in Figure 4.15 but for the fields u' and v' with $m=2$ and $S=0.5$.

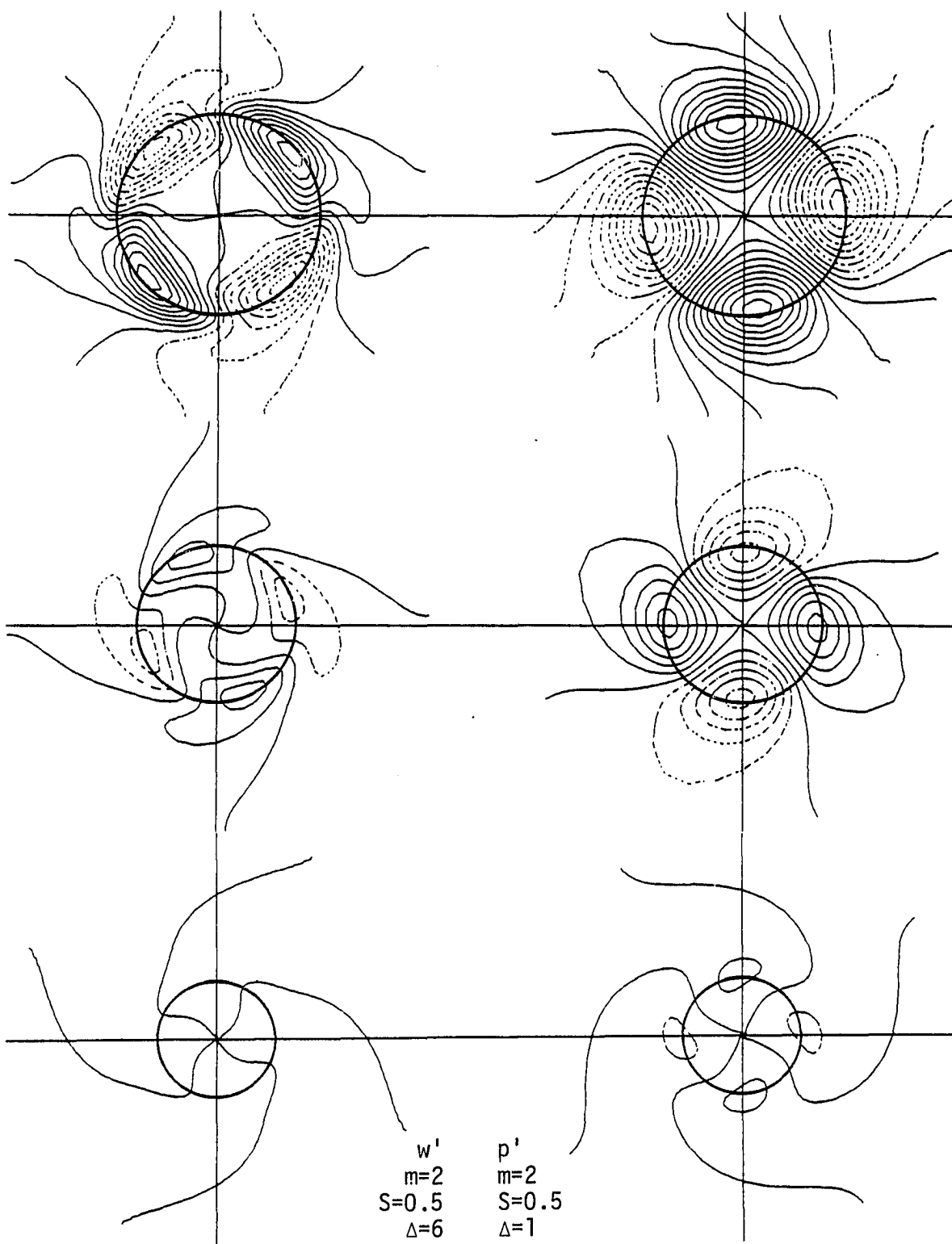


Figure 4.21. Same as in Figure 4.15 but for the fields w' and p' with $m=2$ and $S=0.5$.

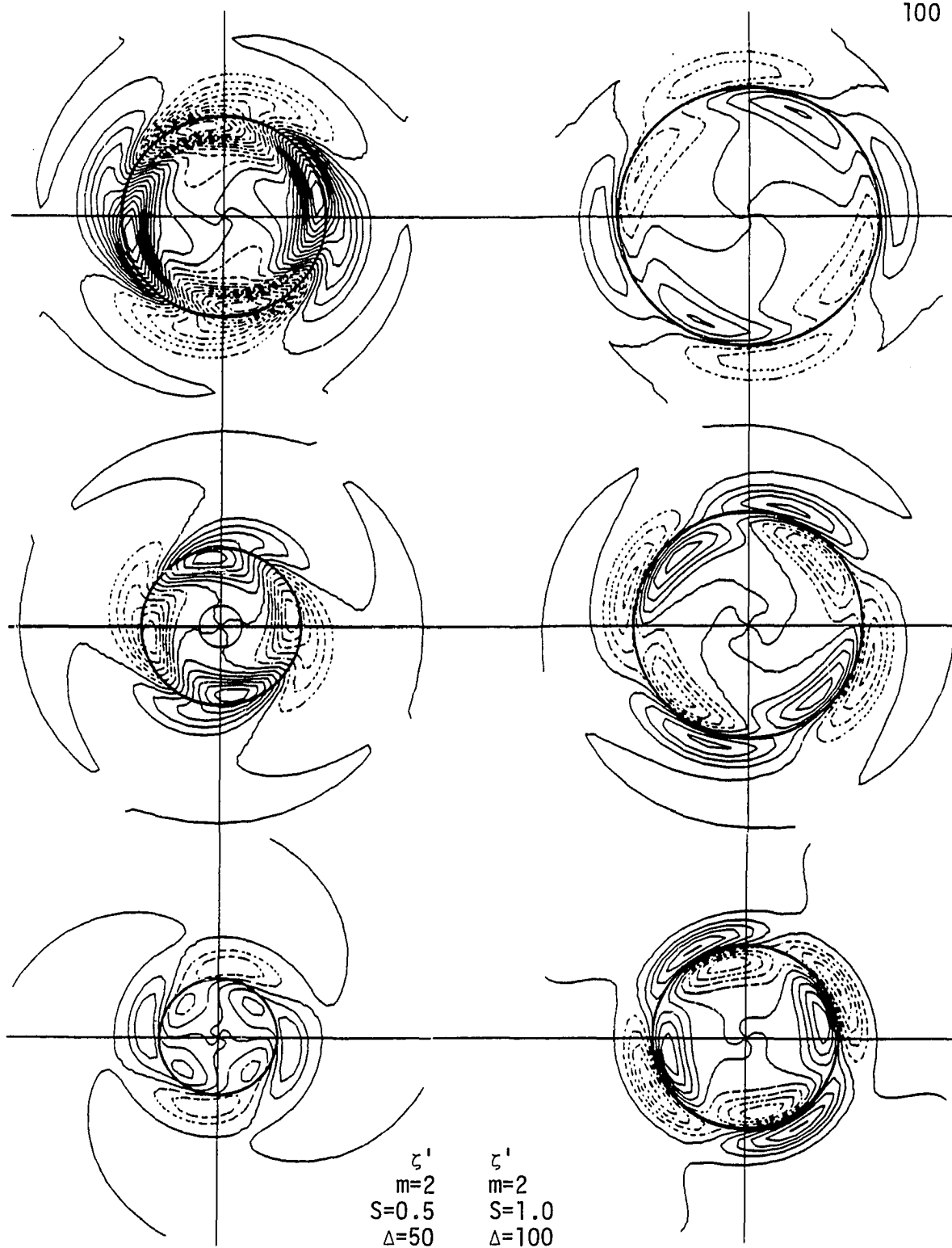


Figure 4.22. Same as in Figure 4.15 but for the fields z' with $m=2$ and $S=0.5$, and z' with $m=2$ and $S=1.0$.

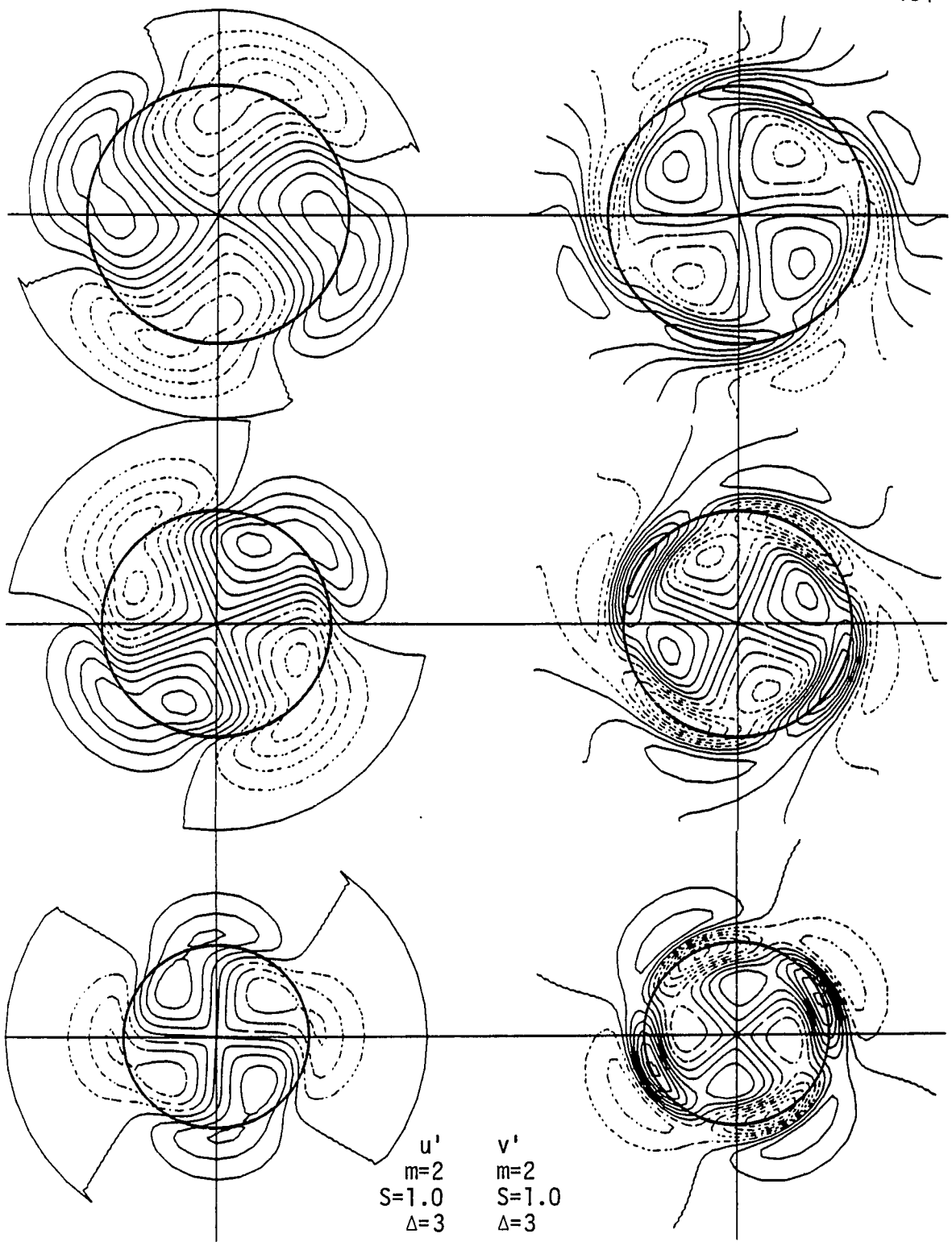


Figure 4.23. Same as in Figure 4.15 but for the fields u' and v' with $m=2$ and $S=1.0$.

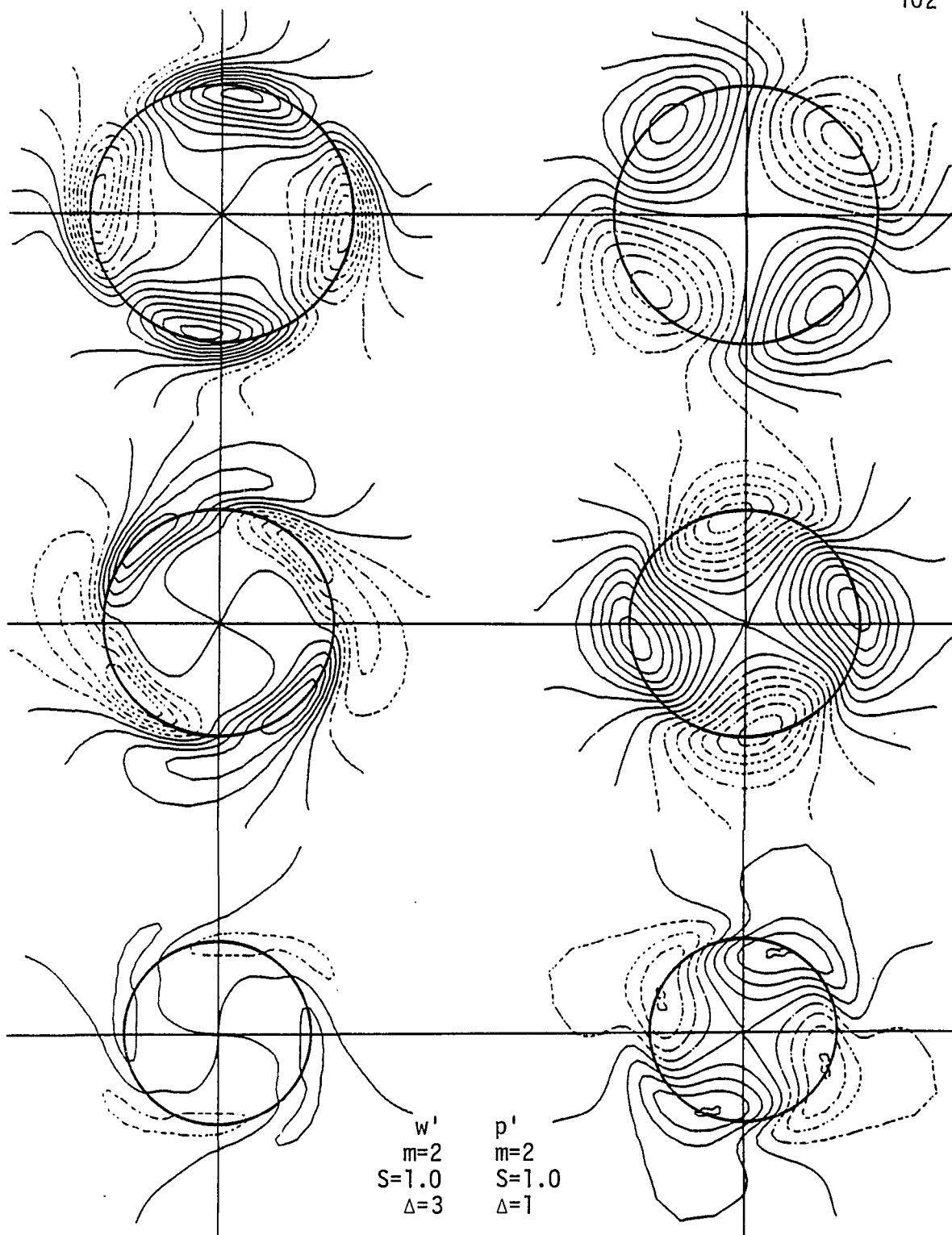


Figure 4.24. Same as in Figure 4.15 but for the fields w' and p' with $m=2$ and $S=1.0$.

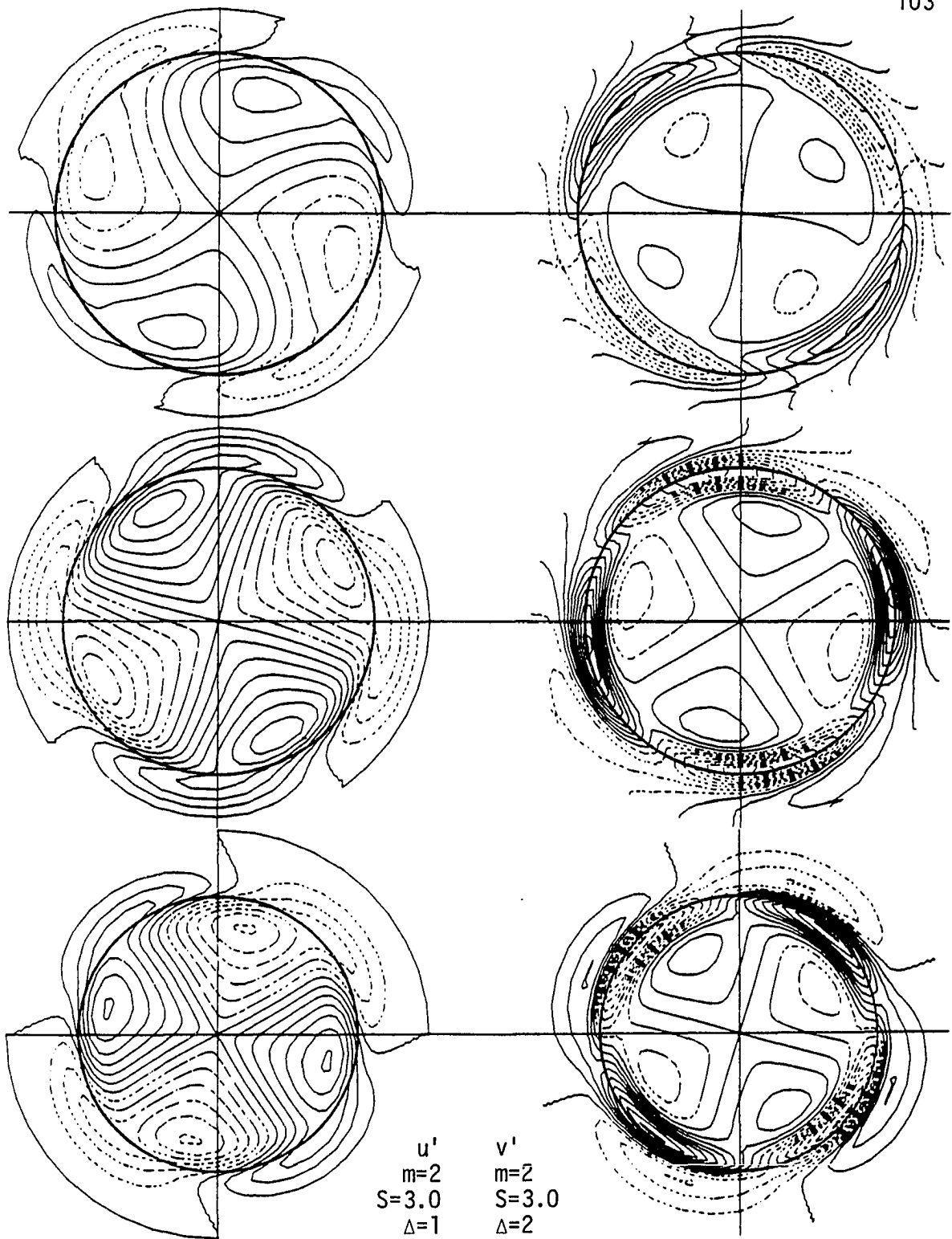


Figure 4.25. Same as in Figure 4.15 but for the fields u' and v' with $m=2$ and $S=3.0$.

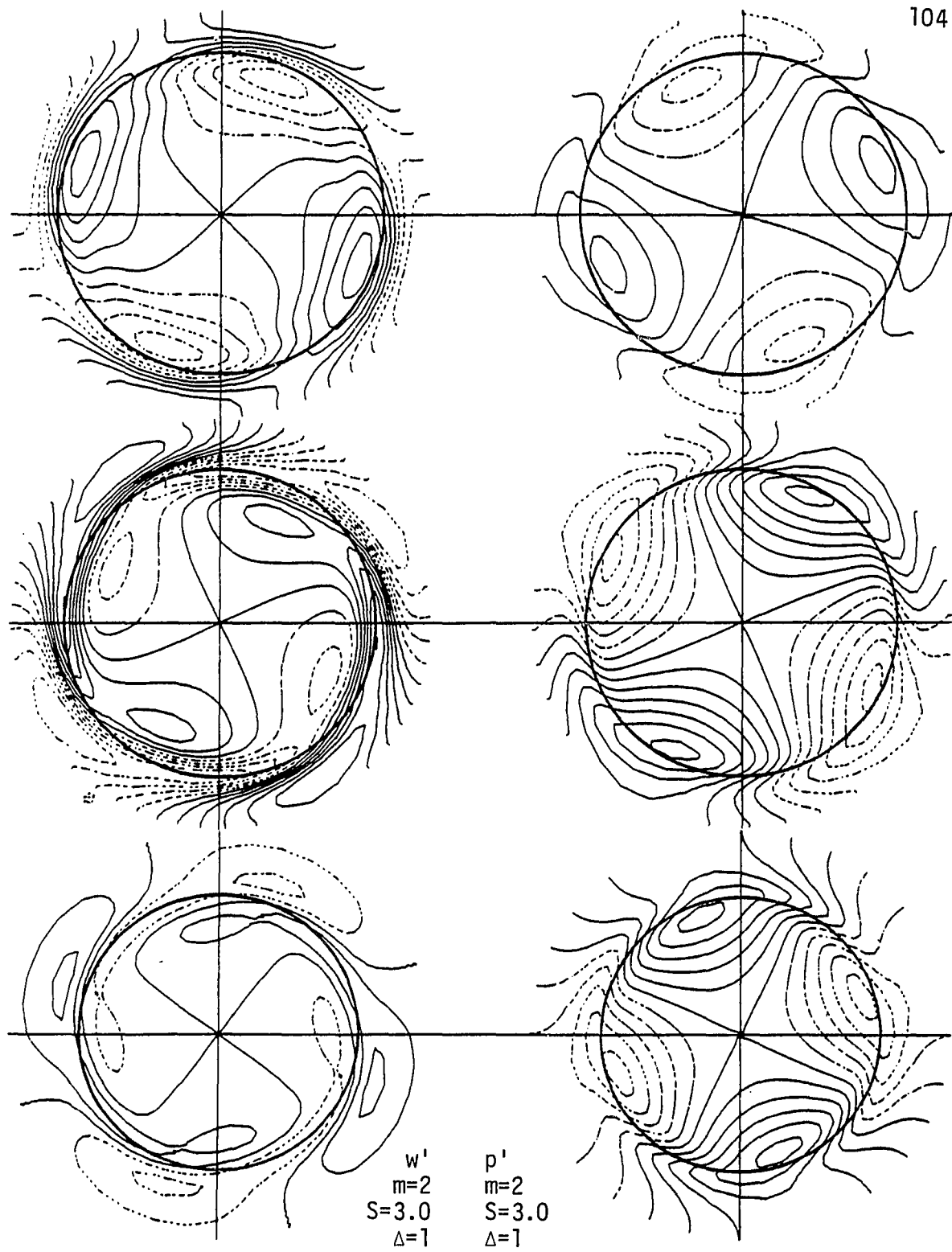


Figure 4.26. Same as in Figure 4.15 but for the fields w' and p' with $m=2$ and $S=3.0$.

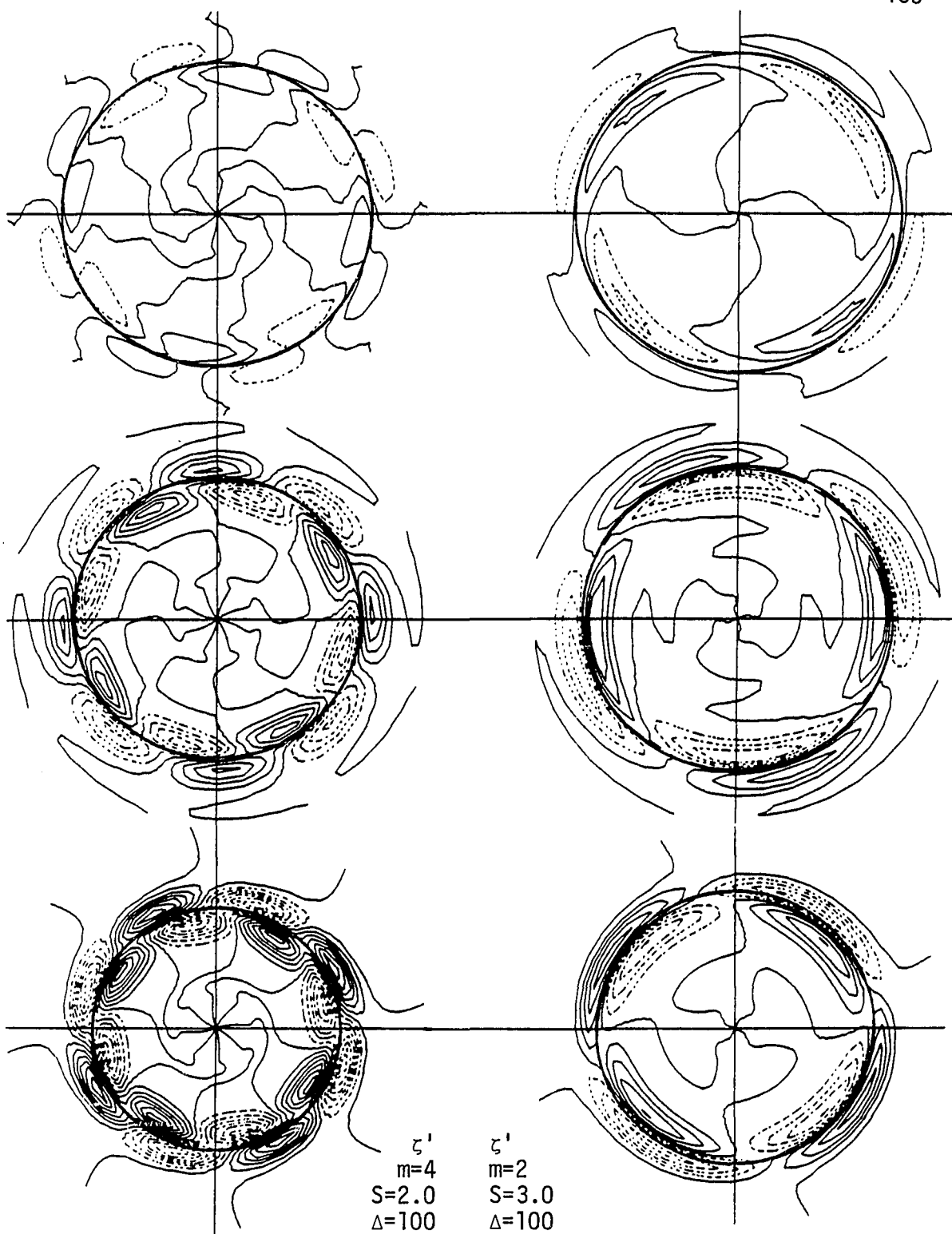


Figure 4.27. Same as in Figure 4.15 but for the fields ζ' with $m=4$ and $S=2.0$, and ζ' with $m=2$ and $S=3.0$.

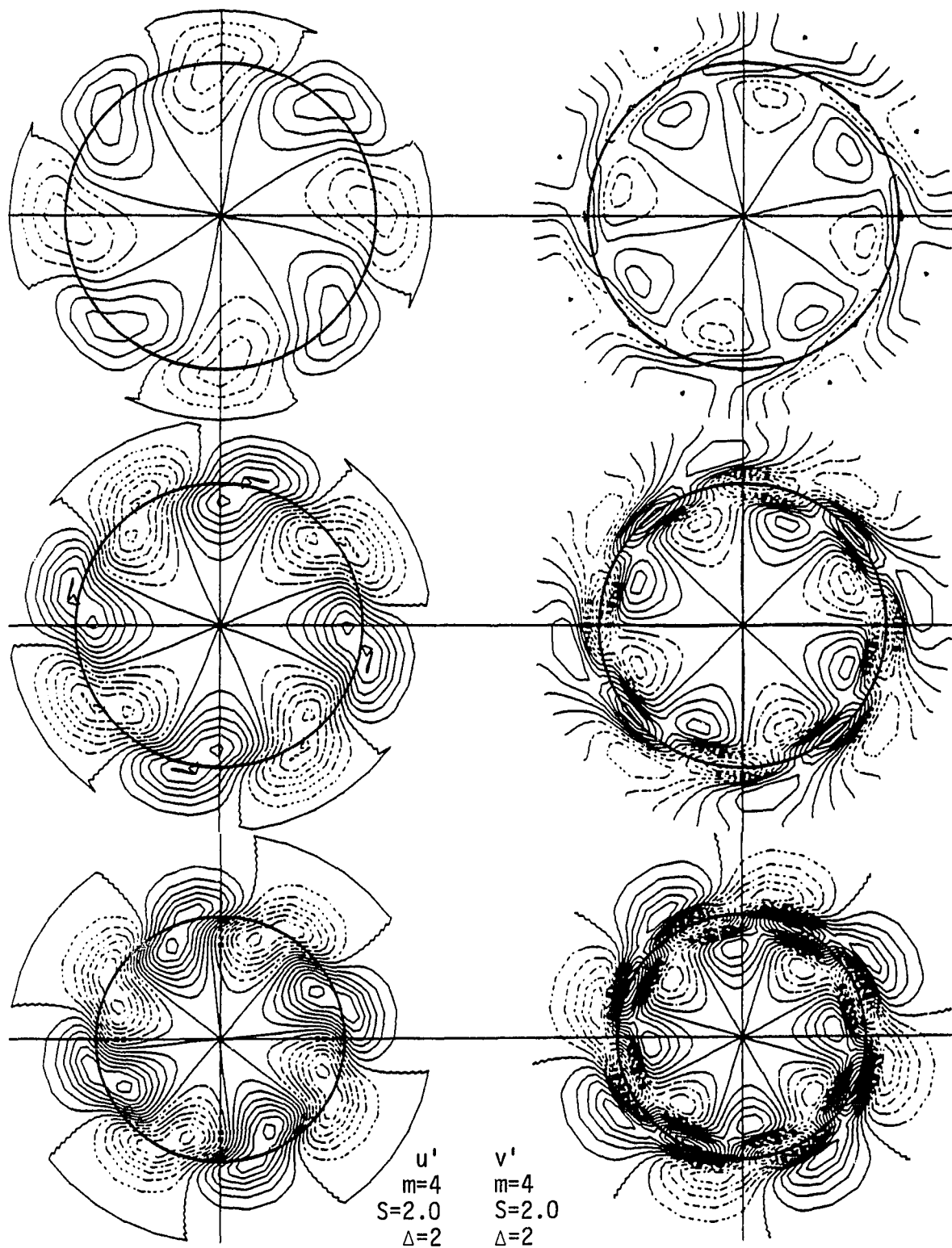


Figure 4.28. Same as in Figure 4.15 but for the fields u' and v' with $m=4$ and $S=2.0$.

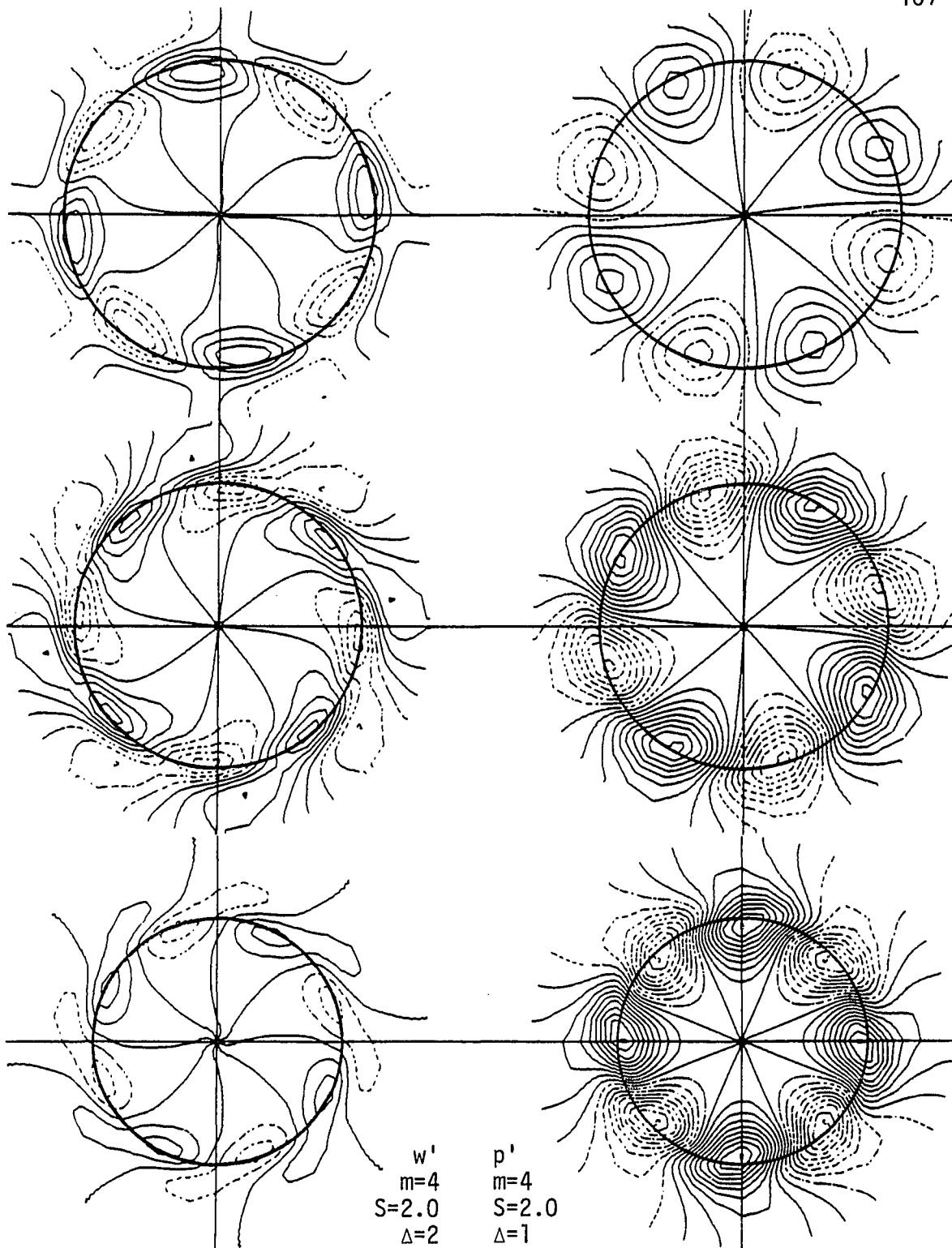


Figure 4.29. Same as in Figure 4.15 but for the fields w' and p' with $m=4$ and $S=2.0$.

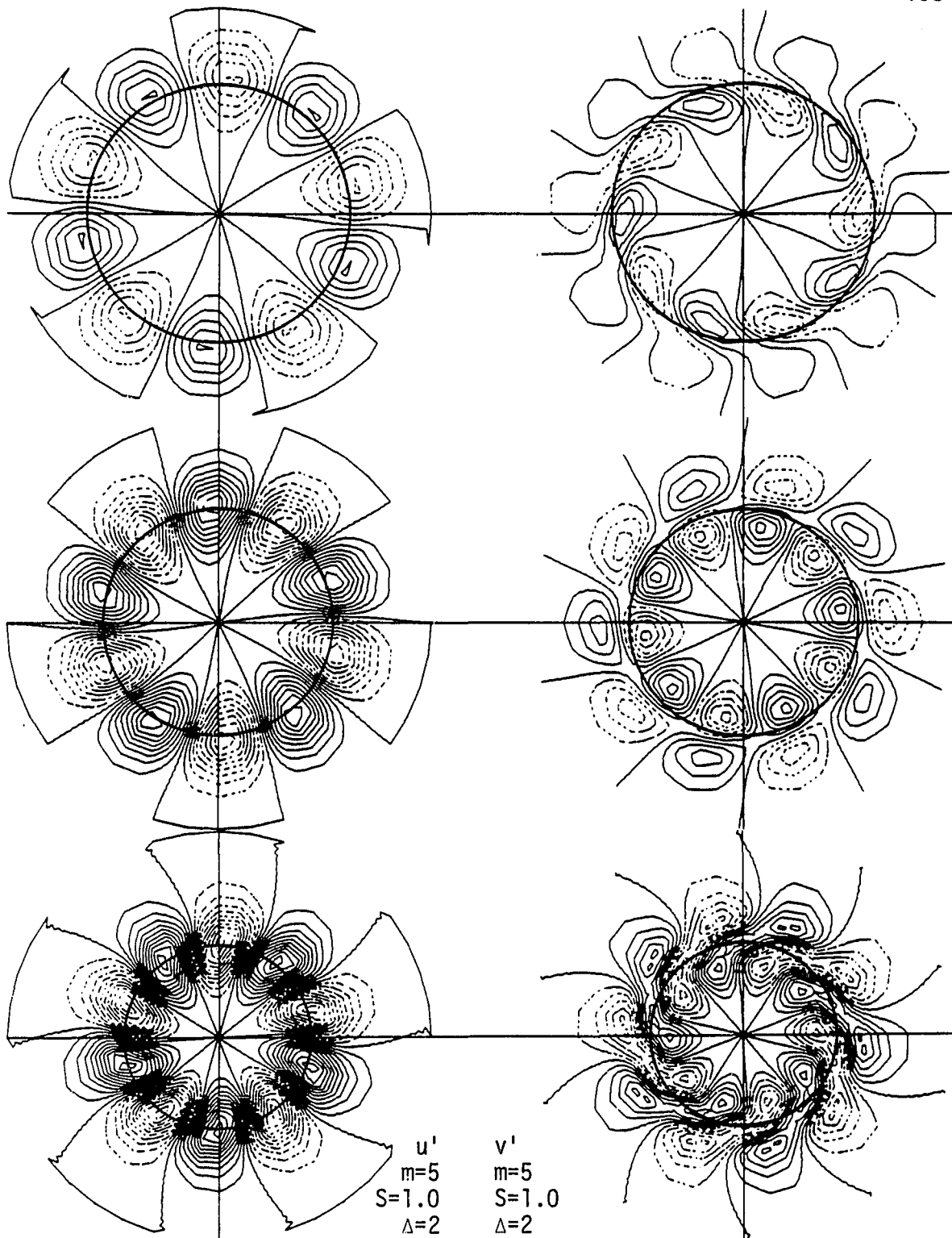


Figure 4.30. Same as in Figure 4.15 but for the fields u' and v' with $m=5$ and $S=1.0$.

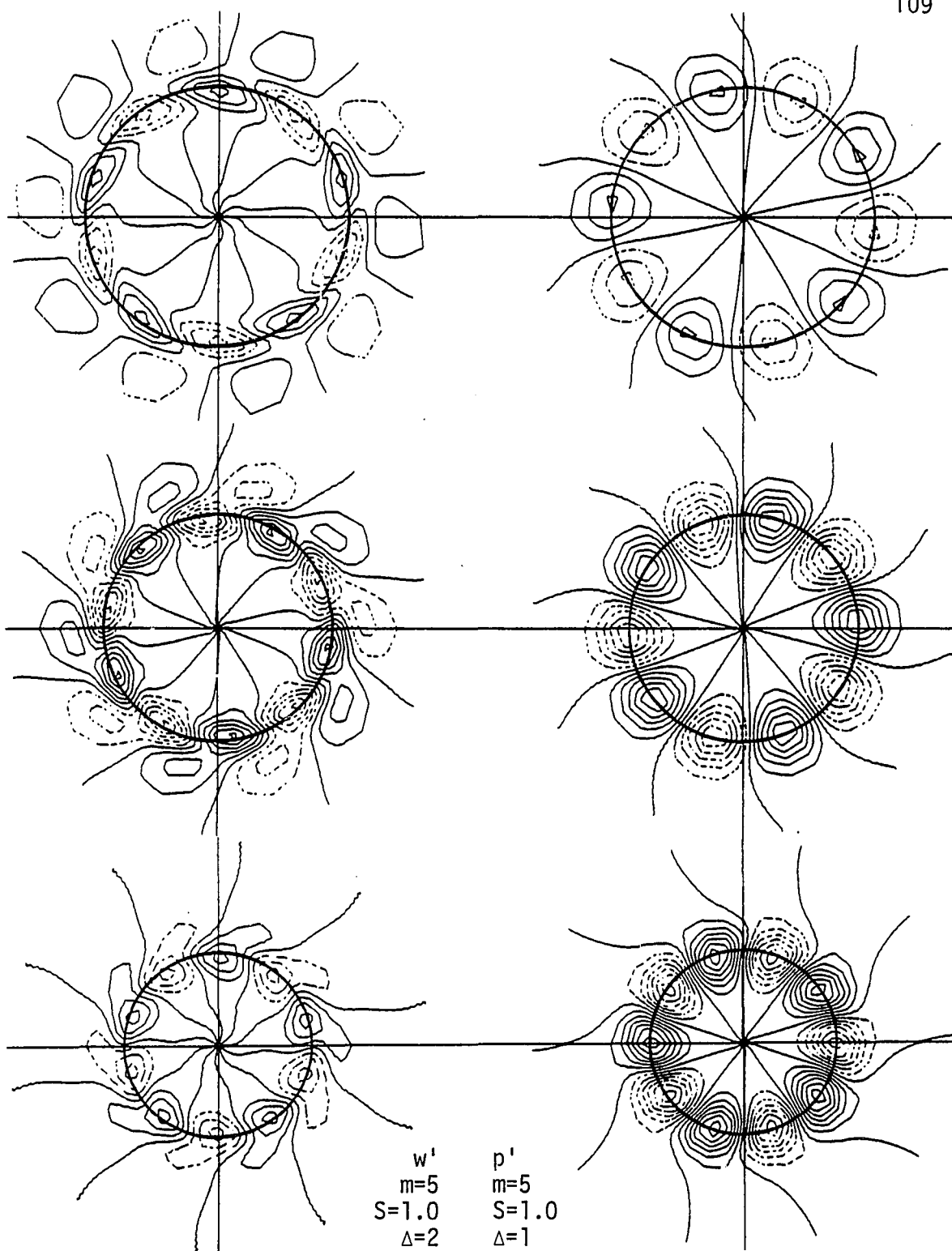


Figure 4.31. Same as in Figure 4.15 but for the fields w' and p' with $m=5$ and $S=1.0$.

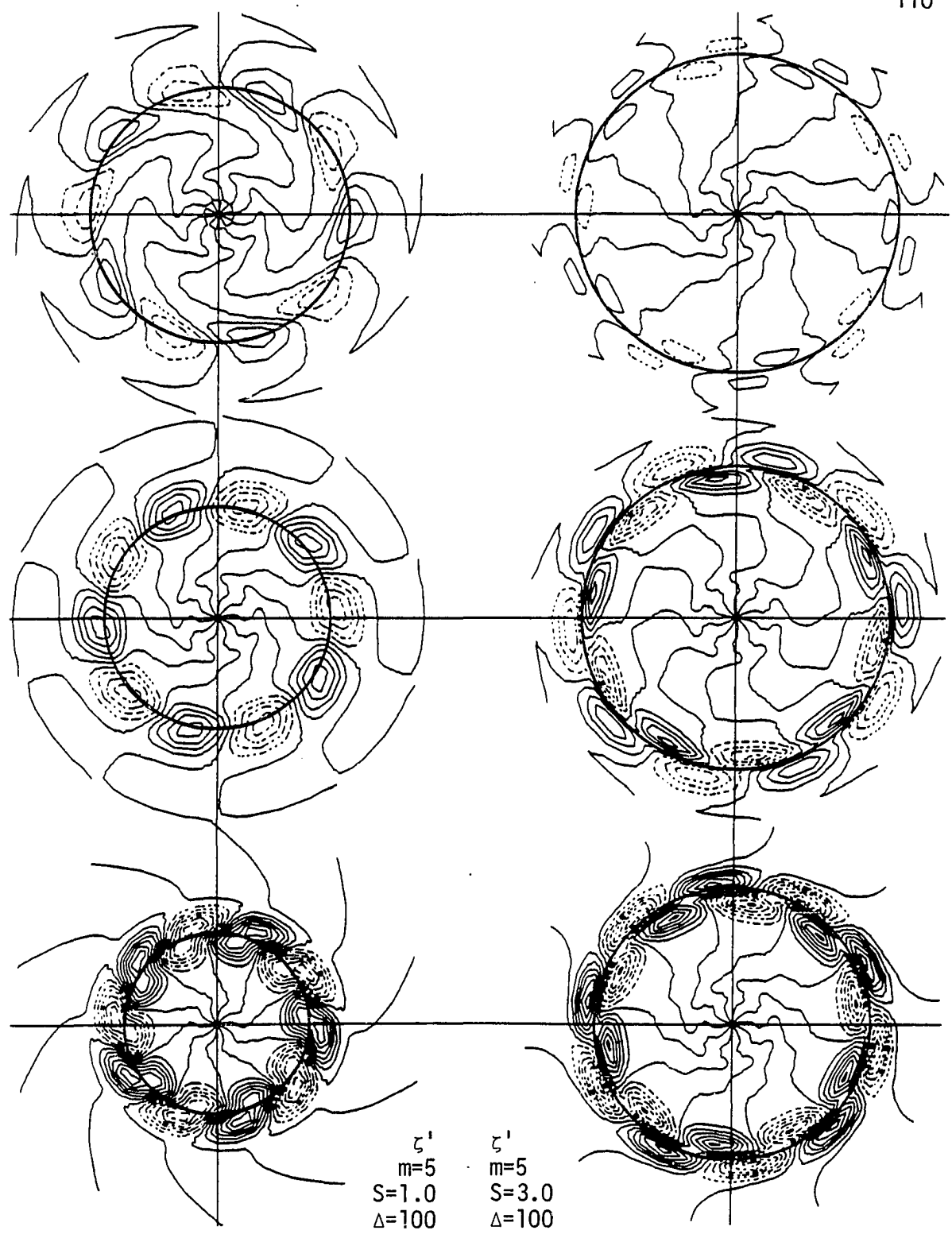


Figure 4.32. Same as in Figure 4.15 but for the fields ζ' with $m=5$ and $S=1.0$, and ζ' with $m=5$ and $S=3.0$.

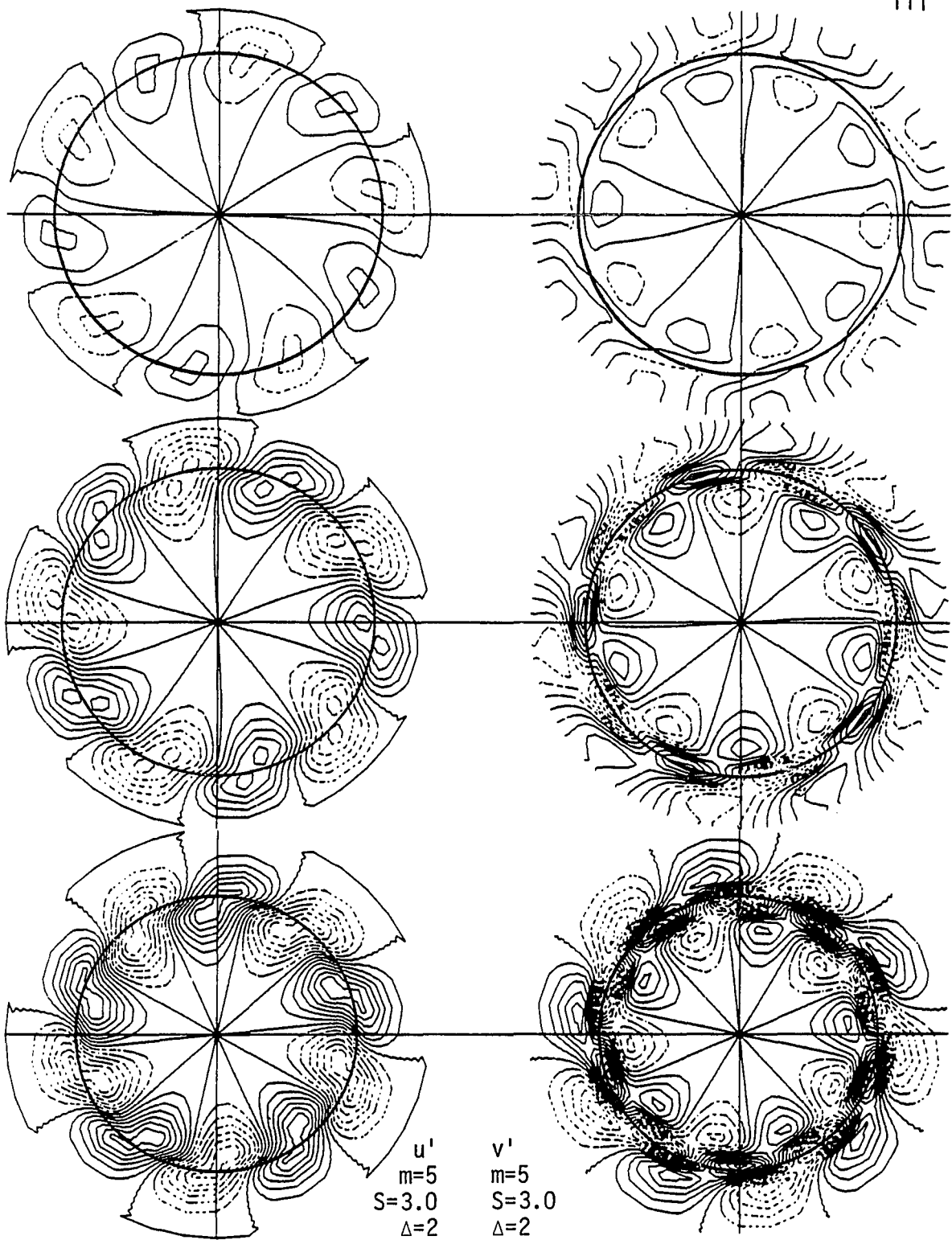


Figure 4.33. Same as in Figure 4.15 but for the fields u' and v' with $m=5$ and $S=3.0$.

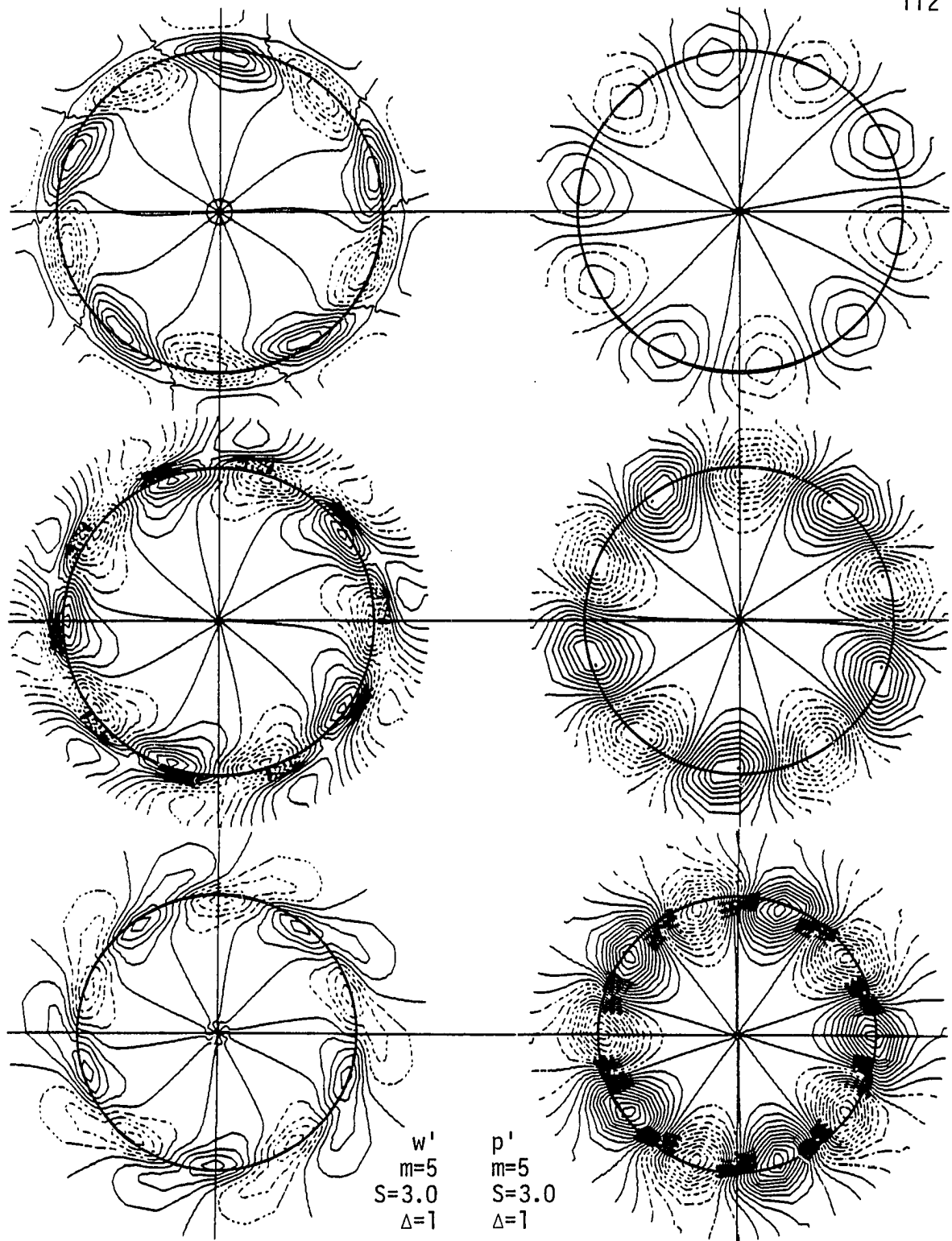


Figure 4.34. Same as in Figure 4.15 but for the fields w' and p' with $m=5$ and $S=3.0$.

column and denotes the contour interval for that column. Of course, the absolute magnitude of a field and the relative magnitudes between different experiments are irrelevant.

An analysis of the perturbation structures is facilitated by choosing one perturbation field as a "reference field" against which all others can be compared. In most cases, the pressure field is the smoothest and contains the least amount of small-scale features so it is the most appropriate for this purpose. Figs. 4.15 - 4.34 indicate that the pressure perturbations nearly always have only a single maximum in the field--that is, only one radius (per level) where a local peak in amplitude occurs. The radius of the maximum increases with the level indicating that the perturbation spreads out with height. From the position of the circle drawn on each plot, it can be seen that the perturbation pressure maximum usually occurs at or just inside the radius of maximum axisymmetric vorticity at all levels. For wavenumber 1, however, the pressure field tends toward a weak double maximum at the lowest level with the maxima lying on either side of the maximum $\bar{\zeta}$. The azimuth angle of a given phase of the perturbation, such as a crest, undergoes a substantial retrogression with height. (Recall that both positive θ and the sense of the rotation of the axisymmetric flow are in the counterclockwise direction.) That retrogression rather than progression occurs is confirmed by examining all levels of the solution rather than just the three shown. The tilt of phase lines with height is approximately the same in the lower and upper portions of a given pressure field, but the amount of tilt is substantially

lower at higher swirl ratios. For example, while at $S = 0.5$ and for wavenumber 2, the total retrogression between levels 1 and 3 amounts to one full wavelength, by $S = 1.0$ it has fallen to $2/3$ wavelength and at $S = 3.0$ to $1/2$ wavelength. For a given swirl ratio, the shorter waves are more nearly vertical than the long ones, although they do tilt a greater fraction of their own wavelength.

The other four fields illustrated in Figs. 4.15 - 4.34 generally have a more complicated structure than does pressure, sometimes with a double or triple maximum, but their overall phase and radial relationship to pressure does not vary appreciably. The u' fields for wavenumbers greater than 1 tend to have a single broad maximum lying on or just inside the radius of maximum \bar{c} . This puts the maxima of u' and p' at the same radius, and u' leads p' by about one fourth wavelength. Occasionally, two weak peaks are apparent within the large u' maximum (e.g., Fig. 4.28, level 2). For wavenumber 1, the double peak is more pronounced and a greater radial and azimuthal separation occurs between the two peaks. (The difference occurs presumably because u' is allowed to be nonzero at the center.) A fairly typical v' field can be found in Fig. 4.28, level 2. A triple maximum is present with the innermost v' maximum lying inside the p' maximum and leading it slightly, the middle v' maximum occurring at the same radius as the p' maximum and trailing it by one fourth wavelength, and the outer v' maximum lying at a still greater radius and trailing the p' maximum by a full half wavelength. Deviations from this structure occur among different experiments and levels primarily in the relative strengths

of the three maxima. The middle maximum is usually the strongest, especially at the lower levels, but is not always present (e.g., note Fig. 4.30 where the middle maximum is totally absent from levels 2 and 3). The w' field has a very similar shape as the v' field and the maxima of the two fields nearly coincide, except that the inner maximum of w' is always weak or nonexistent. In most cases, the "middle maximum" (that lying at the same radius as the p' maximum) is the strongest (e.g., Fig. 4.24), but for $S = 3.0$ and wavenumber 2 (Fig. 4.26), the outer maximum dominates at the lower levels. The ζ' fields usually contain a double maximum with the splitting between the peaks generally more pronounced at the lower levels. One peak lies on either side of the $\bar{\zeta}$ maximum with the outer peak always trailing the inner one. The point midway between the peaks very closely coincides with the location of minimum pressure (for example, compare Figs. 4.27 and 4.29). The separation between the two ζ' maxima tends to increase with S and decrease with wavenumber. As extreme examples, note in Fig. 4.32 ($S = 1.0$) that virtually no separation occurs and that in Fig. 4.27 ($S = 3.0$) the separation reaches one half wavelength. Note the implication of these comparisons that because all perturbation fields maintain the same relative positions at each level, they all exhibit the same tilt and radial spreading with height as does the perturbation pressure. Also implied is the fact that, since the radius of the maximum axisymmetric vertical vorticity increases with S , all perturbation fields do likewise.

A major influence which the swirl ratio and wavenumber have on the linear perturbation structure is in the relative strengths of the different fields at the different levels. While u' , v' , p' and ζ' all tend to have larger amplitudes at the middle and lowest levels throughout most of the parameter space, notable exceptions occur for $S = 0.3$ with $m = 1$ (Figs. 4.15 - 4.17) and $S = 0.5$ with $m = 2$ (Figs. 4.20 - 4.22). There, the amplitudes of all fields (including w') are unusually weak at level 1. By comparing the contour intervals (given by Δ) and the number of contour lines for the various fields within any given experiment, it can be seen that both the swirl ratio and wavenumber can greatly alter the comparative amplitudes of the fields. This is further indicated by Table 4.2, which includes all linear experiments performed. Entries in the table are quotients denoting the maximum amplitude of each velocity field and the ζ' field, occurring over all levels, relative to that of p' . It can be seen that within the given range of parameter space, the quotient u'_{\max}/p'_{\max} varies by a factor of more than 3. The quotient always decreases with S and usually increases with wavenumber. On the other hand, v'_{\max}/p'_{\max} , which varies by a factor of more than 4, nearly always decreases with wavenumber and is rather irregular with the swirl ratio. The quotient w'_{\max}/p'_{\max} has the highest variability in the domain, ranging by more than a factor of 10, and always decreases with S while generally decreasing slowly with wavenumber. The quantity ζ'_{\max}/p'_{\max} varies only by a factor of 2 and is highly variable with both S and wavenumber.

Table 4.2. A comparison of the maximum amplitudes (over all levels and radii) of different perturbation fields within the same experiment as a function of swirl ratio and wavenumber. Entries are grouped in blocks of four and represent the quotients u'_{\max}/p'_{\max} , v'_{\max}/p'_{\max} , w'_{\max}/p'_{\max} and ζ'_{\max}/p'_{\max} in the order given. Numerical values are appropriate to MKS units.

SWIRL RATIO	m=1	m=2	m=3	m=4	m=5	m=6
0.3	3.9					
	4.6					
	6.2					
	103					
0.5	3.2	2.9				
	3.5	2.5				
	4.6	4.7				
	82	89				
0.7	2.6	2.4	2.9			
	3.3	2.0	2.3			
	3.9	3.9	2.2			
	75	47	94			
1.0	2.1	2.1	2.4	2.9	3.1	
	3.9	2.4	2.9	2.2	1.6	
	3.0	2.9	1.8	1.8	1.5	
	87	67	96	100	100	
1.5	1.5	1.7	1.8	2.0	2.3	
	4.1	3.0	2.8	2.1	1.6	
	1.9	1.7	1.4	1.2	1.2	
	82	73	84	78	81	
2.0	1.3	1.4	1.6	1.7	1.7	
	4.1	3.0	2.7	2.2	1.6	
	1.6	1.2	1.1	0.9	0.9	
	82	79	84	76	70	
2.5	1.2	1.2	1.3	1.4	1.5	1.4
	4.2	2.7	2.5	2.1	1.6	1.1
	1.4	1.0	0.9	0.8	0.7	0.6
	82	74	75	68	60	59
3.0	1.1	1.1	1.2	1.1	1.1	1.2
	4.3	2.6	2.4	1.9	1.5	1.2
	1.2	1.0	0.7	0.7	0.7	0.6
	86	74	72	64	57	55

4.5 Energy Budgets of Linear Perturbations

Recall from Section 3.7 that an energy equation (Eq. 3.27) was derived which partitions the energy gained or lost by the linear perturbations into nine individual components. These components are relisted here and numbered for convenience.

$$\text{Term 1} \quad \iiint \left[u'v' \left(\frac{\bar{v}}{r} - \frac{\partial \bar{v}}{\partial r} \right) \right] r \, dr \, d\theta \, dz$$

$$\text{Term 2} \quad \iiint \left[-u'w' \frac{\partial \bar{w}}{\partial r} \right] r \, dr \, d\theta \, dz$$

$$\text{Term 3} \quad \iiint \left[-u'u' \frac{\partial \bar{u}}{\partial r} - v'v'\bar{u} \right] r \, dr \, d\theta \, dz$$

$$\text{Term 4} \quad \iiint \left[-v'w' \frac{\partial \bar{v}}{\partial z} \right] r \, dr \, d\theta \, dz$$

$$\text{Term 5} \quad \iiint \left[-w'w' \frac{\partial \bar{w}}{\partial z} \right] r \, dr \, d\theta \, dz$$

$$\text{Term 6} \quad \iiint \left[-w'u' \frac{\partial \bar{u}}{\partial z} \right] r \, dr \, d\theta \, dz$$

$$\text{Term 7} \quad \iint \left[(-\bar{w}E')_{\text{TOP}} \right] r \, dr \, d\theta$$

$$\text{Term 8} \quad \iiint \left[u'F_r' + v'F_\theta' + w'F_z' \right] r \, dr \, d\theta \, dz$$

$$\text{Term 9} \quad \iint \left[\left(-\frac{p'w'}{\rho} \right)_{\text{TOP}} \right] r \, dr \, d\theta$$

The sum of all terms is equal to the expression

$$\frac{\partial}{\partial t} \iiint E' r dr d\theta dz$$

which is the tendency of the total energy in the perturbation. An inspection of each term will reveal its interpretation in terms of the type of energy source or sink which it describes. Terms 1-7 can be seen to represent different types of interactions between the perturbation and the axisymmetric flow while terms 8 and 9 involve the perturbation only. Term 1 describes the interaction of the perturbation with the azimuthal component of the axisymmetric flow, specifically $-\frac{\partial \bar{v}}{\partial r} + \frac{\bar{v}}{r}$. This quantity represents a shearing deformation in the horizontal plane and tends to be positive outside the maximum of \bar{v} , negative just inside the maximum \bar{v} , and near zero at still lower radii. Thus, if the correlation $u'v'$ tends to be positive outside \bar{v}_{\max} and negative just inside the maximum, the perturbation will extract energy from the axisymmetric flow. An analogous argument applies to the next five terms. Term 2 relates the perturbation to the radial shear of \bar{w} , while term 3 involves the radial derivative of \bar{u} as well as the quantity $\frac{\bar{u}}{r}$ which is also a stretching term. Terms 4-6 are energy sources or sinks which depend on the vertical derivatives of \bar{v} , \bar{w} and \bar{u} , respectively. Term 7 may be interpreted as the advection of perturbation kinetic energy outward through the baffle by the axisymmetric vertical velocity \bar{w} . This integral is always negative since E' is always assumed to be zero outside the domain and thus cannot be

advected inward. Term 8 represents turbulent dissipation within the perturbation and is likewise always negative. Term 9 is a surface pressure-work term representing the fact that when high perturbation pressure is positively correlated with downward velocity at the baffle, a net positive work is done on the fluid beneath the baffle.

The magnitudes of terms 1-8 as they occur in linear experiments 1-38 are plotted as a function of swirl ratio and wavenumber in Fig. 4.35. (Term 9 has not been included because it is very near zero for all cases.) The figure contains 33 separate histograms, each representing a particular linear experiment where amplification took place, and the little square in each histogram is intended as a locator relating to the coordinate axes. The energy terms 1-8 are plotted in order from left to right with four on either side of the square. The vertical extent of any bar denotes its relative magnitude with up indicating positive values, and down, negative values. For each experiment, the energy terms are normalized by dividing by twice the total kinetic energy of the perturbation. Therefore, the energy terms can be compared from one experiment to another as well as within a given experiment. Note that the normalization causes the plotted terms to have a dimension of t^{-1} which is equivalent to a growth rate. Thus, the sum over all terms in any experiment gives the growth rate for that perturbation. The small increments along the vertical axes denote growth-rate units of $0.1 s^{-1}$.

A quick inspection of the histograms shows that either term 1 or term 2 is always the primary energy source for the perturbation.

Figure 4.35. Histograms showing the contributions of eight individual sources (or sinks) of energy for the perturbations as a function of swirl ratio and wavenumber. The small square within each histogram serves to locate the proper positions on the coordinate axes. The height of an individual bar denotes the rate of energy input divided by twice the total energy in the perturbation, and thus is equivalent to a growth rate. The small increments along the vertical axis denote growth rate units of 0.1 s^{-1} .

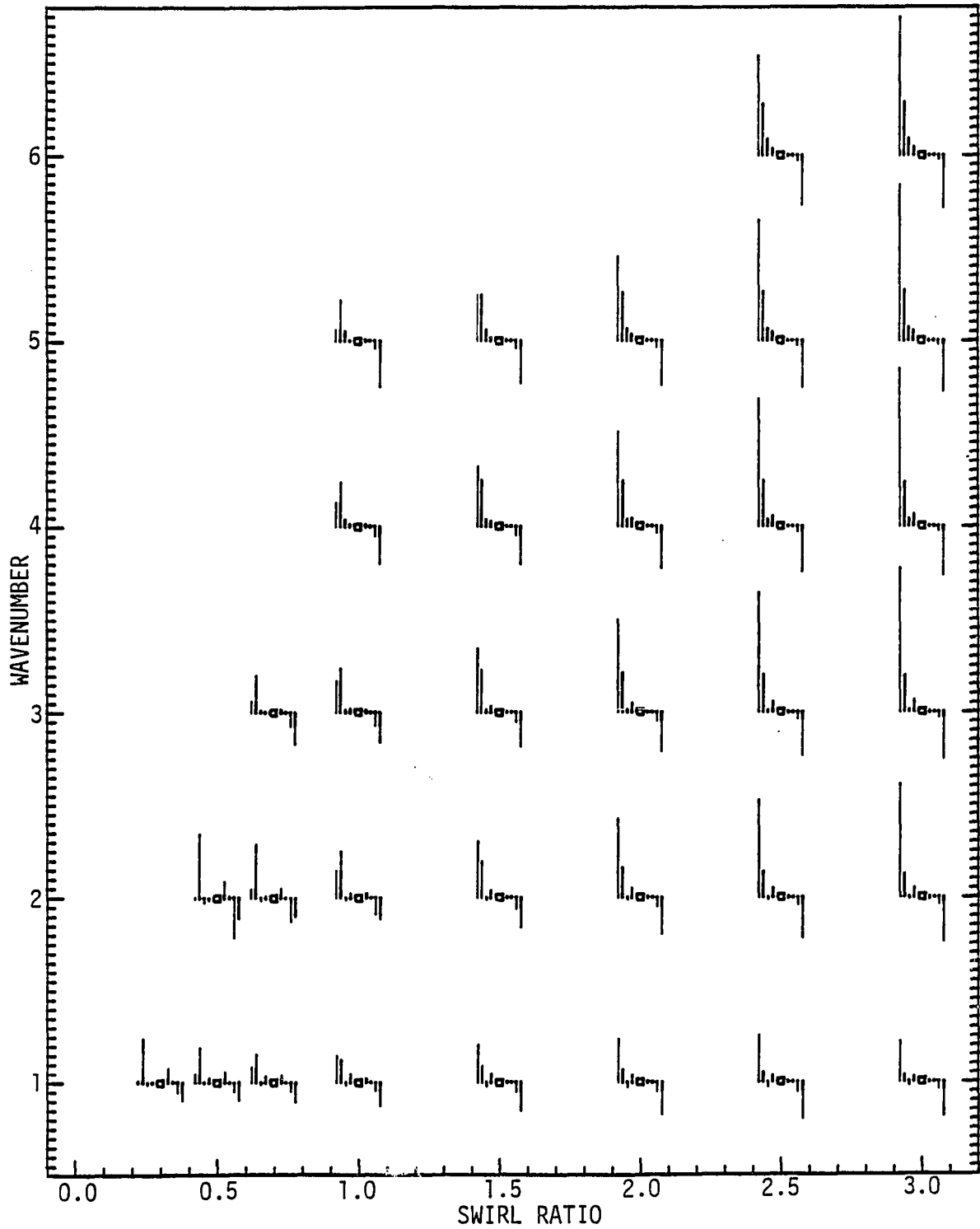


Figure 4.35. Histograms showing the contributions of eight individual sources (or sinks) of energy for the perturbations as a function of swirl ratio and wavenumber.

For all wavenumbers other than 1, term 1 increases in magnitude monotonically with S within the given domain. For wavenumber 1, term 1 begins to decrease with S at around $S = 2.5$. (Recall that wavenumber 1 approaches zero growth at high S .) Term 2 shows a strong tendency to decrease with S for wavenumbers 1 and 2 while for the shorter waves, it remains relatively unchanged. The net result is that term 2 dominates at and below $S = 1.0$ (at and below $S = 0.7$ for wavenumber 1) while term 1 dominates elsewhere. Note that for any given swirl ratio, term 2 becomes more important relative to term 1 with increasing wavenumber. For the majority of experiments, term 8 is the primary energy sink and tends to increase in magnitude both with S and wavenumber. Term 7, normally fairly close to zero in magnitude, does become significant for the longer waves and lower swirl ratios, and actually exceeds term 8 as an energy sink for wavenumber 2 and $S \leq 0.7$. A positive energy contribution to the perturbation is sometimes made by terms 3-5, although in terms of relative importance among the various sources, the contribution is usually small. Term 5 does make a significant contribution for $S \leq 0.5$, representing as much as 25% of the total energy source. Term 6 is always near zero.

4.6 Phase Speeds of Linear Perturbations

In Section 3.6, it was demonstrated that the linear solutions propagate in the azimuthal direction with a constant angular velocity ω . The steady state values of ω resulting from experiments 1-38 are listed in Table 4.3 in units of degrees per second. The angular velocity can be seen to increase substantially with S , particularly for the

Table 4.3. Angular velocity ω (rate of change of θ) in degrees per second of linear perturbations as a function of swirl ratio and wavenumber. Also shown are the maximum values of \bar{v}/r occurring in the axisymmetric flow at each of three different levels.

SWIRL RATIO	MAXIMUM VALUE OF \bar{v}/r IN AXISYMMETRIC FLOW			WAVENUMBER					
	LOWER SURFACE	MIDDLE LEVEL	BAFFLE LEVEL	m=1	m=2	m=3	m=4	m=5	m=6
0.3	133	60	24	58					
0.5	100	54	28	57	55				
0.7	95	51	28	64	59	66			
1.0	100	63	40	77	66	68	69	72	
1.5	114	75	54	98	80	76	75	76	
2.0	129	91	67	119	95	86	84	84	
2.5	144	93	82	137	109	98	93	92	93
3.0	159	115	97	150	124	110	104	102	102

longer waves. Values range from less than 60 degrees per second at $S \leq 0.5$ to 150 degrees per second at $S = 3.0$ and wavenumber 1.

Also shown in Table 4.3 is the maximum angular velocity (that is, the maximum value of $\frac{\bar{v}}{r}$) which occurs in the axisymmetric vortex at the lower surface, the middle level, and the baffle. In all cases, the linear perturbations travel more slowly than the maximum value of $\frac{\bar{v}}{r}$ at the surface and more rapidly at the baffle. Generally, the mid-level maximum of $\frac{\bar{v}}{r}$ is fairly close to the phase speed of the most unstable wavenumber, although at $S = 3.0$, the value at the baffle is closer.

Chapter 5

DISCUSSION AND CONCLUSIONS

In Chapter 4, the results of the linear experiments were presented directly without including further interpretation. Here, a more in-depth analysis is made and the results are discussed in terms of earlier theoretical studies and the laboratory observations. The chapter concludes with summarizing remarks concerning the nature and interpretation of this study and its relevance to laboratory and natural occurrences of secondary vortices.

5.1 Discussion of Linear Results

In contrast to earlier vortex instability studies, as those discussed in Section 1.3, the present investigation has included the effects of axial boundaries and radial motion in both the axisymmetric and perturbation solutions. The numerical computations were carried out using a geometry appropriate to the laboratory simulator, and the only obvious simplifications made on the flow were free slip on all boundaries and spatial invariance of the eddy viscosity coefficient using only an estimated value. Thus, in comparison to previous theoretical work, this study should provide the most complete and realistic results with regard to the laboratory-simulated tornadoes.

The results of this study do indicate, however, that over much of the range of parameter values, particularly at higher swirl ratios,

those simpler studies are reasonably valid with regard to the laboratory tornado insofar as they include the most important component or components of the vortex. In section 4.5, it was shown that at high S , by far the most important factor in destabilizing the vortex was the presence of a region having a high rate of fluid deformation described by the term $(\bar{v}/r - \partial\bar{v}/\partial r)$, while at somewhat lower S , the term $\partial\bar{w}/\partial r$ was the most important. In all of the above-mentioned studies, where infinitely long and axially invariant vortices are considered, either the first or both of these terms are present. On the other hand, the particular radial profiles of \bar{v} and \bar{w} specified in those studies are not necessarily good approximations to the laboratory simulator. Because only the study by Gall (1983) includes both \bar{v} and \bar{w} in the axisymmetric vortex, while at the same time using realistic radial distributions of those components, it is perhaps uniquely applicable among the infinite-vortex studies to the laboratory results.

Notably, the results of Gall's study and this one show a high degree of similarity. In both cases, the axisymmetric flow is stable to all wavenumbers at very low swirl where no central downdraft exists. Increasing S causes wavenumber 1 to become unstable first, with the most unstable wavenumber subsequently shifting to the shorter wavelengths. The most unstable linear modes are always tilted in the clockwise direction with increasing height (that is, against the axisymmetric flow), and they propagate in the counterclockwise direction. The perturbation pressure fields are very smooth and the maxima lie on or just inside the radius of maximum $\bar{\zeta}$. The w' and ζ' fields contain

a more complex structure and the field maxima are similarly located with respect to both the p' and $\bar{\zeta}$ maxima. The energetics of both studies indicate that at low S , the energy in the perturbation is primarily derived from the radial shear of \bar{w} , while at high S , it originates from the radial distribution of \bar{v} . From these comparisons, it appears that in spite of its simplified treatment of the laboratory vortex, Gall's study nevertheless demonstrates the primary instability in the vortex and includes the more important characteristics of the linear perturbations.

It is obvious, however, that because Gall's model assumes axial invariance in the axisymmetric flow and (except for the phase angle) in the perturbations, some major differences must exist between the results of the two studies. For example, the lower boundary in the present study forces the flow to be strictly horizontal at that level and thus significantly modifies the low level structure of the flow. Similarly, the perturbation fields all exhibit a radial spreading with height following that of the axisymmetric vortex, and a significant axial variation in the intensity of the perturbation often occurs, the maximum amplitude sometimes occurring at high levels and sometimes at low levels. As a consequence, the finer details of the energetics, growth rates, and phase relationships of the perturbations, as mentioned above, are not identical for the two studies. While Gall's study is of a more fundamental nature, with application to a broader class of vortices, this study is designed to be specifically applicable to the laboratory vortex simulator.

An important criterion by which to evaluate this study is in its ability to demonstrate and explain the observed behavior of secondary vortices in the laboratory. A study is particularly worthwhile if it can provide an explanation of a phenomenon in the simplest terms which accurately describe the essential processes involved. In using a linearized, rather than full three-dimensional, model to simulate the development of secondary vortices, this study has eliminated many of the dynamic processes occurring in the flow and has concentrated solely on the initial departure of the flow from a symmetric to an asymmetric state. It would be hoped that many of the characteristics of the linear perturbations observed in this model bear a strong similarity to the fully-developed secondary vortices in the laboratory; then, linear theory alone would be demonstrated as being largely capable of explaining the laboratory results and much of the problem would be solved.

In comparing the linear and laboratory results, the discussion will be mainly qualitative, as very few quantitative measurements of secondary vortices are yet available and the linear model does not produce steady-state perturbation amplitudes. The comparison indicates that in many aspects, a strong connection does exist between the results. Of, perhaps, primary importance is the observation that the multiplicity of secondary vortices in the simulator increases steadily from none up to as many as six as the swirl increases from low to high values. In the linear model, many wavenumbers are often unstable simultaneously; however, there is always one wavenumber (except when

a transition from one wavenumber to the next occurs) which stands out as being the most unstable, and that wavenumber does increase steadily with S . Moreover, the linear model indicates that all wavenumbers are stable for the lowest values of S . Thus, it may be that the wavenumber which appears in the simulator is simply that which is most unstable to the axisymmetric flow, and thus that linear theory alone can largely explain the multiplicity of the secondary vortices with nonlinear processes playing only a minor role. It may also be noted that even with the lowest growth rate for a most unstable wavenumber (i.e., $G \sim 0.3$ for wavenumber 1 and $S = 0.3$), a large amplitude secondary vortex will appear in a reasonable amount of time (several seconds) given a typical amount of background turbulence in the air to act as an initial perturbation.

One way in which the predictions of the linear model and the observations in the laboratory often differ is in the particular swirl ratios where transitions from one wavenumber 1 to the next occur. The linear results indicate that wavenumber 1 first becomes unstable somewhere around $S = 0.2$ or 0.3 , and wavenumbers 2 and 3 become the most unstable beginning at $S = 0.7$ and $S = 1.0$, respectively. In the Purdue simulator, where the inflow is sufficiently strong so that free-slip on the lower surface is a good approximation (see Church et al., 1979), the transitions to the single, double and triple secondary vortex patterns occur around $S = 0.2$, 0.4 , and 1.0 , respectively. Thus, the main difference is in the one-to-two transition. However, it was demonstrated in section 4.3 that any agreement at all between these

results should be rather fortuitous; the linear growth rate spectrum is highly sensitive to the eddy viscosity coefficient and the value chosen for the coefficient was only approximate. Furthermore, as indicated in the introduction, the various transitions obtained in laboratory experiments have differed from one simulator to another. In Ward's simulator, to whose dimensions the numerical models in this study conform, the first two transitions have been found to occur at the lower values of around $S = 0.15$ and $S = 0.2$, while the third transition remains fairly close to $S = 1.0$ (unpublished result). This suggests that the value chosen for ν is probably high for low swirl ratios where the flow is more laminar but that it is fairly good above $S = 1.0$ with the greater turbulence present.

Structurally, we find that the linear mode indicated to be the most unstable for a given swirl ratio and wavenumber possesses many of the characteristics observed in secondary vortices. The linear modes and the secondary vortices always lie on the strong shear zone between the rotating and ascending outer flow and the relatively stagnant central core. Thus, both disturbances occur at larger radii at higher levels and higher swirl ratios. In each case, the disturbances propagate in the same direction as the axisymmetric flow around the center of the chamber. The helical tilt, clockwise with height in a counter-clockwise axisymmetric flow is characteristic of both the secondary vortices in the simulator and the linear modes. Although the cross sections shown in section 4.4 do not indicate much change in the pitch angle with height, an examination of the perturbation phase

angles at all levels reveals that the phase lines are essentially vertical at the lower surface where $\bar{w} = w' = 0$. This is the case observed for secondary vortices. The pitch angle for a given multiplicity of secondary vortices (and linear waves) is readily observed to become more vertical with increasing S . For the longer waves, the linear results indicate that at the lower swirl ratio where a particular wavenumber first becomes unstable, the perturbation tends to have its maximum amplitude at high levels and a much lower amplitude at low levels. On the other hand, at higher swirl ratios, particularly above the range where the wavenumber has been the most unstable, the maximum amplitude has shifted to the lower levels. This effect is much less pronounced in the shorter waves but a relative strengthening of the amplitude at lower levels still does occur with increasing S . This effect corresponds well to the laboratory observation that immediately after a transition to a higher wavenumber has taken place, the secondary vortices often do not reach the lower surface or are only weak there. Another laboratory observation is that while the longer waves remain well defined all the way up to the baffle, wavenumbers of 3 or more end in turbulence before reaching that height. This result likewise appears to be predicted by the linear model: The linear wave structures representing peaks in the growth rate spectrum, i.e., Figs. 4.15 - 4.19, 4.22 - 4.24, 4.27 - 4.29 and 4.32 - 4.34, show the longer waves to have large relative amplitudes at high levels while the shorter waves are much weaker near the top.

There are two interesting structural phenomena observed in the laboratory which are not apparent in the numerical results. Firstly, as mentioned in Section 1.2, when only a single helical secondary vortex occurs, the fluid in the helix never travels appreciably in the azimuthal direction but moves only vertically and radially. The reason for this result, as explained in Church et al. (1979) is based on the fact that coincidentally with this case, the central axisymmetric downdraft does not exist or does not extend very far below the baffle; instead, a weak updraft prevails along the axis. In the linear model, on the other hand, wavenumber 1 occurs as the only unstable wave at $S = 0.3$ where $\bar{w} < 0$ along the axis, and the perturbation does travel azimuthally. A possible cause for the persistence of the central updraft in the simulator to somewhat higher swirl ratios is the enhanced radial inflow in the lower boundary layer which is induced by the viscous stress of the surface. If this is true, the simplifying assumption of free-slip employed in the numerical models may have significantly altered the results for low S and wavenumber 1. The second phenomenon observed in the simulator is that occasionally, one secondary vortex of a multiple vortex system differs from the rest, being weaker (or, rarely, stronger) than the rest (Snow and Church, 1981). This effect is not observable in a single-mode linear solution, that is, a linear solution which has been integrated until only the most unstable mode remains. Possibly, the observed phenomenon is an inherently nonlinear process related to the interaction of different wavelengths.

On the other hand, the variation in the secondary vortices may result from the interaction of two separate linear modes (having the same wavenumber and for the same swirl ratio) which have nearly identical growth rates. The occurrence of such cases was observed a few times in the linear experiments causing the numerical integrations to be necessary for extra long periods of time. The most extreme case was experiment number 6 ($S = 0.5$, wavenumber 2) where even after the equivalent of a full minute of simulated time, there still existed a secondary mode having nearly the same amplitude as the most unstable mode.

From the above comparisons between the observed characteristics of secondary vortices and the growth rates and structures of the modeled linear perturbations, it appears that although there are some discrepancies, linear theory does go a long way in accurately describing the departure of a high-swirl tornadolike vortex from an axisymmetric state. An examination of the linear results allows a number of deductions to be made concerning secondary vortices. Looking back at Section 4.5, we recall that energy term 1, which has the form $u'v'(\frac{\bar{v}}{r} - \frac{\partial \bar{v}}{\partial r})$, stands alone at high S as being the dominant energy source for the perturbations. The quantity in parenthesis has by far its most extreme value in the region of maximum $\bar{\zeta}$. Thus, it is by having u' and v' negatively correlated in that region (e.g., see Fig. 4.33) that the perturbation is able to gain so much energy from the axisymmetric flow. At larger radii, where the parenthetical quantity is positive, the correlation between u' and v' has fallen to near zero

so that the perturbation does not lose energy there. Note that the change in the relative phase is achieved from the strong radial tilt of v' in contrast to the much lesser tilt of u' . As pointed out earlier, $(\frac{\bar{v}}{r} - \frac{\partial \bar{v}}{\partial r})$ represents the rate of fluid deformation (rather than the vorticity). Thus, it is not the high maximum of $\bar{\zeta}$ itself which destabilizes the vortex but rather the deformation which occurs in the same region. At much lower swirl ratios, the region of high $\bar{\zeta}$ is much closer to the center so that $\frac{\bar{v}}{r}$ is similar in magnitude to $\frac{\partial \bar{v}}{\partial r}$. Hence, the deformation due to \bar{v} is small and very little energy can be extracted from term 1. It is important to note that $\bar{\zeta}$ is always positive. Thus, the so-called "inertial instability," which depends on the existence of some region of vorticity having the opposite sense from the rotation of the axisymmetric flow, is not the cause of the secondary vortices in the laboratory.

It was also seen in Section 4.5 that energy term 2, having the form $-u'w' \frac{\partial \bar{w}}{\partial r}$, was the dominant perturbation energy source for all wavenumbers at low S . Note that terms 2 and 5 could have been combined to form $-u'w' (\frac{\partial \bar{w}}{\partial r} + \frac{\partial \bar{u}}{\partial z})$ which again relates to deformation of the axisymmetric flow, this time in the r - z plane. The terms were separated to emphasize the importance of \bar{w} on vortex instability at low swirl ratios, and also because term 6 is always small. Thus, for term 2, deformation and vorticity are identical. It can be seen in Figs. 4.15 - 4.24 and 4.30 - 4.32, which represent low swirl cases, that u' and w' are very negatively correlated in the region of maximum $\bar{\zeta}$ (which has the same location as the most intense $\bar{\eta}$ or $\frac{\partial \bar{w}}{\partial r}$) so that the

perturbations can extract the maximum energy from the axisymmetric flow. This correlation continues for higher swirl cases as well (for the shorter waves) where the contribution from term 2 is approximately the same. The fact that term 2 is low for high S and low wavenumber indicates that the correlation between u' and w' is closer to zero there, which can be seen from Figs. 4.25 and 4.26.

It is interesting to compare the relative positions of the u' , v' and w' maxima. v' and w' are generally positively correlated while u' is negatively correlated with them both. This arrangement results in strong inward, upward and counterclockwise (positive θ) motion occurring together and strong outward, downward and clockwise motion occurring together. The combination causes the large swirling and rising momentum at larger radii to be transported inward across the shear zone while the low momentum from the interior is transported outward, as would be expected from a growing perturbation. The effect of the momentum transport should resemble, to some degree, the action of viscous stress in broadening the shear zone of the axisymmetric flow. This nonlinear feedback is one of the mechanisms by which the secondary vortex amplitude would be limited.

The other term which involves cross-correlations between different perturbation velocity fields is term 4 ($-v'w' \frac{\partial \bar{v}}{\partial z}$). The other half of the deformation expression, $-(\frac{v'w'}{r}) \frac{\partial \bar{w}}{\partial \theta}$, is zero from axisymmetry. Although v' and w' are quite positively correlated, $\frac{\partial \bar{v}}{\partial z}$ tends to be only weakly negative so term 4 only amounts to a small energy source.

Terms 3 and 5 ($-u'u' \frac{\partial \bar{u}}{\partial r} - v'v'\bar{u}$ and $-w'w' \frac{\partial \bar{w}}{\partial z}$) are stretching deformation terms related to the degree of horizontal convergence and vertical divergence of the axisymmetric flow. Note that only auto-correlations (which are inherently positive) of the perturbation fields are involved here. In term 3, because $-\frac{\partial \bar{u}}{\partial r}$ and $-\bar{u}$ are positive at low levels and generally negative at higher levels, the term will tend to be an energy source for those waves having the largest amplitudes in the inflow region. Term 5 is interesting because although $-\frac{\partial \bar{w}}{\partial z}$ is quite negative for the flow on the whole, it is positive in the shear zone where the perturbations have the highest amplitude. Thus, term 5 is generally positive. Note that for the cases $S = 0.3$ with $m = 1$ and $S = 0.5$ with $m = 2$, the unusually large relative amplitudes developed at the highest levels correspond to the larger values which occur in term 5 for those cases. (Similarly, the large negative value of term 7 for the latter case can be attributed, in part, to the unusually large amplitude at the baffle.) Because terms 3 and 5 are never dominant, however, it must be concluded that the strong radial inflow and vertical stretching which occur at lower levels in the axisymmetric vortex do not appreciably affect the energetics of the perturbations. Rather, it is only the structure of the flow which is significantly altered by the lower boundary and inflow.

Term 8, which represents viscous dissipation, is nearly always the largest energy sink for the perturbations. Interestingly, for linear experiments near the critical instability curve, particularly at the lowest unstable swirl ratio for wavenumbers 3 - 5 and the

highest unstable swirl ratio (near 3.0) for wavenumber 1, dissipation remains a large energy sink and is thus highly influential in determining the precise location of the curve. Recall, for example, that when a lower viscosity coefficient was used, the effect of which would lessen the magnitude of term 8, the neutral stability curve was shifted to lower values of S . Of course, another major effect of decreased viscosity is to narrow the shear zone of the axisymmetric vortex, thus intensifying the strength of the shear. This will increase, in particular, energy terms 1 and 2 and, consequently, the growth rates of the waves. (It seems unlikely that the lowering of viscosity would ever cause the lowest swirl ratio flow to become unstable, however; there, no central downdraft occurs and thus the shear zones of \bar{v} and \bar{w} are weak or nonexistent.) Because the shorter waves are more highly damped by dissipation, as demonstrated in Fig. 4.35, the shift toward shorter waves of the growth rate spectrum peak which was found to occur with decreased viscosity can be partially explained. Furthermore, it has been argued by others that the most favored wavelength of a perturbation should be closely related to the width of the shear zone. If this is true, a decrease in the shear zone width (which occurs with a lower viscosity coefficient) should decrease the preferred azimuthal wavelength. Because the strength of the viscosity does not appreciably affect the total circumference of the shear zone in which the waves lie, a higher preferred wavenumber should result from lower viscosity.

The above argument concerning the effect which the width and circumference of the shear zone have on the dominant wavenumber

suggests an explanation for another observed phenomenon: Recall that both in the laboratory simulator and the linear model, at the lower end of the swirl ratio range where a particular wavenumber dominates the flow, the maximum perturbation amplitude tends to occur at the upper levels, particularly for the longer waves. On the other hand, at the high end of that swirl ratio range, the largest amplitudes are found at the lower levels. The reason for this may be the radial spreading with the height of the axisymmetric shear zone: As the entire vortex expands with increasing S , the most ideal shear zone circumference for any given wavenumber should be found first at high levels and then later at low levels. It can also be argued that this effect should, as observed, be most pronounced for the longer waves where the percentage increase in wavenumber at a transition is larger.

5.2 Conclusions

This study has examined the formation and characteristics of secondary vortices in an axisymmetrically forced, tornadolike vortex. The particular type of vortex on which the investigation focused was that developed by a Ward-type vortex simulator, a laboratory device designed to generate flow resembling that in a rotating, tornado-producing cumulonimbus supercell. (Secondary vortices have been produced in that simulator and have been extensively studied.) The method used in this study was to numerically generate steady state axisymmetric vortex flows for a variety of swirl ratios, and to test each of these flows for instability to linearized, axially asymmetric perturbations. For those flows found to be unstable, the details of the

growing linear perturbations were presented and discussed at length. The study was found to be capable of reproducing and explaining a number of the characteristics of secondary vortices observed in previous laboratory experiments.

As this was the first vortex instability study which included an axial boundary, a low-level radial inflow, and axial variations in the axisymmetric vortex, there was a particular interest in the possible effect these would have on the linear solutions. It was found that, while the perturbation structures were altered somewhat from Gall's more idealized vortex, the perturbations bore approximately the same relationship to the axisymmetric flow both in spatial location and in energetics. In both studies, the particular distributions which the azimuthal and vertical velocity components have in the radial direction were found to have by far the greatest influence on the perturbations.

This investigation being a linear instability study, it is primarily concerned with the reasons why secondary vortices form in an axisymmetrically forced primary vortex, and with the manner in which the unstable vortex initially departs from a symmetric state. Hence, many questions concerning the behavior of fully developed secondary vortices, such as their maximum intensity, are not directly dealt with. However, it is supposed that, because of the strong resemblance between the laboratory observations and the linear results, and because the laboratory simulator is designed to model certain types of natural tornadoes, some features of naturally occurring secondary vortices

might be inferred from the linear results. For example, the linear growth rates obtained are sufficiently high to indicate that secondary vortices should appear quickly, once the primary vortex becomes unstable. Secondary vortices would be expected to lie near the radius in the primary vortex where the maximum vertical vorticity is found, not where the maximum azimuthal velocity occurs, and they should travel with approximately $1/2$ to $2/3$ the maximum angular velocity found in the primary vortex (this latter behavior has been observed in tornadoes, e.g., Forbes, 1976). Another indication of the linear results is that the most intense region of secondary vortices is usually at the lower surface, the part of greatest concern in terms of destructive force.

In certain respects, the methods used in this study are subject to criticism for being unrealistic. A number of simplifying assumptions were employed in the modeling of the secondary vortices. Most important among these was the linearization of the perturbation equations which omitted many important dynamic processes, including those which limit the perturbation amplitudes. No interaction between different wavenumbers was allowed, nor was modification of the axisymmetric vortex due to the presence of secondary vortices. Rather than have a particular wavenumber perturbation develop from an already asymmetric flow, which is usually the case in an actual vortex, perturbations of all wavenumbers were spawned directly from symmetric vortices only. However, the main purpose of using this approach was to determine whether the relatively simple linear theory was alone

capable of reproducing many of the primary features of observed secondary vortices. Because such was indeed shown to be the case, we can draw the conclusion that secondary vortices can be attributed mainly to the axisymmetric part of a vortex, and depend less significantly on other scales of asymmetry. A secondary goal of using linear theory was to demonstrate that the high-swirl axisymmetric vortex (of the type investigated) is unstable; this indicates that such a flow configuration cannot exist except under very specialized conditions, and thus that secondary vortices are a necessary consequence of the high swirl. Another of the questionable assumptions used in the models was the free-slip boundary condition. Although it is believed that the results of this approximation were of little consequence for the top and outer boundaries, given that the baffle pressure could still be made constant with radius and the outer computational boundary was rather removed from the center of action, it was demonstrated that the stress of the lower boundary may have important effects on the interior flow. The boundary-induced radial inflow which is known to occur in the simulator within the lowest few centimeters (e.g., Baker, 1981) is possibly responsible for increasing the swirl ratio where the central axisymmetric downdraft first penetrates to the surface, and the single secondary vortex regime occurs while the axis flow is still upward. According to Church et al. (1979), the central updraft, rather than downdraft, coexisting with the secondary vortex is responsible for the vortex having certain unique characteristics. At higher swirl ratios, the free-slip lower boundary condition appears to be reasonably

valid. The other major modeling assumption to which objections are justifiable is the invariance of the eddy viscosity coefficient both with the spatial coordinates and with the swirl ratio. As pointed out earlier, it is obvious that ν often varies considerably with position in a given flow, particularly one having a high swirl ratio, since the visible level of turbulence is highly location dependent (e.g., Church et al., 1979). It seems unreasonable, however, in a study of this type to attempt to compute accurate spatial distributions of ν because complicated and time consuming techniques such as second order closure would be required. Instead, the much simpler constant viscosity assumption was deemed a very appropriate first approximation. The invariance of ν with the swirl ratio is, on the other hand, a more serious simplification. The numerical results were clear in demonstrating the sensitivity of the growth rate spectrum (in particular, its peak) to the viscosity coefficient, and it appears obvious that ν should increase with S given the corresponding increase in the observable turbulence. Thus, only by properly varying ν with S can the linear results be expected to accurately predict the swirl ratios where the transitions of the most unstable wave from one wavenumber to the next should occur. However, as mentioned above, the accurate determination of ν would have required a complicated process. On the other hand, to have varied ν simply for tuning the model and forcing the transitions to match properly would have obscured the effect of varying the swirl ratio. For these reasons, the viscosity coefficient was left

as a constant. Of course, it must follow that the numerical values obtained for the linear growth rates are only roughly approximate.

A natural suggestion for refining this research is to lift the above-mentioned simplifications and to try to more closely match the observed laboratory results. In adopting a no-slip condition at the boundaries, a higher grid resolution would be required there. Of perhaps equal interest would be to explore the effects of different simulator geometries, inflow rates and degrees of surface roughness. These areas have been given considerable attention in laboratory experiments but have not yet been investigated numerically. Ultimately, of course, the simulator walls and baffle, whose influences on the flow are artificial, should be removed and the scale of the problem should be expanded to match that of an actual tornado case. Modeling the readily observable and measureable flows produced in the laboratory, however, is an important first step, both for studying the known flow and for verifying the numerical models. It is hoped that the results of this investigation will suggest areas for further research in the laboratory and in dealing with natural tornadoes.

REFERENCES

- Agee, E., C. Church, C. Morris, and J. Snow, 1975: Some synoptic aspects and dynamic features of vortices associated with the tornado outbreak of 3 April 1974. Mon. Wea. Rev., 103, 318-333.
- Arakawa, A., 1966: Computational design for long-term numerical integrations of the equations of atmospheric motion. J. Comput. Phys., 1, 119-143.
- Arakawa, A., and V. R. Lamb, 1977: Computational design of the basic dynamical processes of the UCLA general circulation model. Methods in Computational Physics, 17, Academic Press, 174-265, 337.
- Asselin, R. A., 1972: Frequency filter for time integrations. Mon. Wea. Rev., 100, 487-490.
- Baker, G. L., 1981: Boundary layers in laminar vortex flows. Ph.D dissertation, Purdue University.
- Batchelor, G. K., 1967: An Introduction to Fluid Dynamics, Cambridge University Press, Cambridge, U. K., 615.
- Brown, J. A., 1969: A numerical investigation of hydrodynamic instability and energy conversions in the quasigeostrophic atmosphere, Part I. J. Atmos. Sci., 26, 352-365.
- Bryan, K., 1966: A scheme for the numerical integration of the equations of motion on an irregular grid free of nonlinear instability. Mon. Wea. Rev., 94, 39-40.
- Church, C. R., J. T. Snow, G. L. Baker, and E. M. Agee, 1979: Characteristics of tornado-like vortices as a function of swirl ratio: A laboratory investigation. J. Atmos. Sci., 36, 1755-1776.
- Davies-Jones, R. P., 1973: The dependence of core radius on swirl ratio in a tornado simulator. J. Atmos. Sci., 30, 1427-1430.
- Davies-Jones, R. P., 1976: Laboratory simulations of tornadoes. Proc. Symp. on Tornadoes. Lubbock, Dept. of Civil Engr., Texas Tech. University, 151-173.

- Forbes, G. S., 1976: Photogrammetric characteristics of the Parker tornado of April 3, 1974. Proc. Symp. on Tornadoes. Lubbock, Dept. of Civil Engr., Texas Tech University, 58-77.
- Forsythe, G. E., M. A. Malcolm, and C. B. Moler, 1977: Computer Methods for Mathematical Computations. Prentice-Hall, Inc., Englewood Cliffs, N. J., 259.
- Fujita, T. T., D. L. Bradbury, and C. F. Van Thullenar, 1970: Palm Sunday tornadoes of April 11, 1965. Mon. Wea. Rev., 98, 29-69.
- Fujita, T. T., et al., 1976: Photogrammetric analyses of tornadoes. Proc. Symp. on Tornadoes. Lubbock, Dept. of Civil Engr., Texas Tech University, 43-88.
- Gall, R. L., 1982: Internal dynamics of tornado-like vortices. J. Atmos. Sci., 39, 2721-2736.
- Gall, R. L., 1983: A linear analysis of the multiple vortex phenomenon in simulated tornadoes. J. Atmos. Sci., 40, XXX-XXX.
- Haltiner, G. J., and R. T. Williams, 1980: Numerical Prediction and Dynamic Meteorology, John Wiley and Sons, Inc.
- Hoecker, W. H. Jr., 1960: Wind speed and air flow patterns in the Dallas tornado of April 2, 1957. Mon. Wea. Rev., 88, 167-180.
- Holton, J. R., 1972: An Introduction to Dynamic Meteorology. Academic Press, 319.
- Kurihara, Y., 1965: On the use of implicit and iterative methods for the time integration of the wave equation. Mon. Wea. Rev., 93, 33-46.
- Lilly, D. K., 1981: Wave-permeable lateral boundary conditions for convective cloud and storm simulations. J. Atmos. Sci., 38, 1313-1316.
- Maslowe, S. A., 1974: Instability of rigidly rotating flows to non-axisymmetric disturbances. J. Fluid Mech., 64, 307-317.
- Mehta, K. C., 1976: Windspeed estimates: Engineering analyses. Proc. Symp. on Tornadoes. Lubbock, Dept. of Civil Engr., Texas Tech University, 89-103.
- Michalke, A., and A. Timme, 1967: On the instability of certain two-dimensional vortex-type flows. J. Fluid. Mech., 29, 647-666.

- NCAR Software Support Library Manual, 1975, Natural Center for Atmospheric Research, Boulder, Colo.
- Orlanski, I., 1976: A simple boundary condition for unbounded hyperbolic flows. J. Comput. Phys., 21, 251-269.
- Rotunno, R., 1977: Numerical simulation of a laboratory vortex. J. Atmos. Sci., 34, 1942-1956.
- Rotunno, R., 1978: A note on the instability of a cylindrical vortex sheet. J. Fluid Mech., 87, 761-771.
- Rotunno, R., 1982: Numerical simulation of multiple vortices. Topics in Atmospheric and Oceanic Science: Intense Atmospheric Vortices, L. Bengtsson and J. Lighthill, Eds., Springer-Verlag, Berlin, Heidelberg, 215-228.
- Snow, J. T., 1978: On inertial instability as related to the multiple vortex phenomenon. J. Atmos. Sci., 35, 1660-1677.
- Snow, J. T., and C. R. Church, 1981: Observations of instabilities in tornado-like vortices. Paper presented at Third Conference of Atmospheric and Oceanic Waves and Stability, Jan. 19-23, 1981, San Diego, Calif.
- Staley, D. O., and R. L. Gall, 1979: Barotropic instability in a tornado vortex. J. Atmos. Sci., 36, 973-981.
- Ward, N. B., 1972: The exploration of certain features of tornado dynamics using a laboratory model. J. Atmos. Sci., 29, 1194-1204.
- Warn-Varnas, A., W. W. Fowlis, S. Piacsek, and S. M. Lee, 1978: Numerical solutions and laser-doppler measurements of spin-up. J. Fluid Mech., 85, 609-639.
- Williams, G. P., 1969: Numerical integration of the three-dimensional Navier-Stokes equations for incompressible flow. J. Fluid Mech., 37, 727-750.